Ferromagnetic Resonance Force Microscopy

Thesis by

Melissa Masae Midzor

In Partial Fulfillment of the Requirements

for the Degree of

Doctor of Philosophy

Advisor: Professor Michael L. Roukes

California Institute of Technology

Pasadena, California

2001

(Defended September 12, 2000)

Acknowledgements

When I first joined the group, my advisor Michael compared the pursuit of a Ph.D. to that of an Olympic athlete — years of accumulated effort, challenges, frustrations, and, hopefully, triumphs. As one of the first students in a new group that quickly grew to be a small empire of cutting edge science, the challenges and demands cannot be readily described. Like the athletes competing in Sydney this year, I can only hope to thank a small fraction of the many people who supported me directly or indirectly to accomplish this goal. In this small space I hope to thank those whose efforts and support have affected my work the most significantly.

For the opportunity to work on an extremely interesting and challenging project, providing the equipment to do the work with, being supportive during the depressing year after my divorce, sending me to Los Alamos to gain valuable experience, letting me branch away from NMRFM to pursue FMRFM, and believing in and developing my abilities as an experimental physicist, I am grateful to my advisor, Michael Roukes. I thank Chris Hammel, whose collaboration and support at Los Alamos, physical insights, and daily interactions during my visits were pivotal to my pursuit of FMRFM. Special thanks to Phil Wigen, who spent five incredible months working daily with me in the lab, whose insights into FMR shaved months off my head-banging attempts trying to understand the data, and whose enthusiasm in the lab drove me to greater accomplishments in my research. Those months were the most fun in my career as a scientist. I also am grateful to Nils Asplund, for all his help in building the intricate and vital parts of the apparatus I could never hope to build myself, teaching me the machine shop skills I needed to build the parts I could; and encouraging me when the end never seemed to be in sight. The FMRFM work would not have been possible without the samples and insightful conversations provided by Phil Wigen, Jeff Childress, Ursula Ebels, Kamel Ounadjela, Brett Heinrich, and Richard

Campbell.

I often gleaned help from people in a variety of areas and talents from within our group at Caltech and Los Alamos, and from groups of other disciplines at Caltech. I am grateful to the post-docs, for passing on their skills while they themselves were immersed in challenging projects: Tim Tighe, the first to teach me semiconductor processing, and Keith Schwab, who always had an interesting idea or two on many aspects of my research. Special thanks to Darrell Harrington, who has helped me immensely with mechanical oscillators (their theory, design, and measurement), microstrip resonators, and semiconductor fabrication, and who was always willing to lend me a hand with my experiment. Thanks to Frank Monzon, for his dedication to keep the equipment in the clean room and the water circulators working against all odds. The optics of my apparatus were successful in a large part due Josh Bliss and the Caltech optics groups of Libbrecht and Kimble, who provided valuable help and many of the low noise components of my interferometer.

I would especially like to thank Zhengyong Zhang, for teaching me FMR, the art of duct-tape physics, and the details of the MRFM apparatus throughout the many months I spent in Los Alamos. My career in physics has always been driven by my interest in ferromagnetics (which began when I was a small child), and I am grateful that his first FMR experiments opened up this avenue for my Ph.D. research. I will miss working with Denis Pelekhov, whose incredible skill as an experimental physicist and whose crazy ideas — which actually worked — led to great advances in the MRFM research. Thanks to Wei Chen and Michael Cross for their enlightening theoretical discussions and suggestions, and in particular to Wei for his calculations of the internal fields and the quantum well theory. I would like to acknowledge Stacia Rutherford, Exie-Marie, and the three previous administrative assistants who made sure my equipment orders were taken care of quickly (often under of the pressure of "I need it yesterday"), and letting me vent my frustrations of being a graduate student.

Finally, I want to thank the people closest to me who have given support mentally and emotionally throughout the long years: my best friend at Caltech, Rick Jenet, for being there when I needed a Red Door break or had math questions at 4 am, and for being an

all around friend. My parents, Denis and Clare Midzor, whose love and support in all of my myriad endeavors has been unwavering. My best friend of 16 years, Bonnie Barnes, whose complete faith in my abilities sustained me through the times I doubted myself, who could always cheer me up, and who listened with complete sympathy to my woes as a grad student. And finally, to Steve Frey, my future husband, who suffered through the last and most strenuous years of my graduate career, and who has made my life wonderful even at the most stressful times.

My deepest and sincerest gratitude to all.

Abstract

A new approach to magnetic resonance was introduced in 1992 based upon detection of spin-induced forces by J. Sidles [1]. This technique, now called magnetic resonance force microscopy (MRFM), was first demonstrated that same year via electron paramagnetic resonance (EPR) by D. Rugar *et al.* [2]. This new method combines principles of magnetic resonance with those of scanned probe technology to detect spin resonance through mechanical, rather than inductive, means. In this thesis the development and use of *ferromagnetic resonance force microscopy* (FMRFM) is described. This variant of MRFM, which allows investigation of ferromagnetic samples, was first demonstrated in 1996 by Z. Zhang *et al.* [3]. FMRFM enables characterization of (a) the dynamic magnetic properties of *microscale* magnetic devices, and (b) the spatial dependence of ferromagnetic resonance within a sample. Both are impossible with conventional ferromagnetic resonance techniques.

Ferromagnetically coupled systems, however, pose unique challenges for force detection. In this thesis the attainable spatial resolution – and the underlying physical mechanisms that determine it – are established. We analyze the dependence of the magnetostatic modes upon sample dimensions using a series of microscale yttrium iron garnet (YIG) samples. Mapping of mode amplitudes within these sample is attained with an unprecedented spatial resolution of $15\mu m$. The modes, never before analyzed on this scale, fit simple models developed in this thesis for samples of micron dimensions. The application of stronger gradient fields induces localized perturbation of the ferromagnetic resonance modes. The first demonstrations of this effect are presented in this study, and a simple theoretical model is developed to explain our observations. The results indicate that the characteristics of the locally-detected ferromagnetic modes are still largely determined by the external fields and dimensions of the entire sample, rather than by the localized interaction volume (i.e., the locale most strongly affected by the local gradient field). Establishing this is a crucial first

step toward understanding FMRFM in the high gradient field limit where the dispersion relations become locally determined. In this high gradient field regime, FMRFM imaging becomes analogous with that of EPR MRFM.

FMRFM has also been employed to characterize magnetic multilayers, similar to those utilized in giant magnetoresistance (GMR) devices, on a lateral scale $40 \times 40 \mu m$. This is orders of magnitude smaller than possible via conventional methods. Anisotropy energies, thickness, and interface qualities of *individual* layers have been resolved.

This initial work clearly demonstrates the immense and unique potential that FMRFM offers for characterizing advanced magnetic nanostructures and magnetic devices.

Contents

List of Figures

1 Introduction

Ferromagnetic Resonance (FMR) is an important technique for characterizing magnetic materials and devices. Improvements in sample preparation techniques have enabled the development of extremely uniform, thin, single crystal magnetic films. This has resulted in magnetic devices with thicknesses on the order of Angstroms and lateral dimensions approaching the micron scale. FMR, which characterizes the dynamic properties of these materials such as exchange and anisotropy energies, can be a vital tool to the characterization and future development of miniaturized magnetic devices. However, conventional FMR techniques, in which the resonance is detected inductively, is limited in sensitivity and thus requires relatively large sample areas ($\tilde{}mm^2$). It has not been generally possible to characterize, on a microscopic scale, the spatial dependencies of the magnetic anisotropy and exchange energies in ferromagnetic devices or individual ferromagnetic nanostructures.

In 1992, theoretical [1][4] and experimental work [2][5] was carried out demonstrating magnetic resonance force microscopy (MRFM). MRFM is a new 3D imaging technique with the potential of achieving atomic scale resolution. This approach, which combines principles of magnetic resonance with scanning technology, is based upon mechanical, rather than inductive, detection. It achieves this by sensitively detecting the force between a small probe magnet and the spin moment in the sample by means of a mechanical resonator. A probe magnet mounted upon a mechanical resonator provides a gradient field, ∇H, necessary for imaging. It also generates a time-varying interaction with the spin magnetization $\vec{M}$ in the sample that imposes a force, $F = \vec{M} \cdot \vec{\nabla} H$, upon the mechanical resonator. The external fields driving the magnetic resonance are carefully manipulated to produce a modulation in the magnitude of $\vec{M}$ at one of the resonance frequencies of the mechanical resonator. The magnetic resonance signal is enhanced by the quality factor, Q, of the force-driven mechanical resonator. For electron paramagnetic resonance (EPR) and nu-

clear magnetic resonance (NMR), the resonance condition is a local function of the total scalar external magnetic field. Thus, the gradient field and the sample linewidth determine a volume in space in which the resonance condition is met.

Ferromagnetically coupled systems pose unique challenges for force detection. Strong coupling between local moments lead to magnetic resonance modes that are not localized, but extended throughout the sample. The resonance conditions for FMR are strongly influenced by $\vec{H}_{Total}$, the total *vector* field resulting from the applied external and magnetic gradient fields, and also by the sample geometry. Thus, the resolution, or resonance volume, is no longer simply localized nor determined solely by the gradient field and sample line width.

Ferromagnetic resonance on microscopic samples using the MRFM technique (FMRFM) was first demonstrated in 1996 [3]. However, the physical mechanisms that determine the attainable spatial resolution employing the FMRFM technique has not yet been established. There are two objectives of the research presented here: (1) to develop the physical principles of spatial resolution and sensitivity in FMRFM, and (2) to demonstrate and explore the unique possibilities of FMRFM to characterize the dynamic properties of magnetic microstructures.

In this thesis the attainable spatial resolution – and the underlying physical mechanisms that determine it – are established. The dependence of the magnetostatic modes upon sample dimensions are analyzed using a series of microscale yttrium iron garnet (YIG) samples. Mapping of mode amplitudes within the sample are attained with an unprecedented spatial resolution of $15\mu m$. The modes, never before analyzed on this scale, fit simple models developed in this thesis for samples of micron dimensions. With the application of stronger gradient fields, localized perturbations of the ferromagnetic resonance modes are possible. The first demonstrations of such an effect are presented in this study. A simple theoretical model to explain these observations is developed. The miniature gradient magnet perturbs the RF absorption (i.e., signal intensity) of certain modes within a small, localized volume of the sample. The results indicate that in these first experiments the

locally-detected ferromagnetic mode positions are still largely determined by the external fields and dimensions of the entire sample, rather than by the characteristics of the localized interaction region (i.e., the region most strongly affected by the local gradient field). This work is a crucial first step toward understanding FMRFM in the high gradient field limit where the dispersion relations become determined locally. In this high gradient field regime, FMRFM imaging becomes analogous with that of EPR MRFM.

Magnetic multilayers, similar to those employed in giant magnetoresistance (GMR) devices, have also been characterized on a lateral scale ($40 \times 40 \mu m$) that is orders of magnitude smaller than possible via conventional methods. Anisotropy energies, thickness, and interface qualities of *individual* layers have been resolved.

1.1 History of MRFM

It was first suggested by J.A. Sidles in 1992 that magnetic resonance imaging (MRI) could be achieved with unprecedented sensitivity and spatial resolution by magnetically coupling a mechanical force detector to the spins driven into resonance [1][4]. The spatial resolution of MRI is currently limited, by the sensitivity of inductive detection of magnetic resonance, to dimensions greater than tens or hundreds of microns. On the other hand, scanned probe microscopies such as atomic force microscopy (AFM) have been developed which yield atomic resolution. However, these techniques can only be applied to surface studies. The proposed technique essentially combines the advantages of MRI – chemical specificity, subsurface sensitivity, non-destructiveness, and 3-D capabilities – with the force sensing technology of AFM.

The first demonstration of MRFM was achieved by D. Rugar *et al.* in 1992 [6]. Mechanical detection of electron paramagnetic resonance (EPR) was demonstrated using a $30ng$ particle of 2,2-diphenyl-1-picrylhydrazyl (DPPH) affixed to a commercial AFM cantilever. The gradient field was $\nabla H = 0.6G/\mu m$, and this yielded an axial (along the polarizing field) spatial resolution of $19\mu m$. The cantilever had a resonance frequency of $f_c = 8kHz$ and a force constant of $k = .1N/m$. The experiment was performed at ambient temperature

and vacuum ($Q = 2000$). The magnetization of the sample was modulated by adding an oscillating field to the external magnetic field at a frequency of $\frac{f_c}{2}$, and the non-linear response of the magnetization at resonance was then detected at f_c (this is termed the half-frequency modulation technique).

The lateral resolution potential of MRFM was first demonstrated by D. Rugar *et al.* in 1993. Two individual $20\mu m$ DPPH particles, affixed to a cantilever and separated by $35\mu m$, were spatially resolved [7]. The experimental conditions were similar to their earlier demonstration of MRFM [6]. A gradient field of $4.3G/\mu m$ yielded a lateral resolution of $5\mu m$ and an axial resolution of $1\mu m$. Similar results were later obtained by our group [8] and a group at the University of Washington [5].

NMR AND EPR VS. FMR

NMR and EPR are the best candidates for the ultimate goals of sensitivity and spatial resolution in magnetic resonance because their dispersion relations allow for spatial resolution to approach atomic scales [9]. The resolution of NMR or EPR MRFM has straightfoward dependencies upon (a) the mechanical force detector's sensitivity, which is compromised by thermal and external noise sources, (b) the strength of the gradient magnet, and (c) the polarization of the sample. Larger gradient fields, lower temperatures, and increasing the force detector's sensitivity will increase the resolution. From 1992 to 1996, MRFM research focused on improving resolution solely in the application of NMR and EPR measurements. Notable advances in the field of NMR or EPR MRFM are described below.

The approach taken so far has been to develop ultrasensitive mechanical force detectors that utilize cantilevers with force constants much smaller than commercial AFM cantilevers which still yield resonance frequencies in the kHz range. The first ultrasensitive cantilevers [10] had a force constant of $k \sim 10^{-5} N/m$, and were used by *Rugar et al.* [2] in 1994 to detect the magnetic resonance of ^{1}H nuclear spins in ammonium nitrate. A sensitivity of 1.6×10^{13} proton spins was achieved at room-temperature in a warm-bore superconducting magnet providing a vacuum of $< 10^{-3} torr$ with a gradient field of $6G/\mu m$. A spatial

resolution of $2.6\mu m$ was attained. This spatial resolution and sensitivity was several orders of magnitude smaller than possible via conventional NMR techniques.

High Q cantilevers and low temperatures were later used to improve the sensitivity. The ^{19}F nuclear spins in 1% Nd-doped CaF_2 were detected by Wago *et al.* in 1996 [11]. The sample was affixed to the cantilever which, unloaded, had characteristics as follows: $k = 0.07N/m$ and $f_c = 9.8kHz$, and a Q of 4×10^4 at room temperature, which increased to 20×10^4 at $6K$. The frequency dropped to $1.6kHz$ when the sample was affixed to the cantilever. The gradient field employed was $6G/\mu m$.

The first observation of ferromagnetic resonance force microscopy (FMRFM) was achieved by Z. Zhang *et al.* in 1996 [3]. This experiment, which yielded strong signal intensities even at ambient temperatures and pressures, demonstrated the potential of MRFM to become a powerful technique for FMR with micron or sub-micron resolution. Ferromagnetic modes from a yttrium iron garnet (YIG) film with nominal lateral dimensions of $20 \times 40\mu m$ and a thickness of $3\mu m$ were observed. The gradient field was $0.5G/\mu m$, and the resonance frequency and Q of the sample-bearing commercial Si cantilever were $5.26kHz$ and 41 respectively. The gradient field in these experiments was insufficient to provide lateral spatial resolution of the ferromagnetic resonance modes within the sample. An improved modulation technique, termed "anharmonic modulation," first demonstrated by Bruland *et al.* in 1994, was used to obtain the FMRFM signal and avoid spurious coupling to the cantilever.

Sensitivity and resolution is fairly straightforward and reasonably well understood for NMR and EPR MRFM, although it still poses challenge – both in the technology and in the physics – to achieve single spin detection. However, the large coupling of magnetic moments in ferromagnetic materials make the physics determining sensitivity and spatial resolution in FMRFM quite complex. It is the objective of this work to (a) develop FMRFM and to determine the underlying physical principles governing its sensitivity and spatial resolution, and (b) demonstrate its potential for characterizing the dynamic magnetic and physical properties of magnetic microstructures.

1.2 Chapter summary

In this section, after giving a brief overview, a summary of the chapter contents will be given.

Defining the concept of spatial resolution within a ferromagnetic sample, and understanding how FMRFM can provide local imaging, are complicated issues. The resonance fields and the amplitudes of ferromagnetic modes involve complicated interactions between the sample, the external fields, and the probe magnet. There are three major components which are essential to the understanding of the physical principles of spatial resolution and sensitivity in FMRFM. First, FMRFM must be developed to provide the ability to measure the ferromagnetic resonance (FMR) of microscale samples. The resonances obtained experimentally must correspond with values expected from established theories. Second, simple models must be developed to determine the resonances of microstructures, which have not been analyzed on this scale before, and verified experimentally. Third, the gradient field of the probe magnet must be increased to interact with the sample strongly enough to create local perturbations in the ferromagnetic resonance. Observing these deviations from the weak gradient field limit, which are established in the two components stated above, is a crucial first step toward understanding FMRFM in the high gradient field limit where the ferromagnetic resonance becomes locally determined. In this regime, FMRFM imaging becomes analogous with that of EPR MRFM. A simple theoretical model to explain the observed effects must be developed. A detailed analysis of YIG microstructures has been performed to obtain these three components.

In Chapter 2, the theories of MRFM and FMR are presented. It starts with the underlying physical mechanisms of spatial resolution for EPR and NMR MRFM to illustrate the general MRFM technique. Then, two established theories of FMR are reviewed: (1) the continuum model for thin metallic films (≤ 1000Å) and (2) the magnetostatic wave theory for thicker samples such as YIG ($1 - 3\mu m$). A simple model for microscopic films, which have comparable width and thickness, is developed from the magnetostatic mode theory.

At the end of Chapter 2, the major physical differences and challenges of FMR versus EPR and NMR MRFM are discussed. Possible effects of a high gradient field and the magnetic coupling on the sensitivity and spatial resolution in the sample are introduced.

In Chapter 3, the experimental apparatus and measurement techniques are discussed in detail. Particular characteristics of the FMRFM apparatus, such as the noise floor of the fiber optic interferometer and the uniformity of the RF field, are analyzed. The limitations on the sensitivity of MRFM due to various noise sources within the apparatus are explored. The technological advances in detection methods developed during the course of this study, such as NiFe-tipped cantilevers and large structure microstrip resonators, are also presented.

In Chapter 4, the physical principles underlying spatial resolution and sensitivity in FMRFM are established for two regimes, first the low gradient field limit and then the high gradient field limit. The data and the analysis is presented approximately in the order of the three components detailed earlier. The resonances obtained in the early YIG experiments are in qualitative agreement with theoretical expectations. Mapping of mode amplitudes within the sample, attained with an unprecedented spatial resolution of $15\mu m$, are described. These results demonstrate the ability of FMRFM to measure ferromagnetic resonance in microscopic samples and to provide spatial resolution of magnetostatic modes within the samples. A detailed analysis on a microscale geometrical series of YIG is described. The ferromagnetic resonances obtained experimentally agree with expected values from a simple model developed for microstructures in Chapter 2.

Chapter 4 also includes descriptions of experiments in which the gradient field at the sample is increased by bringing the probe magnet within a few microns of the sample surface. Local perturbations in the sample are found to yield deviations in the resonance measurements from the expected values established earlier in the chapter. A simple model to qualitatively account for the observed effects is developed.

Chapter 5 describes experiments that demonstrate the ability of FMRFM to characterize the magnetic properties of multilayer metallic films, similar to those used in GMR devices. The thickness, anisotropy energies, and interface qualities of *individual* layers are determined. The observed values of volume and surface anisotropy energies are shown to fall within values recently reported in the literature.

This study of spatial resolution in FMRFM is concluded in Chapter 6. FMRFM is differentiated into two limits involving either *weak* or *strong* local gradient fields. The physical mechanisms governing FMR imaging and spatial resolution within these two regimes are discussed. Finally, prospects are explored for future FMRFM experiments that expand on the observations and simple theories developed in this thesis.

Appendix A includes a table of the notation used in this thesis. The theory of thermal noise and sensitivity in mechanical resonators is presented in Appendix B. The processing details for the YIG samples and NiFe-tipped cantilevers are described in Appendix C. The calculations of the demagnetization of microstructures are in Appendix D. Finally, a discussion of an alternate mechanical force detector, magnetic films on high frequency beams, and preliminary experiments to demonstrate their feasibility, are included in Appendix E.

2 FMRFM: Development and understanding

The theoretical development and understanding of ferromagnetic resonance force microscopy (FMRFM) are presented in three sections. First, the application of magnetic resonance force microscopy to NMR and EPR is presented. The basic theory of detection, and several of the measurement techniques, are the same for both methods. The underlying physics of the spatial resolution and sensitivity in EPR MRFM is more straightforward than that of FMRFM. The unique challenges for force detection posed by ferromagnetically coupled systems will be compared to the simpler and better studied field of EPR MRFM.

Second, the theory of ferromagnetic resonance (FMR) is presented using two different approaches. The continuum model best illustrates the dependence of the dispersion relation upon anisotropy energies, sample thickness, and the angle of the external field relative to the sample plane. This model is used when characterizing the fundamental mode in thin metallic films in Chapter 5. Then, the magnetostatic mode model develops the dependence of the dispersion relation upon all of the sample dimensions (not just the thickness). A simple model is derived for the resonance fields of the fundamental and higher order modes of YIG microstructures.

Third, the key differences of FMRFM versus EPR and NMR MRFM, which arise from the ferromagnetic coupling within the sample, are discussed. Possible observable effects from the coupling on the dispersion relation are considered.

2.1 MRFM

2.1.1 Basic theory (parallel geometry)

When a magnetic moment $\vec{M}$ is placed in a static external magnet field $\vec{H}$, it will precess about the field axis with an intrinsic frequency ω until damping parameters bring the moment into alignment with the field. The relationship between $\vec{H}$ and ω is called the dispersion relation. For this simple system, the dispersion relation is $\omega = \gamma H_{res}$, where γ is the gyromagnetic ratio and H_{res} is the magnetic field at resonance. External energy can be added to the system to enhance the precession by applying an external RF magnetic field, H_{rf}, with a frequency of ω, parallel to the precession plane. In conventional magnetic resonance measurements, the resonance is detected inductively, such as through the absorption of the RF power [12].

In MRFM, the magnetic resonance is detected mechanically, rather than inductively. A schematic of a MRFM set-up is shown in Figure 2.1 [1]. Electromagnetic coils (not shown) provide an external field $H\,\hat{z}$ which can be swept. A modulation coil (not shown) produces a small field modulation field $H_{\rm mod}(t) = H_{\rm mod} \sin \omega_{\rm mod} t\ \hat{z}$. A small probe magnet produces a gradient field. The total external magnetic field at the sample is $\vec{H}_{total} = \vec{H}(r)_{probe} + \vec{H} + \vec{H}_{\rm mod}$. A small RF coil, which enhances the spin precession, produces a field H_{RF} perpendicular to $\hat{z}$.

Mechanical detection

Mechanical detection requires two main components, as shown in Figure 2.2. First, a magnetic moment $\vec{M}$ in a gradient field ∇H will experience a force, $F = (\vec{M} \cdot \vec{\nabla})\vec{H}$. The gradient field is supplied by a small probe magnet mounted to a mechanical resonator (i.e., a cantilever). The spins in the sample produce a moment $\vec{M}$ which interacts with the gradient field, thus producing a force on the mechanical resonator. For the orientation of the external fields and the cantilever shown in Figure 2.2(b), the force on the cantilever is

$$F_z = M_z \frac{\partial H}{\partial z} \hat{z}, \tag{2.1}$$

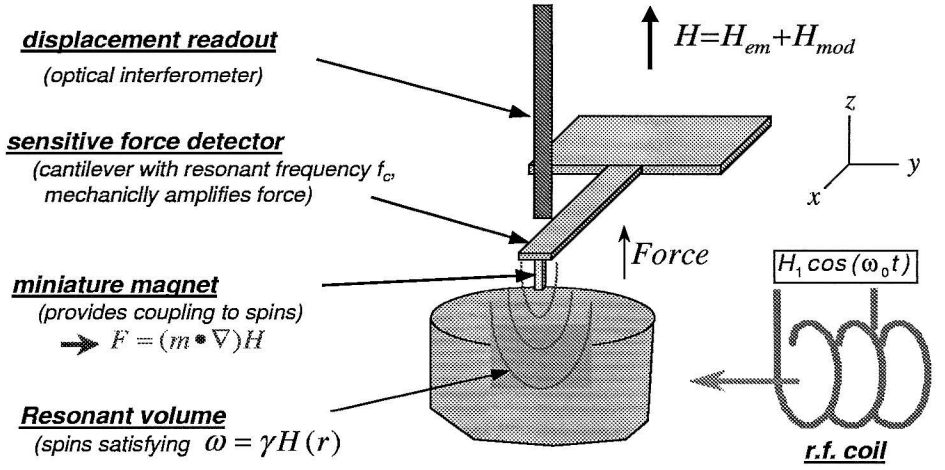

Figure 2.1: A schematic of a MRFM apparatus, and the key ingredients of detection. See text for details.

where M_z is magnitude of the magnetic moment in the direction of the cantilever deflection. The force in the x and y directions are neglected in this case since the cantilever can only deflect in the z direction..

Second, the amplitude of the magnetic moment M_z is modulated such that the resulting force varies at the resonance frequency of the mechanical resonator, f_c. The mechanical resonator is driven by the time varying force, $F(f_c) = M_z(f_c)\left(\frac{\partial H}{\partial z}\right)$. The magnitude of M_z is determined by the magnetic resonance condition and the external and RF fields. Thus, the small time variation in the amplitude of M_z can be produced by modulating the amplitude of the RF field H_{RF}, modulating the external field H_{mod}, or a combination of the two (see section "anharmonic modulation"). The response of the cantilever to the driving force is enhanced by its quality factor, Q. In short, the gradient field couples the precessing magnetic moments to the cantilever, the cantilever responds mechanically to the precessing moments, and the Q of the cantilever enhances the magnetic resonance signal.

The force response is detected by measuring the oscillation amplitude of the cantilever at f_c using an optical fiber interferometer and a lock-in amplifier. Thus, on resonance, the

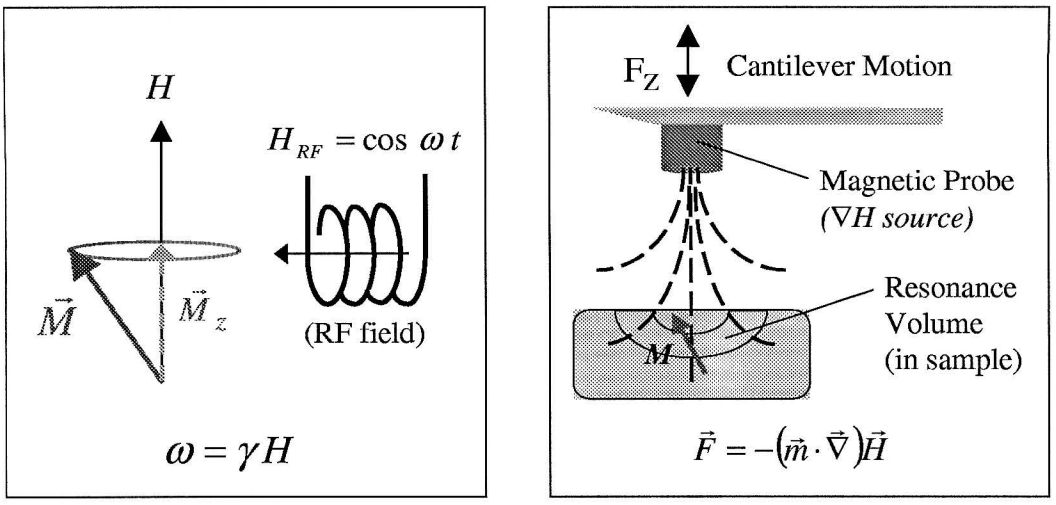

Figure 2.2: (a) The resonance condition, $\omega = \gamma H_{res}$, of a magnet moment $\vec{M}$ in an external field H. Energy supplied by an RF coil enhances the precession. (b) The gradient field ∇H is coupled the precessing magnetic moment $\vec{M}$ in the sample to produce a force on the cantilever. The gradient field also creates a local volume of field, centered on H_{res}, in which the resonance condition is met.

MRFM signal is given approximately by

$$A_{\max} = \frac{F_0 Q}{k} = m_z \left(\frac{\partial H}{\partial z} \right) Q/k, \tag{2.2}$$

where $A_{\max}$ is the maximum oscillation amplitude to first order, $F(t) = F_0 \sin \omega_c t$, and k is the force constant of the cantilever. In practice, the dependence of the modulated magnetic moment, $M_z(t)$, is a complicated function whose magnitude depends on the resonance line width of the sample the applied fields (H, H_{RF}, and H_{mod}) [13].

Spatial resolution

In conventional magnetic resonance imaging of NMR and EPR, spatial resolution is determined by the volume of space over which the magnetic resonance condition is satisfied. In MRFM, this volume is determined by the gradient field, ∇H, from the probe magnet and

the resonance line width, ΔH, of the sample. The volume of magnetic resonance, often called the "sensitive slice," determines the spatial resolution of EPR and NMR MRFM.

In theory, either the RF frequency ω or the total field H can be swept to obtain a resonance spectrum. In practice, the RF frequency ω is fixed and the external field, H, is swept through the resonance condition. The gradient field of the probe magnet adds a small local field which varies in space, $\delta H(r)$, in the vicinity of the sample. The total field which must satisfy the magnetic resonance condition is now $H_{total}(r) = H + \delta H(r)$. Thus, as the external field is swept, only the spins at r satisfying the magnetic resonance condition at $H_{total}(r) = H_{res}$ will resonate. i.e., the field is swept spatially through the sample.

The sample resonance has a finite line width, ΔH, centered at the resonance field H_{res}. The intrinsic line width, due to spin-spin coupling and other factors [14], increases the volume of space where the magnetic resonance condition can be satisfied by the external fields. The resolution, Δx_i, in NMR and EPR MRFM is defined as:

$$\Delta x_i = \frac{\Delta H}{\nabla H_i} = \frac{\Delta H}{\frac{\partial |\vec{H}|}{\partial x_i}}. \tag{2.3}$$

The resonance condition is a *local* function of the applied field – only spins within this volume will resonate and contribute to the time varying force on the cantilever.

Limits of sensitivity

The fundamental limit to the force sensitivity of MRFM is the thermal (or, ultimately, quantum) fluctuations in the mechanical force detector [see Appendix B]. The force on the detector created by the magnetic moments and the gradient field cannot be resolved if it is smaller than the thermal force noise. The sensitivity of the MRFM can be described by the minimum number of spins (having spin I and gyromagnetic ratio γ) in the resonance volume that produce a force equal to the thermal force noise, yielding a signal-to-noise ratio (SNR) of unity. Assuming a sample with Curie-law susceptibility, the minimum detectable signal, N_{MDS}, is [8]

$$N_{MDS} = \frac{S_F^{1/2}\,(\Delta f)^{1/2}}{F_{spin}} = \left[\frac{1}{|\nabla H|}\right] \cdot \left[\frac{3k_B T}{(h\gamma)^2\, I\,(I+1)\, H}\right] \cdot \left[\sqrt{\frac{2k\, k_B T\ \Delta f}{Q\ \omega_c}}\right], \tag{2.4}$$

where $S_F^{1/2}$ is the thermal noise spectral density of the cantilever, Δf is the measurement bandwidth, F_{spin} is the force per spin (from $F = (\vec{M} \cdot \vec{\nabla})\vec{H}$), k_B is Boltzmans constant, T is the absolute temperature, Q and k are the quality factor and force constant of the cantilever, and ω_c is the resonance frequency of the cantilever. The first term on the right is the physical mechanism by which the magnetic moment is coupled to the cantilever. The second term is simply the inverse spin polarization of the sample. The third term is the thermal force sensitivity of the cantilever. In Eq. 2.4, other sources of noise are ignored. It is further assumed that the readout of the signal (the displacement transducer) is itself noiseless. At room temperature, the engineering to insure the dominance of the noise by thermal fluctuations is straightforward and discussed in Chapter 3.

To improve force sensitivity, there are four engineering parameters that can be optimized: (1) increase the gradient field ∇H, (2) lower the temperature T, (3) increase the quality factor Q of the mechanical resonator, and (3) lower the force constant k or increase the frequency ω_c of the mechanical resonator. However, changing one parameter to improve signal strength often results in an adverse change in a related parameter. The sensitivity (N_{MDS}) and the resolution must be considered together, along with the spin density of the sample, to determine if the signal strength is greater than the thermal noise. In determining the optimal cantilever design and requisite gradient field to detect resonance in a sample, the following considerations are important:

- To detect a small number of spins, a large magnetic gradient field (∇H) is necessary to produce a large force on the cantilever (Eq. 2.4). However, increasing the gradient field decreases the resonant volume (Eq. 2.3). The relevant relations are

$$\text{Force: } F \propto \nabla H, \qquad \text{Resolution: } \Delta x_i \propto \frac{1}{\nabla H_i} . \tag{2.5}$$

  If the density of magnetic moments within the sample is not large enough, there will not be enough spins in the resonance volume to create sufficient force to exceed the thermal noise. Early experiments utilized low gradient fields ($\approx 0.1\,T/m$) to create sufficiently large resonance volumes.

- The force constant k of the mechanical force detector can be reduced by altering

its dimensions. While reducing k increases sensitivity of the mechanical resonator to small forces, it also reduces the resonance frequency ω_c. Low frequencies will create long ring up/down times, drastically reducing the speed of data acquisition unless feedback is employed [15]. The relevant equations to consider when designing the mechanical force detector are:

$$k \propto w\left(\frac{t}{L}\right)^3, \qquad \omega_c \propto \left(\frac{t}{L^2}\right) , \tag{2.6}$$

where w, L, and t are the width, length, and thickness of the mechanical resonator. Furthermore, the force from the resonance spins must remain coherent over the ring up/down time of the force detector in order for it to respond to the signal. This will be especially important for pulsed NMR, where the decay time length must exceed, or be on the same order, as the ring up/down time. Low frequency mechanical resonators, which have increased sensitivity but have long ring up/down times, greatly limit the applicability of MRFM to a narrow range of samples. These requirements can be balanced to find appropriate values of ω_c and k which increase the sensitivity, but still maintain a reasonably high frequency and low force constant [see Appendix B-table].

The ultimate resolution of MRFM may well be the detection of a single nuclear spin. Neglecting polarization factors, a SNR of 1 ($N_{MDS} = 1$) for a single nuclear spin can be obtained with (approximated for a doubly-clamped beam mechanical resonator) $\nabla H = 10^6\, T/m$, $\omega_c = 3\, MHz$, $k = 3\, N/m$, $Q = 10^6$, $T = 50\, mK$, and $\Delta f = 0.1\, Hz$. Theoretical complications, such as coupling to a single spin, are outside the scope of this thesis but are being pursued in our research group. A more in-depth description of MRFM can be found in Hammel *et al.*[8] and Sidles [9].

2.1.2 Early EPR experiments (DPPH)

Early experiments in MRFM (and FMRFM) were performed with the sample affixed to the cantilever. The gradient field was supplied by a small, but macroscopic, permanent NdFeB

magnet located near the sample. From Newton's third law, the force $[\vec{F} = (\vec{M} \cdot \vec{\nabla})\vec{H}]$ acts equally on the sample or the magnet, but it is ultimately dissipated within the part of the system that can move, such as the cantilever.

First experiments of MRFM were performed with small particles of 2,2-diphenyl-1-picrylhydrazyl (DPPH), an organic material with a single unpaired electron per molecule, glued to the end of a commercial cantilever. DPPH is the "standard sample" used in EPR. In Figure 2.3 (top), the swept field spectrum is shown for a single particle of DPPH approximately $18\mu m$ in diameter ($5ng$) and containing $8x10^{12}$spins. The signal force is $\sim 3x10^{-15}N/m$ for the experimental conditions $|\nabla H| = 0.8\,G/\mu m$, $\omega_{rf} = 709\,MHz$, and $H = 253\,G$. The calculated thermal noise of the cantilever ($T \cong 300K$, $Q = 3x10^4, k = 0.08\,N/m$) is $\sim 4.1x10^{-16}N/m$, which agrees well with the observed signal [16].

For EPR, only the spins within the resonance volume, as determined by Eq. 2.3, will contribute to the MRFM signal. Thus, two separate particles in a magnetic gradient field will resonate at different fields as the external field is swept. A spatial resolution of $1\mu m$ and a sensitivity of $3x10^{11}$ spins was demonstrated by placing two DPPH particles on the cantilever separated by the $1 - 3\mu m$ thickness of the cantilever (Figure 2.3 (bottom)) [16].

2.2 FMR theory

In a ferromagnetic sample, the resonance frequency ω and the equilibrium position of the magnetic moments $\overrightarrow{M}$ not only depend upon the externally applied field H, but also on the total internal magnetic field H_i. The internal field results from anisotropy energies (crystalline and surface effects), exchange coupling (spin-spin interactions), and demagnetization energies (dipole-dipole interactions). Thus, the dispersion relation is no longer a simple function of only the local external field. Instead, it depends upon a fairly complicated relation between: the external and internal fields; on the sample shape and size; and the sample's orientation to the external field.

There are several ways to solve for the dispersion relation [17]. In the following sections, three methods will be discussed: (1) the continuum model for metallic films (less than 1000Å), (2) the magnetostatic wave theory for thicker samples such as YIG ($1-3\mu m$), and

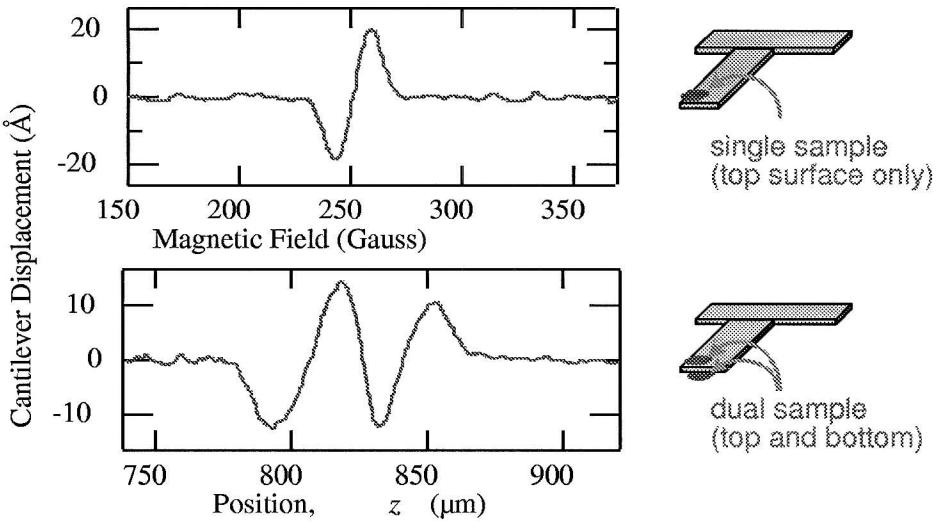

Figure 2.3: The EPR/MRFM spectrum of DPPH, mounted on a commercial Si cantilever $440x40x3\mu m$. (a) Single shot signal from a 18 μm diameter DPPH particle as the bias field is swept. (b) The signal from two DPPH particles, 7ng (above) and 3ng (below). The amplitude of the cantilever oscillation is shown as a function of distance, z, from the end of the gradient magnet to the volume in which the resonance condition is satisfied. Observations of two distinct signals demonstrate a one-dimensional "imaging" resolution of order $1\mu m$. The cantilever has a resonance frequency in vacuum of $8.8\,kHz$ and a Q of 20,000. The RF frequency is $825\,MHz$. After Hammel [16].

(3) the magnetostatic mode theory further approximated to model microscopic samples which have comparable dimensions in width and thickness – systematic analysis of the mode spectra at these micron dimensions have never before been realized. These three derivations highlight important experimental characteristics of the different sample types that are included in this study.

2.2.1 Continuum model (thin metallic films)

The continuum model [17] is a useful method to determine the dispersion relation of thin magnetic films (thickness << width, length), where surface anisotropies can have a signifi-

cant effect. It starts from the torque equation of motion

$$\frac{1}{\gamma}\frac{d\overrightarrow{M}}{dt} = \overrightarrow{M} \times \overrightarrow{H}_{eff}, \tag{2.7}$$

where

$$\vec{H}_{eff} = \vec{H} - \vec{H}_u + \vec{H}_d + \vec{H}_{ex} + \vec{h}\exp(-i\omega t), \tag{2.8}$$

γ is the gyromagnetic ratio, $\vec{H}_{eff}$ is the total effective field, $\vec{H}$ is the external field, $\vec{H}_u$ is the uniaxial anisotropy field, $\vec{H}_d$ is the demagnetization field, and $\vec{H}_{ex}$ is the exchange field. $\vec{h}$ is the transverse RF component of the field created by the RF component of the sample's magnetic moment, $\vec{m}$. ($\vec{h}$ is not the same as $\vec{H}_{rf}$, the RF field created by the coils or microstrip.) For the simplest case, a single magnetic moment $\overrightarrow{m}$ in a pure external magnetic field $H\,\hat{z}$, the moment precesses about the z axis with frequency $\omega = \gamma H$. However, for a ferromagnetic material, the dispersion relation is much more complicated due to field contributions at each magnetic ion site. These contributions not only include the external field $\vec{H}$, but also the anisotropy energy K (the energy dependence of the orientation of the ion spin with respect to the crystalline axis, surface stresses or other effects); the exchange field $\vec{H}_{ex}$ (due to spins of nearby ions); and the demagnetization field $\vec{H}_d$ (the long range dipole interaction due to spins throughout the rest of the sample).

The torque due to these contributing magnetic fields can be treated in terms of the free energy density of the system, $E(\vec{r})$, through the relation $\tau = \hat{e}_r \times (-\nabla E)$ [18]. Using this expression, the effects of the applied, anisotropy, and demagnetization fields can be treated as scalar contributions to the energy density and dependent upon orientation, rather than as vector fields. The torque equation of motion (Eq. 2.7) can be expressed in orientation and exchange energies and written as [17]

$$\begin{gathered}\frac{d\overrightarrow{M}}{dt} = \gamma\frac{\vec{M}}{M_S} \times \vec{\nabla}E + \gamma\frac{2A}{M_S^2}\vec{M} \times \nabla^2\vec{M}, \\ \text{(orientation)} \qquad \text{(exchange)}\end{gathered} \tag{2.9}$$

where E is the total energy due to the applied, anisotropy, and demagnetization fields; A is the exchange coupling constant; and M_S is the saturation magnetization of the sample.

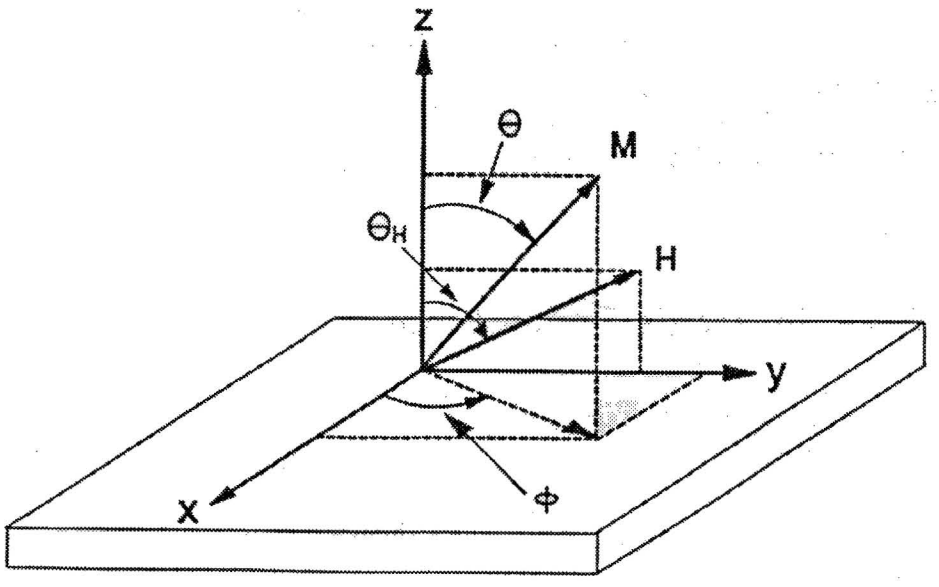

Figure 2.4: Coordinate system used in thin films. After Zhang [19].

Polar coordinates are used, where the z axis is perpendicular to the film plane, as shown in Figure 2.4.

Orientation Energies

The following orientation energies (the first term on the right — hand side of Eq. 2.9) will be considered, as derived by P.E. Wigen [17], and later in further detail by Z. Zhang [19].

1. Zeeman energy. This is the energy of a magnetic moment in an external magnetic field.

$$E_Z = -\vec{M} \cdot \vec{H} = -M_S H \left[\cos\theta_H \cos\theta + \sin\theta_H \sin\theta \cos\left(\phi - \phi_H\right)\right]. \tag{2.10}$$

2. Demagnetization energy. This is the local field at a magnetic ion site created by the long range dipole moments of all the other magnetic ions in the sample. For a sample in a magnetic field, the moments align such that there will be an internal field

opposing the external field. For an thin film, the demagnetization field is negligible in the lateral directions but has significant contributions in the direction of the film thickness [14]. In the coordinate system used here (Figure 2.4), the demagnetization energy is expressed as

$$E_D = 2\pi M_z^2 = 2\pi M_S^2 \cos^2\theta. \tag{2.11}$$

3. Uniaxial anisotropy energy. Physical properties of the sample produce preferred spin orientations. Only properties which produce energy contributions due to the magnetic field orientation with respect to the normal to the film plane (z axis) will be considered in this derivation. Anisotropy energies in the plane of the film (x and y axes) will not be considered. Typical sources of anisotropy energies which contribute to the orientation energies are:

   - Magnetocrystalline energies. Spins in a crystal lattice will have a preferred orientation to minimize energy. The energies arise from spin-orbit coupling and the chemical bonding of the atomic orbitals in the crystal. The atomic orbitals have preferred orientations due to interactions with the electronic wave functions of their surrounding ions. Spin-orbit coupling (for ions with $L_z \neq 0$) will result in the spins also having a preferred direction with respect to the crystal axes. The metallic films in this study are polycrystalline films. Thus, their magnetocrystalline energies are randomized and will not exhibit a coherent dependence upon the magnetic field orientation. The YIG films in this study are cubic crystals grown on (1,1,1) substrates which result in the c-axis perpendicular to the film plane. Thus, the YIG will have a contribution to the uniaxial anisotropy energy from the magnetocrystalline energy.
   - Surface effects. At the surface there is often stress and differences in the separations of the atoms due to a lack of atoms on one side of the surface. As a result, there will be a change in the exchange interaction of the spins near the surface. These spins react differently to magnetic torques, and will contribute to the uniaxial anisotropy energy.

- Magnetoelastic effects. The interface of the substrate and the magnetic material will produce stress due to lattice mismatch. Atomic spacing is reduced or increased, thus changing the local magnetic moment $\vec{M}(r)$. This will also contribute to the uniaxial anisotropy energy.

The uniaxial anisotropy energy can be expressed as

$$E_A = K_{u2} \sin^2 \theta + K_{u4} \sin^4 \theta + ..., \tag{2.12}$$

where K_{ui} are the uniaxial anisotropy energy constants. For most materials, the first term is dominant, and the third and higher order terms are usually small and can be neglected. Using the relation $\nabla \cos^2 \theta = \nabla \left(1 - \sin^2 \theta\right) = -\nabla \sin^2 \theta$, the total orientation energy can be expressed as

$$E = -M_S H \left[\cos \theta_H \cos \theta + \sin \theta_H \sin \theta \cos \left(\phi - \phi_H\right)\right] + K^{eff} \sin^2 \theta, \tag{2.13}$$

where $K^{eff} = K_{u2} - 2\pi M_S^2$.

Exchange Energy (Heisenberg Hamiltonian)

The second term on the right — hand side of the torque equation (Eq. 2.26) is an exchange energy. Dirac showed that for localized electrons in orthogonal orbits, the effect of the Pauli exclusion principle was equivalent to introduction of a spin-dependent energy term in the Hamiltonian of the form [20]

$$\mathcal{H}_{ex} = -2 \sum J_{i,j} S_i \cdot S_j. \tag{2.14}$$

The sum on i and j is over all lattice sites, and the exchange strength $J_{i,j}$ is restricted to nearest neighbor sites due to the small spatial extent of atomic wavefunctions. This is known as the Heisenberg Exchange Hamiltonian. The important physical variable is the relative angle between spins. This energy accounts for spin waves with wavelengths on the order of submicrons (not sample dimensions, such as magnetostatic modes).

The large exchange interaction in ferromagnetic materials results a minimum energy when the spins are parallel to each other. Any disturbance in the spin system that results in small changes in the relative orientation of the spin from one lattice site to the next will produce a restoring torque between the two spins. The exchange Hamiltonian can be expanded as a variation of the neighboring spin S_j in a Taylor series about S_i and the position i [19]:

$$\mathcal{H}_{ex} \simeq 2zJ\sum S_i^2 - J\sum S_i \cdot [(\vec{r}_j - \vec{r}_i)\cdot\nabla]^2 \vec{S}_i + \ldots . \tag{2.15}$$

where z is the number of nearest neighbors and J is the exchange strength. The first term is a ground state, and will not contribute to the torque equation since its derivative is zero. The second term represents a torque which will contribute to the equation of motion. The characteristic length of the disturbance is much larger than the lattice spacing, so derivatives of higher order terms are small and can be neglected. Using the relation $\vec{M} = N(g\mu_B\vec{S})$, where $g\mu_B\vec{S}$ is the magnetic moment of each spin and N is the total number of spins, the exchange energy can be expressed as

$$E_{ex} = -\frac{2A}{M_S^2}\vec{M}\times\nabla^2 M, \tag{2.16}$$

where A is the coupling constant. (For a cubic crystal, $A = \frac{zJS^2}{a}$.)

Solving the Equation of motion There are two main steps to obtaining a solution to the torque equation (Eq. 2.7) for a thin film geometry.

First, the equilibrium position of the magnetic moment, $\vec{M}(\theta_0, \phi_0)$, is determined and defined by the equilibrium orientation angles θ_0 and ϕ_0. In equilibrium, the spins are aligned with the effective field, a combination of the external, anisotropy, and demagnetization fields. Applying the static condition $\vec{M}\times\vec{H}_{eff} = 0$, the left side of the torque equation equals zero ($\frac{dM}{dt} = 0$). The exchange term also equals zero, for $\vec{K}, \vec{M} \neq F(z)$, since the

spins are parallel. Thus, the only contribution comes from the orientation energies [19], where θ_0 and ϕ_0 satisfy the equations

$$\begin{aligned} H\sin(\theta_0-\theta_H)+H_{eff}\sin\theta_0\cos\theta_0 &= 0 \\ \phi_0 &= 0. \end{aligned} \tag{2.17}$$

Second, the system is perturbed. Assuming small precession amplitudes about the equilibrium point, the equation of motion is linearized. The magnetic moment is assumed to have both a frequency and a spatial response of the form

$$\begin{aligned} M &= M_S\hat{e}_r + m_\theta\hat{e}_\theta + m_\phi\hat{e}_\phi, \\ m_{\theta,\phi} &= m_{\theta_0,\phi_0}e^{-i(\omega t-k\cdot r)}, \end{aligned} \tag{2.18}$$

where ω is the precession frequency and $\vec{k}$ is the wave number. Only spin waves in the z direction (normal to the film plane) will be considered. Spin wave numbers (k_y, k_x) in the x and y directions correspond to wavelengths of order of the films lateral dimensions, which are much larger than the film thickness. The exchange energy for modes in the lateral directions are negligible compared to the mode energy the z direction. (i.e., $\frac{2A}{M_S}k_{x,y}^2 << \frac{2A}{M_S}k_z^2$, where $k_i = \frac{n\pi}{x_i}$.) Thus, the approximation $\vec{k}\cdot\vec{r} \approx k_z z$ is valid for thin films.

The torque equation of motion is solved by linearizing Eq. 2.26 about the equilibrium position (Eq. 2.17). Keeping only first order terms (terms containing second derivatives), a pair of coupled equations is obtained. The notation $E_{\theta\theta} = \frac{\partial E}{\partial\theta\partial\theta}$, $E_{\phi\phi} = \frac{\partial E}{\partial\phi\partial\phi}$, $E_{\theta\phi} = \frac{\partial E}{\partial\theta\partial\phi}$ is used, where E is the total orientation energy (Eq. 2.13). Evaluating at the equilibrium positions, $\theta = \theta_0$ and $\phi = \phi_0$, the following coupled equations are obtained:

$$\begin{aligned} \frac{1}{\gamma}\frac{dm_\theta}{dt} &= -\frac{E_{\theta\phi}}{M_S\sin\theta}m_\theta - \frac{E_{\phi\phi}}{M_S\sin^2\theta}m_\phi - \frac{2A}{M_S}\nabla^2 m_\phi \\ \frac{1}{\gamma}\frac{dm_\phi}{dt} &= \frac{E_{\theta\theta}}{M_S}m_\theta + \frac{E_{\theta\phi}}{M_S\sin\theta}m_\phi + \frac{2A}{M_S}\nabla^2 m_\theta \end{aligned} \tag{2.19}$$

Solving the above coupled equations, and assuming that m_θ and m_ϕ have the form $e^{-i(\omega t-k_z t)}$ 4.20, the dispersion equation, within these approximations, is

$$\left(\frac{\omega}{\gamma}\right)^2 = \left(\frac{E_{\phi\phi}}{M_S\sin^2\theta}+\frac{2A}{M_S k_z^2}\right)\left(\frac{E_{\theta\theta}}{M_S}+\frac{2A}{M_S}\right) - \frac{E_{\theta\phi}^2}{M_S^2\sin^2\theta}\ . \tag{2.20}$$

Damping terms have been ignored because they do not affect the dispersion relation [17][19]. However, damping (spin relaxation) does affect the line width of the resonance. At room temperature, the line widths for NMR and EPR are typically only a few gauss. The line widths for FMR in metals are typically 50-200 gauss [19]. FMR line widths can vary from $1G$ for YIG up to more than $1000G$ for complicated alloys.

Special Case - the uniform (fundamental) mode

The lowest energy mode is defined as the fundamental mode. For the case when the fundamental mode is the uniform mode, $k_z = 0$. All the spins precess uniformly throughout the sample. Calculating the requisite derivatives from Eq. 2.13, and evaluating them at $\theta = \theta_0$, $\phi = \phi_0$, yields the simplified dispersion relation

$$\left(\frac{\omega}{\gamma}\right)^2 = H\left[H\cos\left(\theta_0 - \theta_H\right) + H^{eff}\cos\left(2\theta_0\right) + ...\right]\frac{\sin\theta_H}{\sin\theta_0}, \tag{2.21}$$

where $H^{eff} = \frac{2K^{eff}}{M_S}$ and $K^{eff} = K_{u2} - 2\pi M_S^2$. Note that the resonance condition explicitly depends on the angle of the external magnetic field relative to the film plane, θ_H. An example of the dependence in shown in Figure 2.5.

For H parallel to the film plane, the magnetization vector is parallel to the external field at equilibrium, so that $\theta_H = \theta_0 = 90°$. For this case, the dispersion equation can be calculated explicitly and is

$$\frac{\omega}{\gamma} = \sqrt{H\left(H - H_{eff}\right)}. \tag{2.22}$$

For H perpendicular to the film plane, both $\theta_H = 0°$and $\theta_0 = 0°$ if the external field is sufficient to saturate the magnetization. Using small angle approximations, one obtains for this state [19]

$$\frac{\omega}{\gamma} = H + H_{eff}. \tag{2.23}$$

A simple physical picture of this effect is as follows. The magnetization (at zero field) lies in the plane of the film as the lowest energy state. It requires energy to rotate $\vec{M}$

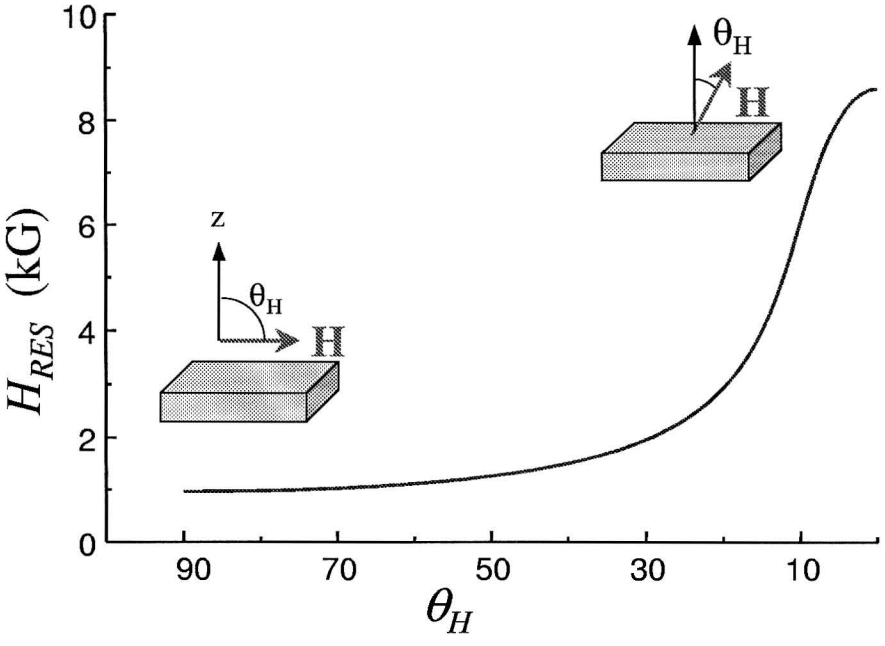

Figure 2.5: The external magnetic field required for resonance, H_{res}, as a function of the angle bewteen the external field and the sample plane.

out of the film plane against the demagnetization and anisotropy energies. Thus, when a perpendicular field is applied to the sample to rotate $\vec{M}$ out of the film plane, a higher field is required for magnetic resonance.

Experimental characterizations of FMR in magnetic films

For devices consisting of metallic magnetic films, their performance depends critically upon bulk and surface anisotropy energies, and thickness. The anisotropy energies, which reflect the quality (or smoothness) of the surface and interfaces, can only be measured with FMR techniques. Improvements in sample preparation techniques have resulted in devices much smaller than the lateral areas of a few mm^2 required for detection with traditional FMR techniques.

The FMRFM technique, however, has the potential to detect and characterize, both the anisotropy energies and thickness, of samples with lateral areas of a few μm^2. In order to

test the abilities of FMRFM, three main measurements were performed that characterized important properties of metallic films:

1. Anisotropy energies: From the above dispersion relations (Eqs. 2.22 and 2.23), and from the relation $H^{eff} = \frac{2K^{eff}}{M_S} = \frac{2\left(K_{u2} - 2\pi M_S^2\right)}{M_S}$, the uniaxial anisotropy energy (K_{u2}) can be measured.

2. H_{res} as a function of θ_H. The dependence of the resonance field on the angle of the external field relative to the film plane can be measured. From Eq. 2.21,

$$\left(\frac{\omega}{\gamma}\right)^2 = H\left[H\cos\left(\theta_0 - \theta_H\right) + H^{eff}\cos\left(2\theta_0\right)\right]\frac{\sin\theta_H}{\sin\theta_0}. \tag{2.24}$$

   This also serves as a measurement of the anisotropy energies.

3. H_{res} as a function of thickness: Typically, the resonance of films thinner than 100Å will have a dependence on thickness [20]. For a given sample, the internal field of the surface spins may differ slightly from the bulk spins. The effective anisotropy constant, K_{eff}, can be expressed as a bulk value, K_V, plus an additional surface term K_S. The bulk anisotropy energy density, K_V, operates uniformly throughout the film and includes magnetocrystalline and magnetostatic terms. K_S is an energy per unit area localized at the surface which may arise from spin-orbit contributions or strains at the surface [20].

   The bulk spins want to precess at the frequency associated with its internal field, a combination of the external and bulk anisotropy fields. Due to the strong exchange interaction, the bulk spins drag the surface spins along with them. Similarly, the same effect occurs for the surface spins. If the thickness is less than the magnetic correlation length ($\sim$ 100Å for metallic films), the bulk spins precess at a frequency due to their internal field, plus a contribution due to the different internal field of the surface spins which is averaged over the volume of the sample. The volume varies linear with the thickness, so the effect of the surface term varies inversely with the thickness of the sample. In this regime, the effective anisotropy energy is defined by

the empirical formula [21]

$$K_{eff} \approx \left(K_V + \frac{2\ K_S}{M_S\ \ t_{film}} \right), \tag{2.25}$$

where t_{film} is the thickness of the film.

2.2.2 Magnetostatic modes (YIG studies)

Magnetostatic modes are spatial variations of the RF component of the magnetic moment $\vec{M}(r)$ that have wavelengths on the order of the dimensions of the sample. They can be thought of as standing waves of the magnetization magnitude across the sample. For sample dimensions larger than a few microns, the exchange energy of the wave (Dk^2) is negligible. In this regime the magnetic excitation is dominated by magneto-static energy rather than exchange energy.

Magnetostatic wave theory was first introduced by White and Solt [22] and Walker [23] for spheroidal samples. Damon and Eschbach (DE theory) [24] later adapted the theory to thin films infinite in lateral dimensions but finite in thickness. Here, they restricted the wave number k along the axis of the thickness d to the physical dimensions of the sample by the relation $k_z = \frac{n_z \pi}{d}$. Sparks [25] performed calculations using an alternative to DE theory which utilized Green's functions instead of separation of variables. Storey *et al.* [29] adapted DE theory to films finite in all three dimensions by restricting the wave numbers along the lateral dimensions in a similar fashion: $k_y = \frac{n_y \pi}{L}$, $k_x = \frac{n_x \pi}{w}$, where L = length and w = width. DE theory assumed an isotropic sample in a uniform field, and the inclusion of anisotropy energy was done by Akhiezer *et al.* [26] and Schnider [27]. Anisotropy is not considered in the derivation presented here, since its only effect is to add a constant offset to the resonance field and does not affect the field spacings between modes. The field spacing will be used to determine the accuracy of the data with respect to theoretical models.

Experiments measuring microwave absorption in thin YIG films were done by Tittmann [28], Storey *et al.* [29], and Borghese [30]. These samples, with thickness from a few

to tens of microns, had lateral dimensions of several hundreds of microns to millimeters – much larger than the samples in our studies. Such detailed analysis of ferromagnetic modes on the micron scale has not been achieved before. The high quality and narrow line widths of the microscale YIG structures included in this study are excellent for evaluating the ability of FMRFM to detect and to probe the ferromagnetic resonance properties of ordered magnetic materials at the micron level.

By neglecting the exchange interaction and anisotropy energies, the magnetization vector $\vec{M}(r,t)$ can now be solved for normal modes directly from the torque equation and Maxwell's Equations. These relation are now

$$\frac{1}{\gamma}\frac{d\overrightarrow{M}}{dt} = \overrightarrow{M} \times \overrightarrow{H}_{Eff}, \tag{2.26}$$

$$\text{where } \vec{H}_{eff} = \vec{H} - 4\pi\,\bar{N}\cdot\vec{M}_S + \vec{h}\exp(-i\omega t), \tag{2.27}$$

and $\bar{N}$ is the demagnetization tensor. The dynamic field, $\vec{h}$, has the same sinusoidal form as $\vec{m}$ (Eq. 4.20), and it may be viewed as the dipole field generated by the gradient of the dynamic magnetization $\vec{m}(\vec{r},t)$ inside the film (Eq. 2.8). $\vec{h}$ will be obtained from Maxwells equations and boundary conditions later in the derivation.

Dispersion relation for thin films

The derivation outlined below follows the models presented by Wigen [17], DE theory [24], and Hurben *et al.* [31]. The lengthy details of the derivation are not given here, but instead a general map for how the dispersion relation is obtained is given to illustrate the complexity of FMR as well as certain key points, such as the sinusoidal form of the solutions. For a more detailed derivation, see the references given previously [17][24][31].

For the external field, H, parallel to the plane of a thin sample, the demagnetization tensor reduces to $N_y = N_z = 0$, $N_x = 1$, and $N_{i,j\neq i} = 0$. Assuming small oscillations about

equilibrium as before, the approximate magnetization and fields, $\vec{M} = M_S\hat{e}_x + m_y\hat{e}_y + m_z\hat{e}_z$ and $\vec{H} = H_0\hat{e}_x + h_y\hat{e}_y + h_z\hat{e}_z$, are inserted into the torque equation (Eq. 2.26). Keeping first order terms in m and h results in a pair of coupled equations:

$$\begin{pmatrix} 4\pi m_y \\ 4\pi m_z \end{pmatrix} = \begin{pmatrix} \kappa & -i\nu \\ i\nu & \kappa \end{pmatrix} \begin{pmatrix} h_y \\ h_z \end{pmatrix}. \tag{2.28}$$

The terms κ and ν represent susceptibility functions which have the forms $\kappa = \frac{\Omega_H}{\Omega_H^2 - \Omega^2}$, $\nu = \frac{\Omega}{\Omega_H^2 - \Omega^2}$, $\Omega = \frac{\omega/\gamma}{4\pi M_0}$, and $\Omega_H = \frac{H_0}{4\pi M_0}$.

Maxwell's equations are used to introduce functional forms of $\vec{h}$ and $\vec{m}$, which will eventually lead to the introduction of sinusoidal and exponentially decaying solutions to the magnetostatic modes. These relations are

$$\vec{\nabla} \times \vec{h} = 0, \qquad \nabla \cdot \left(\vec{h} + 4\pi\vec{m}\right). \tag{2.29}$$

The condition $\vec{\nabla} \times \vec{h} = 0$ allows the introduction of a magnetic potential Ψ, where $\vec{h} = \nabla\Psi$. Applying separation of variables, this scalar potential takes the following forms inside and outside the sample:

$$\Psi^i(x,y,z) = X(x)Y(y)Z^i(z) = e^{ik_x x}e^{ik_y y}\left(a\sin(k_z^i z) + b\cos(k_z^i z)\right) \tag{2.30}$$

$$\Psi^e(x,y,z) = X(x)Y(y)Z^e(z) = e^{ik_x x}e^{ik_y y}c_{1,2}\exp(\mp k_z^e z) \tag{2.31}$$

The terms Ψ^i, k^i, Z^i are for internal values and Ψ^e, k^e, Z^e are external values. i.e., the magnetic potential Ψ^e is only applicable in the regions outside the film: $y > d/2$ or $y < d/2$, where d is the thickness of the film.

Both real and imaginary values for k_z^i are allowed. Real k_z^i values correspond to sinusoidal functions within the sample (volume modes), and imaginary k_z^i values correspond to functions which decay exponentially from the surface into the film (surface modes).

When the condition $\vec{\nabla} \cdot (\vec{h} + 4\pi\vec{m}) = 0$ is applied to the interior of the film, it leads to a simple differential equation for Ψ^i. Outside the film, the condition $\vec{m} = 0$, which implies

$\nabla \cdot h = 0$, leads to simple differential equations for Ψ^e. Using the functional forms for Ψ^i and Ψ^e (Eqs. 2.30, 2.31), the following coupled equations are obtained:

$$\begin{aligned} k_x^2 + (1+\kappa)\left[k_y^2 + (k_z^i)^2\right] &= 0 \\ \text{and } k_x^2 + k_y^2 - (k_z^e)^2 &= 0. \end{aligned} \tag{2.32}$$

By imposing the boundary conditions that the normal components of $\vec{b}$ and the tangential components of $\vec{h}$ must be continuous, the coefficients in the equations for Ψ^i and Ψ^e (Eqs. 2.30, 2.31) are determined.

Combining all the above together, the dispersion relation (for external magnetic field in the plane of the sample) is given by:

$$(1+\kappa)^2\left(-\frac{1+\kappa\left(k_y/k_z^e\right)^2}{1+\kappa}\right) + \nu^2\left(k_y/k_z^e\right)^2 - 1 - 2(1+\kappa)\sqrt{-\frac{1+\kappa\left(k_y/k_z^e\right)^2}{1+\kappa}}\cot(k_z^i d) \tag{2.33}$$

(2.34)

Thus far, it has been assumed (DE theory) that only the k_z values were limited by a sample dimension (thickness). The values for k_x and k_y can be approximated by utilizing the physical limits imposed the lateral dimensions of the sample [25] [29]. For a sample of width w and length L, the wavenumbers are

$$k_x = \frac{n_x \pi}{w}, \quad k_y = \frac{n_y \pi}{L}, \tag{2.35}$$

where n_x and n_y are assumed to be positive integers characterizing the modes. The approximate magnitude of the magnetization m_z corresponding to the volume modes $n_x = 1, 2, 3, \ldots$ are shown in Figure 4.5. For future reference, the typical scanning position of a FMRFM probe magnet where the maximum signal intensity is expected is also shown.

The dispersion equation (Eq. 2.33) can be calculated numerically [29]. However, some simple relations can be determined for certain cases [17]. These relations provide consistency checks for FMRFM spectra.

- Observed modes when the magnetic field is parallel to the sample plane: Each resonance mode has a wavevector $\vec{k}$ associated with a spatial variation of the RF component of the magnetization normal to the equilibrium position (i.e., magnetostatic

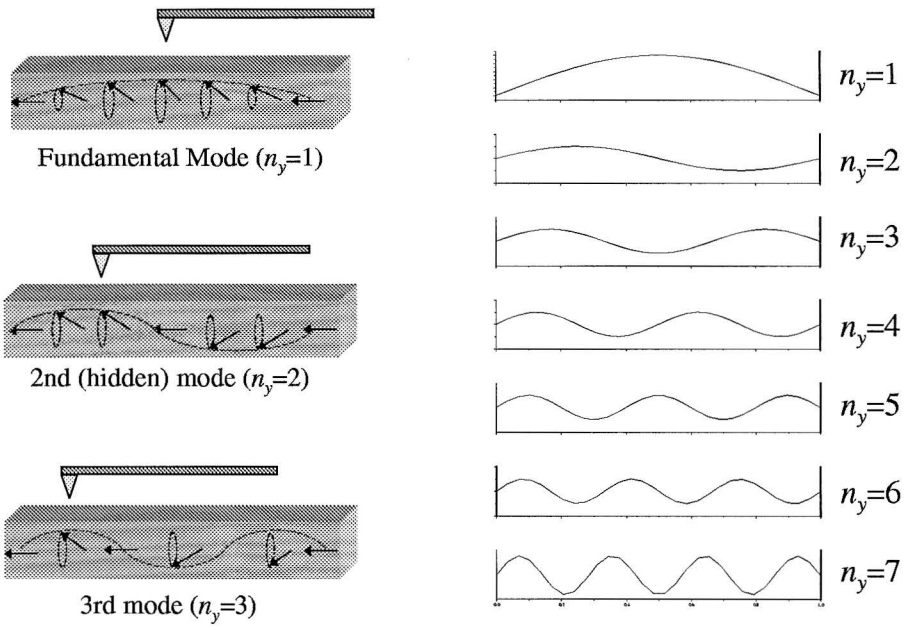

Figure 2.6: The approximate spatial variation of the transverse magnetic moment (m_z) of the first few magnetostatic modes ($n_y = 1, 2, 3, ...$). The cantilever is positoned over the sample where a maximum in the FMRFM signal is expected.

modes). For an in-plane wavevector (k_x, k_y), Eq. 2.32 determines the out-of-plane wavenumber k_z. For a real k_z value ($k_z > 0$), the mode is excited throughout the bulk of the sample (volume mode). This results from the form of the magnetization assumed in the previous derivations, $m = \nabla\Psi^i \propto \nabla(e^{ik_y y}.....)$. For an imaginary k value ($k_y < 0$), the RF component of the magnetization moment decays exponentially from the surface (surface mode). In the FMR spectra, the volume modes occur at external magnetic fields lower than the fundamental mode, and the surface modes occur at fields higher than the fundamental mode.

- Observed modes when the magnetic field is perpendicular to the sample plane: A similar derivation for the field perpendicular to the sample plane yields the results that only volume modes exist. In the FMR spectra, these modes occur at fields lower than the fundamental mode. The field spacings between the volume modes for both

regimes (magnetic field parallel and perpendicular to the sample plane) should be of comparable magnitudes.

- Field spacing between modes: For the fundamental mode ($k_z = 0$) with the field perpendicular to the sample plane, a uniaxial anisotropy energy simply shifts the frequency of the magnetostatic modes by $\Delta\omega = \gamma H_u$. However, the relative positions of the mode spectra (i.e., the field spacing between higher order modes) remain the same. In the FMR spectra, a constant offset of the resonance fields from the calculated values could be attributed to anisotropy energies.

Dispersion relation for microstructures (fundamental mode)

The YIG samples used in this study have geometries where the thickness and lateral dimensions are comparable. Therefore, they can no longer be regarded simply as thin films, but similar to ellipsoids. An approximate dispersion relation for the fundamental mode of microstructures will be derived by (a) assuming a dispersion relation similar to that of ellipsoids and (b) calculating the internal fields ($\vec{H}_i = \vec{H} - \vec{H}_d$) of the rectangular samples.

The demagnetization field is $H_d = -\vec{M} \cdot \hat{n}$, where $\hat{n}$ is the surface normal. For an arbitrary shaped sample, the demagnetization field for a given direction of $\vec{M}$ relative to the sample axes may be approximated $H_d = NM$, where N is the demagnetization factor. In general, N is a tensor function of the sample shape. However, for an ellipsoid, N is a diagonal tensor because the internal field turns out to be uniform. The dispersion relation for the fundamental mode in an ellipsoid, with the external field in the z direction, can be solved explicitly [14]:

$$\left(\frac{\omega}{\gamma}\right)^2 = \left[H - 4\pi\left(N_z - N_x\right)M\right] \times \left[H - 4\pi\left(N_z - N_y\right)M\right] \tag{2.36}$$

where N_i are the demagnetization factors associated with the aspect ratios of an ellipsoid. For comparison, an infinite thin film has $N_x = N_y = 0$, $N_z = 1$, and the dispersion relation reduces to the form $\frac{\omega}{\gamma} = H - H_{d,z} = H - 4\pi M_S$.

The samples in this study have lateral dimensions of a few tens of microns and a thickness of a few microns. A demagnetization field resulting from all faces of the sample will have a significant contribution to the internal field regardless of the orientation of the magnetization. For a sample having magnetization oriented normal to one of the faces ($\hat{z}$), the torque acting on the spins at the center of the sample will give the following approximate dispersion relation

$$\left(\frac{\omega}{\gamma}\right)^2 = [H - (H_{d,z} - H_{d,x})] \times [H - (H_{d,z} - H_{d,y})] \tag{2.37}$$

The ratio of the dimensions will have several effects on the dispersion relation. First, the internal field will have contributions from the demagnetization factors stemming from the lateral dimensions, in addition to the thickness dimension, of the sample. As a result, the external field at resonance will be decreased from the value of $\frac{\omega}{\gamma} = H - 4\pi M_S$ that is typical for very thin films ($t << l, w$). Second, for samples having finite dimensions, the transverse RF component of the magnetization ($m(r,t)$) will establish an internal RF demagnetization field, h_d. The field, h_d, will further influence the resonance condition in a manner similar to presence of $N_{x,y}$ in Eq. 2.36. Third, the demagnetization factors N_i are not constant for any sample that is not an ellipsoid. Thus, the internal field is not exactly uniform throughout the magnetized sample.

In order to approximate the magnitude of the $\vec{H}_d$, the model will assume that the magnetization is uniform across the sample. The demagnetization field is evaluated at the center of the sample and is determined for a sample completely saturated along each of the principle axes of the sample. At the center of the sample, H_d is a minimum and therefore defines the bottom of a "potential well" which establishes the position of the eigenvalue of the fundamental mode. The details of the demagnetization field calculation are in Appendix D. The calculated values are listed in tables included in Chapter 4.

The approximate dispersion relation for the fundamental mode (Eq. 2.37) neglects the variation in the internal field due to h_d, the demagnetization field established by the transverse component of the RF magnetization. Also neglected is the shift of the fundamental mode due to the dipolar forces associated with the finite transverse wavelengths of the fun-

damental mode of the samples. i.e., the fundamental mode was assumed to be $\vec{k} = (0, 0, 0)$, but in reality it is $\vec{k} = (k_x > 0, k_y > 0, k_z > 0)$. This means that all spins are not precessing at the same amplitude in the fundamental mode, but have a complicated amplitude dependence across the sample. An approximate sinusoidal amplitude dependence across the sample is shown in Figure 2.6.

Dispersion relation in microstructures (higher order modes)

An approximate dispersion relation for the higher order magnetostatic modes of microstructures will be determined by utilizing the Kalinikos approximation [32]. This simple model is for the special case where the wave number in the thickness direction is equal to zero, but wave numbers in the film plane are not ($k_z = 0$, $k_x \neq 0$, $k_y \neq 0$).

Damon and Esbach [24] first derived the dispersion relation for traveling magneto-static waves in a magnetic thin film [24]. Kalinikos [32] derived a useful approximation to the dispersion relation that gives the solution explicitly for the mode frequency as a function of the wave number, k. This approximation assumes $k_z = 0$ for all modes, but is still a close approximation to values obtained from DE theory. Kalinikos uses first order perturbation theory, with $k_z = 0$ as the zero-order solution, to obtain the approximate dispersion relation

$$\omega^2 = \omega_i \left[\omega_i + \omega_M \left(1 - \frac{1 - \exp\left(-k_t\ d\right)}{k_t\ d} \right) \right], \tag{2.38}$$

where $\omega_i = \gamma H_i$, $\omega_M = \gamma M_S$, $H_i = H - H_d$, and d is the thickness of the sample. H_i is the internal field required to support the magnetostatic wave of the transverse wave number k_t. H_d is the demagnetization field at the center of the film when the magnetization is saturated normal to the plane of the film.

While this dispersion relation has been established for an infinite media, it will be applied here to approximate the dispersion relations for values of k_t that correspond to the allowed modes (n_x, n_y) of a microscopic structure. The transverse wavenumber is approximated by utilizing the physical limits imposed by the lateral dimensions of the sample [25] [29]. For a sample of width w and length L, the transverse wavenumber is

$$k_t = \left(k_x^2 + k_y^2\right)^{1/2} = \left(\frac{n_x^2\pi^2}{w^2} + \frac{n_y^2\pi^2}{L^2}\right), \tag{2.39}$$

where n_x and n_y are the number of half wavelengths in the x (width) and the y (length) direction of the sample. The modes are not purely sinusoidal, but have a complicated amplitude dependence across the sample. It is a reasonable assumption which is validated by the data in Chapter 4. An approximate sinusoidal amplitude dependence across the sample is shown in Figure 2.6 for several higher order modes.

The field spacing between the magnetostatic modes determined by Eqns. 2.38 and 4.5 show an explicit dependence on the dimensions of the sample — the smaller the structure, the larger the separation between higher order modes.

2.2.3 RF absorption/intensity in uniform field

In typical FMR experiments, the sample is small compared with the dimensions of the RF cavity. Thus, the external RF field, $\vec{H}_{RF}$, can be considered independent of the position $\vec{r}$ within the sample and written as $(H_x, H_y, H_z)e^{-i\omega t}$. For the case where the external field is parallel to the sample plane, the RF component of the magnetic moment is $\vec{m} = \left(0,\, m_y(\vec{r})e^{-i\omega t},\, m_z(\vec{r})e^{-i\omega t}\right)$. From the previous derivations of magnetostatic modes, the magnetic potential inside the sample can be written in the form (Eq. 2.30)

$$\Psi^i\left(x,y,z\right) = X\left(x\right)Y\left(y\right)Z^i\left(z\right) = e^{ik_x x}e^{ik_y y}\left(a\sin(k_z^i z) + b\cos(k_z^i z)\right)e^{-i\omega t} \tag{2.40}$$

for the mode $(k_x, k_y, k_z) = (\frac{n_x\pi}{l_x}, \frac{n_y\pi}{l_y}, k_z^i)$. The intensity of the absorption of the applied RF field can be found by the average value of $\vec{m}\cdot\vec{H}_{RF}$ integrated over the volume of the sample:

$$m \cdot H_{RF} = \frac{1}{2}\,\mathrm{Re}(\vec{m}\cdot\vec{H}_{RF}^{*}), \tag{2.41}$$

where $\vec{H}^*_{RF}$ is the complex conjugate. Substituting for $\vec{m}$ and $\vec{H}^*_{RF}$ and integrating over the volume of the sample, the signal intensity is

$$\langle \vec{m} \cdot \vec{H}_{RF} \rangle = \left\{ \frac{l_y A}{n_y \pi} \left[Z^i(z) \right]_{-d/2}^{d/2} + B \int_{-d/2}^{d/2} Z^i(z)\, dz \right\} \sin\left(\frac{n_y \pi}{2}\right) \frac{l_x}{n_x \pi} \sin\left(\frac{n_x \pi}{2}\right), \quad (2.42)$$

where A and B are functions of ω, H_i, M_S, and $\vec{H}^*_{RF}$.

From this equation (Eq. 2.42) some general conclusions can be drawn. First, there is a selection rule that no absorption will occur for any mode with either n_x or n_y an even integer. Second, if n_x and n_y are both odd integers, then the mode intensity is inversely proportional to n_x (x is the direction of the applied field). Third, the mode intensity decreases with increasing n_y, although not as a simple inverse relation because of the second term in the brackets.

2.3 FMRFM vs. NMR and EPR MRFM

A significant focus of this research is to explore what "spatial resolution" means for FMRFM. In order to do so, the spatial resolution derived for EPR and NMR MRFM is used as a starting point in which to compare the key physical differences arising from the FMRFM. Possible physical effects of the MRFM technique on FMR signals are discussed at the end of this section.

2.3.1 Definitions of spatial resolution in MRFM

Resolution in EPR and NMR MRFM was discussed in the first section of this chapter. The resonance volume is defined, for each axial direction, by

$$\Delta x_i = \frac{\Delta H}{\nabla H_i} = \frac{\Delta H}{\frac{\partial |\vec{H}|}{\partial x_i}}, \quad (2.43)$$

where $i = x, y,$or z. For EPR, the dispersion relation, and thus the resolution, is a *local* effect of the magnetic field. Only the spins within this resonance volume satisfy the resonance condition. A key point is that the resonance volume is determined by the

gradient field of the probe magnet and the line width of the sample. Increasing the gradient field directly increases the resolution.

Resolution in a ferromagnetic sample, however, is complicated by large coupling and the long range dipolar forces within the sample. The ferromagnetic resonance condition no longer depends simply on the local magnetic field as it did for EPR. Ferromagnetic resonance depends directly and critically upon conditions involving the entire sample: the dimensions and anisotropy energies of the sample, and the relative angle of the external field to the sample plane. There are also numerous higher order modes in which the dispersion relation is satisfied. Consequently, the resonance volume is no longer determined simply by the gradient field of the probe magnet and the line width of the sample.

To illustrate these key physical differences between EPR/MRFM and FMRFM, the following three main classes of "spatial resolution" are defined:

1. "Direct" Spatial resolution: This is the typical resolution associated with EPR and NMR MRFM, and defined in Eq. 2.3. The gradient field from the probe magnet alters the local magnetic field within the sample. The gradient field, along with the line width of the sample, creates a small, localized region within the sample where the magnetic field satisfies the dispersion relation. Spins outside of this resonance volume do not satisfy the dispersion relation. Since the spins are not strongly coupled, those spins outside the resonance volume do not significantly affect the spins in resonance. Thus, the probe magnet directly controls the volume of space in which the spins resonate. Only the spins in the localized volume couple to the probe magnet and contribute to the resonance signal.

2. Spatial sensitivity: This is the typical resolution associated with FMRFM. Spatial sensitivity is not determined simply by the gradient field and the line width. For small gradient fields (a few Gauss), the probe magnet does not significantly alter the dispersion relation, as it does for EPR and NMR, but it does still determine a localized region within the sample providing the force upon the mechanical resonator. i.e., the force is determined locally, but not the resonance condition. The strong coupling

between spins in a magnetic sample results in the resonance condition being satisfied by the dispersion relation involving the entire sample instead of the conditions within the localized volume.

For the YIG samples, satisfying the resonance condition of the sample results in magnetostatic modes which have a spatially varying RF component of the magnetization, $\vec{m}(r)$. The probe magnet couples locally to $\vec{m}(r)$, thus measuring the spatial variation in $\vec{m}(r)$ as the cantilever is scanned over the sample. In other words, the spatial variation of the resonance in the sample already exists, and the probe magnet is sensitive to it – the probe magnet does not create the spatial variation. In this regime, resolution is determined by the minimum characteristic length of the mode amplitude variation distinguished by the probe magnet.

An alternate method to understanding spatial sensitivity is to consider the sample as the source of the gradient field. The spatial variation in the sample's magnetization, $\vec{m}(r)$, creates the local gradient field ∇H and the probe magnet acts as the magnetic moment M. The FMRFM signal, produced by the force relation $\vec{F} = \left(\vec{M} \cdot \vec{\nabla}\right) \vec{H}$, is determined integrating the gradient field from the sample over the volume of the probe magnet. Thus, the minimum spatial resolution should be on the order of the dimensions of the probe magnet.

If the gradient field from the probe magnet is increased appreciably, then it may directly affect the dispersion relation. This regime will be discussed at the end of this section and in Chapter 4.

3. Volume sensitivity (or the minimum detectable volume): This resolution is the smallest detectable volume of magnet moment, similar to the minimum detectable number of spins, N_{MDS}, for EPR and NMR. The entire sample fits inside the localized resonance volume which satisfies the resonance condition. i.e., the sample is small enough such that the change in the magnetic field across the entire sample due to the gradient field is less than the line width of the sample: $\frac{\partial H}{\partial z} \cdot L < \Delta H$.

2.3.2 Effects of magnetic coupling within sample

A better understanding of the interaction of a localized magnetic volume and the strong coupling in the sample is needed. This section illustrates the key differences in the dispersion relations, and how a local magnetic field due to the probe magnet could affect the relations.

For EPR and NMR, each spin is not coupled strongly to its neighbors [14] [12]. Therefore, if the resonance condition is satisfied in a small volume of space, only spins within that volume will resonate. When solving the equation of motion, $\frac{d\vec{M}}{dt} = \gamma \vec{M} \times \vec{H}_{eff}$, the RF component of the magnetic moment is *spatially independent* with respect to the sample dimensions. As described earlier, for small oscillations about equilibrium,

$$\begin{aligned} \vec{M} &\rightarrow M_S \hat{z} + \vec{m}\, e^{i\omega t} \\ H_{eff} &\rightarrow H\, \hat{z} + \vec{h}\, e^{i\omega t}, \end{aligned} \tag{2.44}$$

where H is the external magnetic field in the z direction; m is the RF component of the magnetization in the x-y plane and is constant; M_S is the saturation magnetization of the sample (polarized in the z direction); and $\vec{h}$ is the transverse RF component of the field and equal to the applied RF field in this case. Both $\vec{m}$ and $\vec{h}$ are constants, independent of location within the sample. The equation of motion simplifies to the following set of coupled differential equations [14]:

$$\begin{aligned} \frac{dM_x}{dt} &= \gamma H M_y \qquad & \frac{dM_y}{dt} &= \gamma H M_x \\ M_x &= m\cos\omega t \qquad & M_y &= -m\sin\omega t \end{aligned} \tag{2.45}$$

The solution, $\omega = \gamma H$, depends only on the external magnetic field H at the location of the spins. A perturbation in the external field over a small volume, such as from the probe magnet, is easily inserted into the coupled differential equations. Adding $H + \delta H$, where δH is from the probe magnet, into the above equations results in a simple field shift in the dispersion relation: $\omega = \gamma\,(H + \delta H)$.

However, in FMR, the long range coupling results in the magnetic moments strongly interacting over the entire sample [24][17]. The dispersion relation is dominated by the sample dimensions and the external field over the extended sample. A perturbation in the magnetic field over a small volume must be solved within the context of the entire sample.

When solving the equation of motion, $\frac{d\vec{M}}{dt} = \gamma \vec{M} \times \vec{H}_{eff}$, the spatial dependence of the effective field results in an RF component of the magnetic moment that is *spatially dependent* upon the sample dimensions. As described earlier, for small oscillations about equilibrium (Eq. 2.8),

$$\begin{aligned} M &\rightarrow M_S \hat{z} + \vec{m}(r)\, e^{i\omega t} \\ H_{eff} &\rightarrow \vec{H} - \vec{H}_u(r) + \vec{H}_d(r) + \vec{H}_{ex}(r) + \vec{h}(r) e^{i\omega t}, \end{aligned} \tag{2.46}$$

where $\vec{H}_u$, $\vec{H}_d$, and $\vec{H}_{ex}$ are the anisotropy, demagnetization, and exchange fields. The RF component of the magnetization, $\vec{m}(r)$, is no longer a constant but varies spatially. Furthermore, the effective magnetic field H_{eff} now has contributions from the entire sample (rather than individual spins). Thus, the equation of motion for FMR is much more complicated than for EPR, even in the simplest case of magnetostatic modes (Eq. 2.27):

$$\frac{d\vec{M}}{dt} = \gamma \vec{M} \times \left(\vec{H} - 4\pi \bar{N} \cdot \vec{M} + \vec{h}\, e^{i\omega t} \right). \tag{2.47}$$

Furthermore, the dispersion relation for FMR is spatially varying. This is easily seen in the approximation for microstructure (Eqs. 2.38, 4.5):

$$\omega^2 = \omega_i \left[\omega_i + \omega_M \left(1 - \frac{1 - \exp\left(-k_t\, d\right)}{k_t\, d} \right) \right], \tag{2.48}$$

$$k_t = \left(k_x^2 + k_y^2 \right)^{1/2} = \left(\frac{n_x^2 \pi^2}{w^2} + \frac{n_y^2 \pi^2}{L^2} \right). \tag{2.49}$$

As demonstrated by the equations above, the interaction of the spatially dependent magnetic moment $\vec{m}(r)$, the external field H, and the internal fields ($\vec{H}_u$, $\vec{H}_d$, and $\vec{H}_{ex}$) are non-trivial. Adding a small magnetic field perturbation, $H + \delta H$, into the dispersion relation no longer

results in a simple shift of the resonance field. Some possible effects of the perturbation are described below.

2.3.3 Effects on the dispersion relation

The close proximity of the probe magnet to the sample adds a small perturbation field to the external field, $H + \delta H$. Adding δH to a small volume of the sample may slightly modify the dispersion relation locally, but it will not shift the resonance condition uniformly over the sample. However, it may perturb the "shape" of the various normal modes. Some possibilities due to a local perturbation field δH from the probe magnet are explored below.

1. A shift in the resonance field H_{res}: In typical MRFM, the small local field δH simply shifts where the resonance occurs in the external field H: $H_{res} = H + \delta H$. From the approximation of the magnetostatic modes of microstructures, the dispersion relation is (Eq. 2.37)

$$\left(\frac{\omega}{\gamma}\right)^2 = [H - (H_{d,z} - H_{d,x})] \times [H - (H_{d,z} - H_{d,y})]\,. \tag{2.50}$$

   Assuming the internal fields were not perturbed, one may expect a similar shift in FMR measurements by simply adding the small local field into the above equation: $H \rightarrow H + \delta H$. There are two problems with this possibility. First, the shift in the field from the probe magnet is a localized effect, while the entire sample determines the dispersion relation. If the resonance frequency were to be shifted by the field from the probe magnet, it should require that the whole sample fall within the influence of the probe magnet field. i.e., a sample smaller than the resonance volume. Second, creating a small shift in the field over a small fraction of the sample would have to overcome the demagnetization effect, $4\pi \bar{N} \cdot \vec{M}$. A strong local field from the probe magnet, typically $60\,G$ at a scan height of $3\mu m$, is much less than the demagnetization factor of $1750\,G$. The shift would approximately by the weighted average of $H(r)$ over the sample, and thus should have a negligible effect.

2. Change in field spacings between modes: The static magnetic moment of the sample has been assumed to be a constant in our derivations: $M(z) = M_S$. However, the

field from the probe magnet could locally alter the orientation of the static magnetic moment region to region in the sample. This will have effects on the internal magnetic fields of the sample. Effects due to variations in the internal magnetization, such as a slight decrease near the surface of the sample, have been explored in FMR theory in the volume inhomogeneity model [31][33][34]. An example of the effect resulting from a non-constant internal field, $4\pi M(z)$, has been done by Portis [34] for spin waves across the thickness of thin films. In that study, a parabolic form of $4\pi M(z)$ across the sample thickness was assumed, rather than a constant: $4\pi M(z) \rightarrow 4\pi M_S \left(1 - \frac{4\sigma z^2}{t^2}\right)$. They predicted, and measured, a linear spacing of the modes rather than the quadratic spacing predicted by spinwave theory. Thus, a possible effect of the local field from the probe magnet could be an increase or decrease in the field spacings between modes.

In this study, neither a simple shift of the resonance fields nor a change in field spacings between modes were observed beyond the experimental uncertainties of the data. However, in the high gradient field regime ($\delta H \tilde{} 60G$) two effects on the dispersion relation were observed. First, a hidden mode was observed as the probe magnet was scanned along the length of a sample. Second, the signal intensities of the fundamental and particular higher order modes were observed to vary as the probe magnet was brought close to the sample surface. These effects, which we believe may constitute the first demonstration of a controlled localized perturbation of the dispersion relation in FMR, will be discussed in Chapter 4.

3 FMRFM: Experimental set-up

The complexity of ferromagnetic materials creates several experimental challenges beyond typical EPR MRFM. New techniques vital to current and future MRFM studies of both EPR and FMR samples have been developed.

In early EPR/MRFM experiments performed by Rugar, Sidles, and Zhang *et al.* on 2,2-diphenyl-1-picrylhydrazyl (DPPH), the standard test sample for EPR, a parallel force geometry (Fig. 3.2) was used [7], [1], [16]. The external magnetic field, the polarization of the sample, and the direction of the cantilever motion were all along the same axis (z-axis). The sample was mounted on a commercial cantilever with frequency ($f_c \approx 10kHz$), the RF was supplied by a small coil ($800\,Mhz - 1\,GHz$), the gradient and external fields were produced by a macroscopic NdFeB magnet, and the external field was swept ± 300 Gauss by an electromagnet. The resonance condition for DPPH is independent of field angle and depends only on absolute magnitude of H at the sample location.

However, for ferromagnetic samples (FMRFM), there were three main experimental hurdles that needed to be surmounted. First, the resonance depends on external field angle relative to the sample. MRFM set-ups at that time only allowed for the mechanical resonator to resonate along the same axis as the polarizing field. To perform experiments with the external magnetic field H parallel to the plane of the sample, the force and the mechanical resonator motion would have to be perpendicular to H. To achieve this, we developed the *perpendicular force geometry.*

Second FMR must be performed at much higher RF frequencies than EPR, typically $8 - 35\,GHz$, such that resonance occurs at higher magnetic fields in order to saturate the ferromagentic sample. The external field H must be strong enough to saturate the sample to avoid large non-resonance signals [3]. Also, a large H is required to completely polarize the probe magnet and thus maximize the gradient fields. A unique $8GHz$ side-coupled

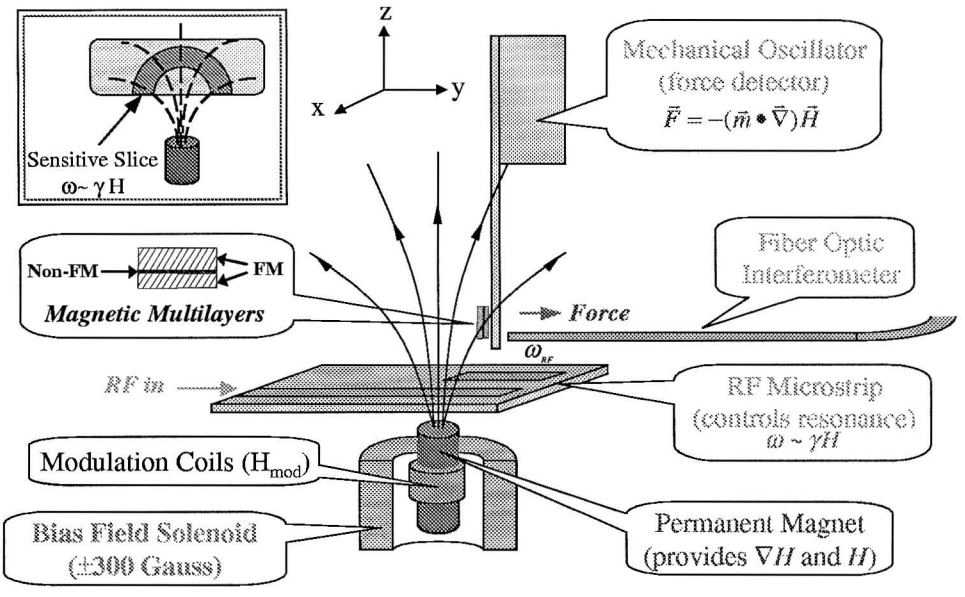

Figure 3.1: *Perpendicular force geometry.* The sample is affixed to the cantilever. The external magnetic field H is parallel to the plane of the sample. The force and the motion of the cantilever are perpendicular to H.

microstrip resonator was designed and produced to meet these requirements.

Third, a true scanning instrument requires that the probe magnet producing the gradient field must be mounted on the cantilever. Also, higher gradient fields are required to increase resolution. We developed new methods for fabricating NiFe-tipped cantilevers. These probe magnets utilize commercial ultrasharp AFM Si cantilevers. A processing technique was developed to coat the commercial cantilevers with permalloy, sputtered from a $Ni_{19}Fe_{89}$ target, solely in the region of the tip. The pyramid shape and micron dimensions of the Si tips produce large gradient fields. The known geometries allow us to model the field and reproduce tips with similar characteristics.

These three new experimental techniques and other important aspects of the FMRFM experimental set-up are presented in this chapter.

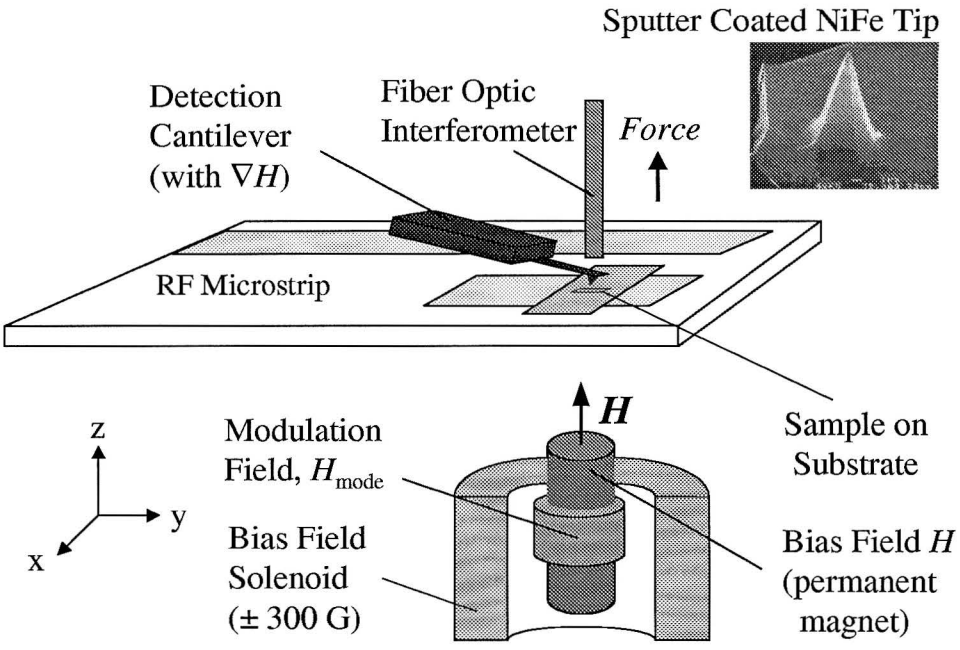

Figure 3.2: *Parallel force geometry.* The external field H is perpendicular to the plane of the sample. The gradient field is produced by the NiFe-tipped cantilever. The force and the motion of the cantilever are parallel to the external field. The spatial characteristics of the sample are scanned by the probe magnet on the cantilever.

3.1 Geometries

Force detection of magnetic resonance requires careful orchestration of the relative orientations of a significant number of experimental variables. These include (a) the direction of the motion of the mechanical resonator, (b) the direction of the induced force (which depends upon the internal magnetization and the gradient field), and (c) the direction of the external field with respect to the sample plane (which determines the internal magnetization). These constraints are satisfied by two classes of experimental configurations, which we term the *perpendicular force geometry* (Fig. 3.3) and the *parallel force geometry* (Fig. 3.2). A small variation on these two principle configurations depends upon whether the sample (Fig. 3.1) or the gradient magnet (Figs. 3.2, 3.3) is affixed to the mechanical resonator.

The basic theory of detection remains the same for each set-up (see Chapter 2, Basic MRFM theory). Each geometry employ the following physical properties:

- A probe magnet produces a gradient field $\nabla\vec{H}$, which couples the magnet to the moment in the sample, to create a force $F = (\vec{M} \cdot \vec{\nabla})\vec{H}$ which acts on the mechanical resonator. This gradient field is produced from either a $\frac{1}{4}$" diameter NdFeB permanent magnet (Fig. 3.1) or a NiFe-tipped cantilever (Figs. 3.2, 3.3).

- The resulting force is exerted onto the cantilever, causing it to deflect. Either the gradient magnet or the sample is placed on the cantilever to detect the strength of the coupling via deflection.

- The magnitude of the sample's magnetic moment in the direction of the cantilever deflection ($M_z$or M_x) is modulated at the resonance frequency of the cantilever, f_c. Thus, the modulated force drives the cantilever and its response is mechanically enhanced by the Q of the cantilever. Modulation is achieved using the anharmonic modulation technique, which is described in a later section [5].

- The amplitude of the cantilever oscillations, usually only a few Å in magnitude, is measured with a fiber optic interferometer and a lock-in amplifier (at f_c).

- The RF field H_{RF} is supplied by a microstrip resonator, orientated such that the RF field is perpendicular to the external field H. Its amplitude, typically $1-3\,Gauss$, is 100% modulated at frequencies of $20-30kHz$.

- The external field H is supplied by a combination of a $\frac{1}{4}$" diameter NdFeB permanent magnet and copper coils. The coils can be swept $\pm 300\,Gauss$. In the very latest set of experiments, a Lakeshore water-cooled electromagnet was used to create and sweep the external field.

- The external field H is modulated by a few gauss (H_{mod}) by a small coil wrapped around the $\frac{1}{4}$" diameter NdFeB permanent magnet. The small field H_{mod} typically has a frequency $f_{H\,\mathrm{mod}}$ of $13kHz$ and an amplitude of a few Gauss.

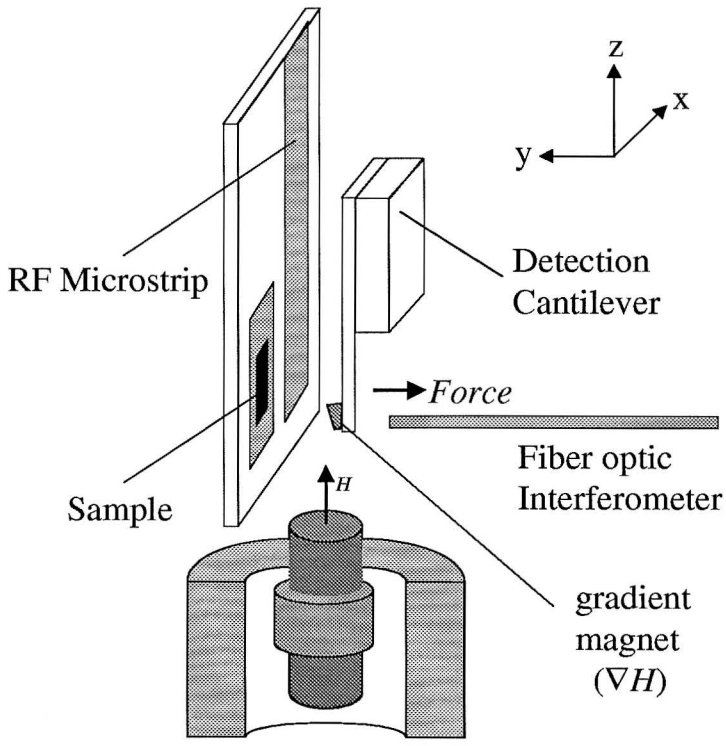

Figure 3.3: *Perpendicular force geometry.* The external field H is parallel to the plane of the sample. The gradient field is produced by the NdFeB probe magnet on the cantilever. The force and motion of the cantilever are perpendicular to the external field. The spatial characteristics of the sample are scanned by the probe magnet on the cantilever.

3.2 Perpendicular force geometry

The resonance condition of DPPH is independent of the angle of the external magnetic field relative to the sample. Typical EPR MRFM measurements were performed with the external magnetic field, the gradient magnetic field, and the force (and thus the cantilever motion) all along the same axis to maximize the signal. However, the resonance conditions for ferromagnetic samples depend critically upon the angle of the external field relative to the sample plane. For Co films, the resonance condition is satisfied at a few hundred Gauss when the magnetic field is parallel to the film plane, but $7 - 12kG$, and beyond the range of our apparatus, when the magnetic field is perpendicular to the film plane. Hence, a geometry that orients the external magnetic field parallel to the plane of a magnetic film is

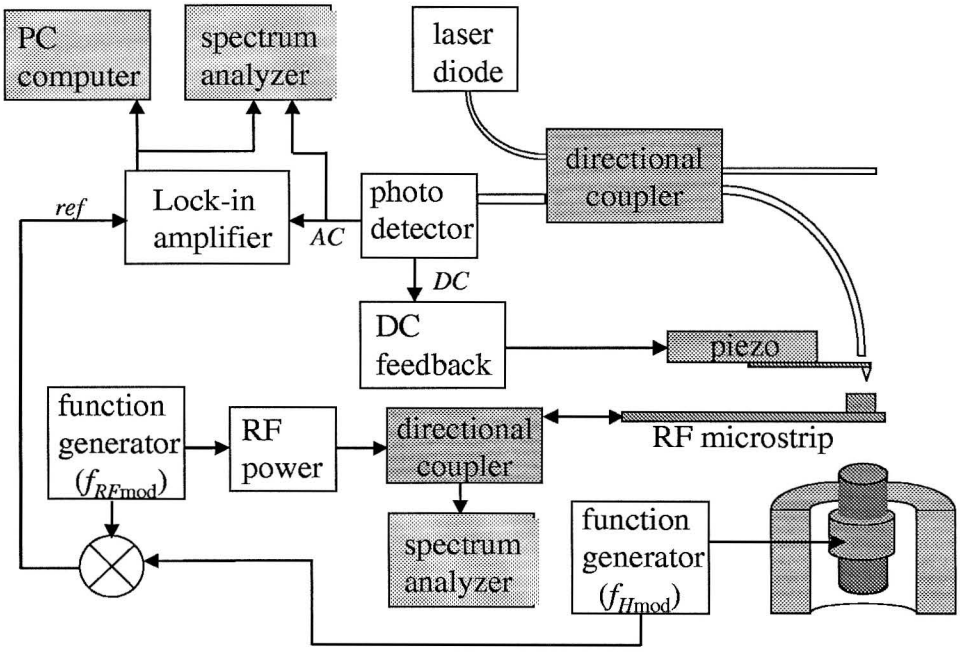

Figure 3.4: Block schematic of the FMRFM set-up. The signal output goes to a PC computer for analysis. The spectrum analyzers monitor the output signal and modulations signals in-situ. See text for details.

required. This places special constraints on the direction of the gradient field inducing the force.

Orienting the external magnetic field parallel to the sample requires the motion of the mechanical resonator to be perpendicular to the external field (see Fig. 3.1 and 3.3). Thus, the force induced by a gradient field must be in the y direction. We term this orientation of the external fields and cantilever motion the *perpendicular force geometry.*

Sample on cantilever

For the case of Co films deposited onto cantilevers, a macroscopic NdFeB bar magnet polarized in the z direction was used to produce the gradient field (Chapter 5). To induce a force in the y direction, the sample-bearing cantilever must be placed off-axis from the z axis of the bar magnet. The long axis of the cantilever is parallel to the z axis, thus only

cantilever motion along the y direction is considered (see Figs. 3.1, 3.5). Forces induced in the z and x directions are negligible because the force constants of the cantilever along those directions are much larger than the force constant in the y direction.

The force induced by the gradient field is

$$F_y = \left[\vec{\nabla}\left(\vec{m}\cdot\vec{H}\right)\right]_y = m_x\frac{\partial H_x}{\partial y} + m_y\frac{\partial H_y}{\partial y} + m_z\frac{\partial H_z}{\partial y}. \tag{3.1}$$

Or, using the product rule $\left(\vec{m}\cdot\vec{\nabla}\right)\vec{H} + \vec{m}\times\left(\vec{\nabla}\times\vec{H}\right) + \vec{H}\times\left(\vec{\nabla}\times\vec{m}\right) + \left(\vec{H}\cdot\vec{\nabla}\right)\vec{m}$, an alternate but equivalent expression is

$$F_y = \left[\left(\vec{m}\cdot\vec{\nabla}\right)\vec{H}\right]_y = m_x\frac{\partial H_y}{\partial x} + m_y\frac{\partial H_y}{\partial y} + m_z\frac{\partial H_y}{\partial z}, \tag{3.2}$$

where it has been assumed that there are no currents ($\vec{\nabla}\times\vec{H} = 0$) and that the magnetic moments cannot act upon themselves.

The sample has magnetization in all three direction ($\vec{m} = m_x, m_y, m_z$) when it is placed off-axis from the bar magnet. When the sample-bearing cantilever is placed at a significant angle from the z axis of the NdFeB bar magnet in the y-z plane, as shown in Figure 3.5, the gradient field along the x direction is negligible. Thus, the force induced on the sample-bearing cantilever in the y direction can be approximated as

$$F_y = m_y\frac{\partial H_y}{\partial y} + m_z\frac{\partial H_y}{\partial z}. \tag{3.3}$$

The resonance condition for the Co films will occur at higher fields for larger angles of the external field relative to the film plane. However, the resonance fields remain within the range of our FMRFM apparatus for angles less than $60 - 70°$.

Probe magnet on cantilever

For FMRFM measurements upon the YIG films, the gradient field was produced by either a NiFe-tipped cantilever (described in section "NiFe-tipped cantilevers"), or a small particle of NdFeB mounted upon a commercial cantilever and pre-polarized in a $8T$ field (Figs. 3.2, 3.3). The probe magnet on the cantilever produces the gradient field which induces the

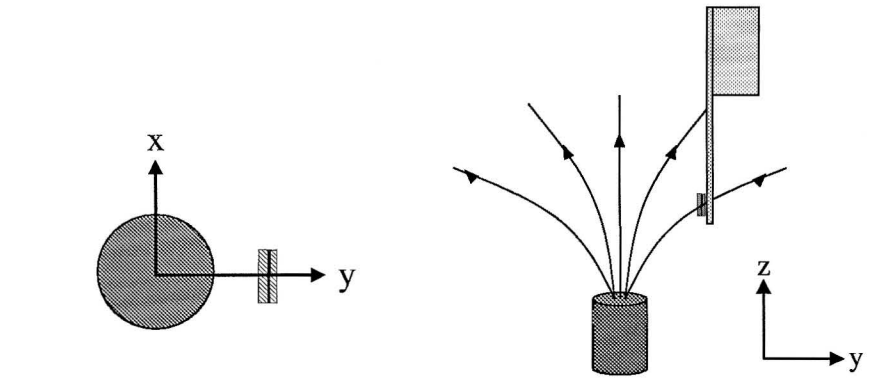

Figure 3.5: The position of the Co layer sample-bearing cantilevers (Chapter 5). The magnetization is negligible in the x direction ($m_x \approx 0$).

force on the cantilever. Therefore, the external field can be oriented completely parallel to the YIG plane — not off-axis as was required for the sample on cantilever — and the magnetization is along the z axis ($\vec{m} = 0, 0, m_z$). The cantilever is still oriented such that deflection only occurs in the y direction. Thus, the resultant force is simply

$$F_y = m_z \frac{\partial H_y}{\partial z}. \tag{3.4}$$

3.3 Anharmonic modulation

In general, it has proven very difficult to modulate the small field H_{mod}, or the RF amplitude H_{RF}, directly at the fundamental resonance frequency of the cantilever, f_c. With the gradient magnet on the mechanical resonator, modulation of the external magnetic field at f_c induces a direct force on the resonator. i.e., it creates a large background signal. To avoid such coupling, we have used the anharmonic modulation technique first demonstrated by Bruland *et al.* [5].

For the case studied by Bruland *et al.* namely EPR on DPPH, the steady state magne-

tization has been derived by Garstens [35] and is given by

$$M_z = \left(\frac{\chi_0}{\mu_0}\right)\left[H_z - \frac{\gamma^2\omega^2 H_{RF}^2 H_z \tau^4}{\left[1+(\gamma H_z-\omega)^2\tau^2\right]\left[1+(\gamma H_z+\omega)^2\tau^2\right] + \frac{1}{2}\gamma^2 H_{RF}^2\tau^2\left(1+\omega^2\tau^2+\gamma^2 H_z^2\tau^2\right)}\right] \tag{3.5}$$

where χ_0 is the parametric susceptibility, H_{RF} is the strength of the RF field, H_z is the strength of the polarizing external field, ω is the frequency of H_{RF}, τ is the relaxation time, and μ_0 is the permeability of vacuum. M_z is a linear function except in the region of resonance. When the resonance condition is satisfied (i.e., $H_z = \pm\omega/\gamma$ for DPPH), the magnetization along the z axis is sharply suppressed as the system becomes saturated. From Eq. 3.5, it is evident that there are three ways to create the oscillating M_z required to produce a time-varying force on the mechanical resonator: (a) modulation of the amplitude of H_z, (b) modulation of the amplitude of H_{RF}, or (c) modulation of the RF frequency ω. Anharmonic modulation is based upon simultaneous modulation of *both* the amplitude of H_z and the amplitude of H_{RF}, at frequencies $f_{H\,\mathrm{mod}}$ and $f_{RF\,\mathrm{mod}}$ respectively. The frequencies are chosen such that $|f_{RF\,\mathrm{mod}} - f_{H\,\mathrm{mod}}| = f_c$, and that neither $f_{RF\,\mathrm{mod}}$ nor $f_{H\,\mathrm{mod}}$ are equal to f_c. This minimizes direct coupling to the mechanical resonator. The utilization of a lock-in amplifier at f_c further suppresses contributions to the detected mechanical response created by the field modulation. Beats in the time-varying magnetization force are shown in Figure 3.6. The precise beat waveform will depend in detail upon the dispersion relation. Eq. 3.5 is only one possible case, given for the example of EPR in DPPH.

The disadvantage of anharmonic modulation is that the nonlinear dependence upon the modulation fields translates "signal" to a wide range of harmonic products, $|nf_{H\,\mathrm{mod}} \pm mf_{RF\,\mathrm{mod}}|$, where n, m are integers. Only a fraction of the signal power will be converted to the desired product $f_c = |f_{RF\,\mathrm{mod}} - f_{H\,\mathrm{mod}}|$.

The anharmonic modulation effect can be thought of in the following simple terms. The modulation field H_{mod} has the effect of modulating the external field in and out of resonance. The modulation of the amplitude of the RF field has the effect of turning the

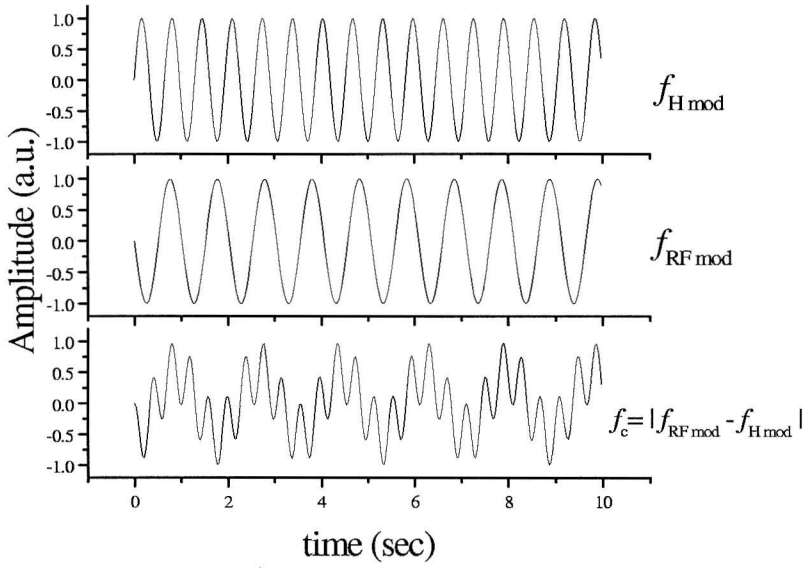

Figure 3.6: A pictorial representation of the anharmonic modulation technique, two field modulations are used to modulate the magnetic resonance at different frequencies, f_{mod} and f_{RF}. The interaction of these two oscillations produces a response that modulates the resonance signal at the difference frequency $|f_{RF} - f_{\mathrm{mod}}| = f_c$. The actual dependencies are more complicated than a simple product function.

resonance of the sample off and on. Their combined effect is to modulate the magnetic moment M_z producing the force on the mechanical resonator, $F_z = M_z \cdot \nabla H_z$.

The characteristic times, T_1 and T_2, for our samples to reach equilibrium are much faster than the frequencies at which the magnetic fields are modulated or at which the signals are detected. Thus, the effect of turning the resonance off and on is, for these purposes, adiabatic.

In this set-up, the frequency is typically at $f_{H\,\mathrm{mod}}$ $(H_{\mathrm{mod}}) = 13\,kHz$, which is within the bandwidth of the power amplifier, to drive the field modulation coil [36]. The RF amplitude was modulated at higher frequency, typically $\sim 31kHz$, chosen such that the difference $|f_{RF\,\mathrm{mod}} - f_{H\,\mathrm{mod}}|$ matched the cantilever frequency. Typically, $f_{H\,\mathrm{mod}} < f_c < f_{RF\,\mathrm{mod}}$ for the NiFe-tipped cantilevers ($f_c \approx 18\,kHz$), and $f_c < f_{H\,\mathrm{mod}} < f_{RF\,\mathrm{mod}}$ for the NdFeB-

tipped cantilevers and for the sample-bearing cantilevers ($f_c \approx 3 - 10\,kHz$). Operation with both modulation frequencies below the cantilever frequency, $f_{H\,\mathrm{mod}} < f_{RF\,\mathrm{mod}} < f_c$, has also been used. However, operation at low frequencies are subject to environmental noises at audio frequencies, and is avoided if possible.

3.4 Microstrip resonators

This FMRFM work is typically performed at microwave frequencies. At these frequencies, higher external resonance fields permit saturation of the sample. In FMRFM, this has the added benefit of also saturating the NiFe probe magnet in the direction of the external field. For parallel force geometries, saturating the probe magnet maximizes the gradient field produced by the NiFe-tipped cantilevers.

In early experiments on EPR [8] and FMR [3], small RF fields of only a few Gauss were supplied by a small coil and tank circuit. These operated at frequencies from a few hundred MHz to $1GHz$. However, in the early FMR experiments on YIG films, this low frequency created a large non-resonant signal due to the sample not being fully magnetized (see Z. Zhang *et al.* [3]). Tank circuits could not easily provide frequencies above $1GHz$.

To enable experiments at higher frequencies, the microstrip resonator shown in Figure 3.7(b) was employed. These are designed to operate at a frequency of $\approx 8GHz$ and produce a magnetic field of a few Gauss. These resonators have several characteristics that are ideal for FMRFM. The higher RF frequency requires a higher external field H to satisfy the resonance condition, thus ensuring the saturation of the YIG samples, Co films, and the NiFe-tipped cantilevers. The properties of the microstrip substrate were chosen to permit large resonator structures. These produce uniform RF fields over an area large compared to the sample dimensions. The unique design promotes coupling of the feedline with the resonator. These have produced RF magnetic fields of a few Gauss, comparable to the fields produced by coil and tank circuits in earlier measurements.

3.4.1 Substrate, dimensions, and design properties

This microstrip design is a modified microstrip filter, as shown in Figure 3.7. The resonators are produced on Duroid, a commercial copper plated dielectric marketed by the Rogers Corporation [37]. For the Rogers RO4003 material used here, the relative dielectric permittivity ϵ_r is 3.38, the thickness of the dielectric t is $2mm$, and the thickness of the copper is $35\mu m$.

The width w of the microstrip is determined by the desired impedance of the line, Z_0, the dielectric thickness t, and the substrate relative permittivity ϵ_r. The relation between these properties is given approximately for two different cases [38].

For "narrow" strips ($w/t < 3.3$),

$$Z_0 = \frac{119.9}{\sqrt{2(\epsilon_r + 1)}} \left[\ln \left\{ 4\frac{t}{w} + \sqrt{16\left(\frac{t}{w}\right)^2 + 2} \right\} \right]. \tag{3.6}$$

For "wide" strips ($w/t > 3.3$),

$$Z_0 = \frac{119.9\pi}{\sqrt{2\epsilon_r}} \left[\frac{w}{2t} + \frac{\ln 4}{\pi} + \frac{\ln\left(e\pi^2/16\right)}{2\pi} \left(\frac{\epsilon_r - 1}{\epsilon_r^2}\right) + \frac{\epsilon_r + 1}{2\pi\epsilon_r} \left\{ \ln \frac{\pi e}{2} + \ln\left(\frac{w}{2t} + .94\right) \right\} \right]^{-1}. \tag{3.7}$$

For an impedance of $Z_0 = 50\Omega$, a microstrip on the chosen Duroid requires a width of $w = 0.5\,mm$.

The length of the half wavelength resonator depends upon an effective permittivity ϵ_{eff}. A considerable portion of the electromagnetic fringe fields extend beyond the physical ends of the microstrip line and resonator. This can be accounted for by considering the line to be longer electrically, and introducing an effective permittivity ϵ_{eff} that depends upon the physical dimensions of the line. This relation is given by [39]

$$\epsilon_{eff} = \frac{\epsilon_r + 1}{2} + \frac{\epsilon_r - 1}{2} \left[1 + 12\frac{t}{w} \right]^{-1/2}. \tag{3.8}$$

The length l of a half wavelength resonator is found simply by the equation

$$l = \frac{\lambda}{2} = \frac{1}{2}\frac{v_p}{f} = \frac{c}{2f\sqrt{\epsilon_{eff}}}, \tag{3.9}$$

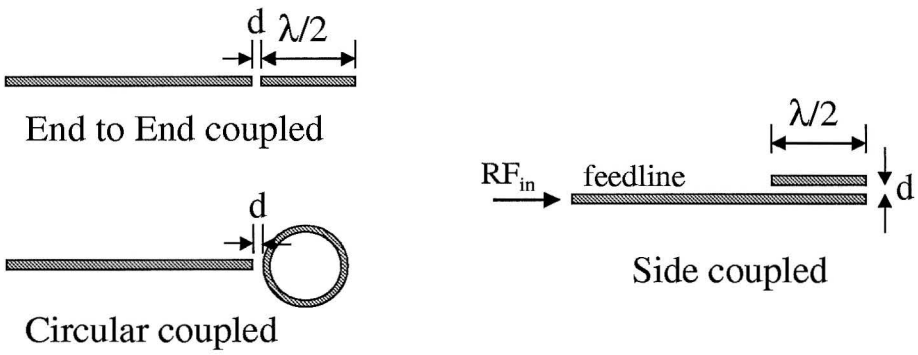

Figure 3.7: Conventional microstrip resonator designs, and the new "side-coupled" design employed in this work.

where v_p is the propagation velocity of a TEM wave, c is the speed of light in a vacuum, and f is the frequency of the resonator. The effective permittivity ϵ_{eff} has been substituted for the regular permittivity of the dielectric substrate. For a $8GHz$ resonator, the length of a half wavelength resonator is $11.5mm$.

The Duroid thickness and dielectric properties were chosen to produce dimensions of the microstrip much larger than common microstrip resonators typically produced on sapphire. Common microstrip resonators, such as the end-to-end or ring-coupled microstrips, are shown in Figure 3.7 [38] [39] [40]. However, for these typical designs produced on the Duroid, their large dimensions ($0.5mm$ wide, $11mm$ long, $8GHz$) resulted in low coupling and inadequate RF magnetic fields. Also, the required spacing d between the feedline and the common resonators for optimal coupling were too small for our microstrip fabrication technics (see Appendix C: Microstrip fabrication techniques).

Computer simulations, using the program *Sonnet,* were used to determine optimal dimensions and spacing for the various microstrip resonators [41]. For this "side-coupled" resonator at $8GHz$, the best parameters are $l = 11.44mm$, $w = .46mm$, and $d = .2mm$. In computer simulations, these dimensions produce a maximum surface current $J_{\max}$ in the center of the resonator of $130\,Amps/m$ for an input into the feedline of $1\,volt = 13dBm = 28mW$. The magnetic field directly above the microstrip (at a distance much less than

its width) can be roughly estimated by the magnetic field above an infinite current sheet, given by the relation

$$H = \frac{1}{2}\mu_B J, \tag{3.10}$$

where J is the surface current and μ_0 is the Bohr magneton. For our resonators, this relation yields a magnetic field of $1Gauss$ for an input power of $28mW$, and a field of $3G$ for an input power of $100mW$. These RF magnetic field strengths are comparable to fields obtained with coils and tank circuits.

The Q for microstrip resonator structures is estimated at ≈ 100 in the literature [39]. Measurements of the side-coupled resonators yielded a $Q \approx 72$, shown in Figure 3.7, which is consistent with theory. The absorption of RF power into the resonator is determined by measuring the reflected RF power from the microstrip structure. A schematic of the measurements is shown in Figure 3.9. The resonator is coupled to semi-rigid coaxial cable (Micro-coax UT85) with a microstrip launcher [42]. A directional coupler passes the RF power from the source into the microstrip structure. Approximately $(-10dB)$ of the reflected power is diverted by the directional coupler to a spectrum analyzer, which measures the amplitude and frequency. During FMRFM measurements, the RF reflected power can be monitored continuously with this method without affecting the FMR.

3.4.2 Impedance matching

The impedance matching of the microstrip resonator to the semirigid coaxial cable is the most significant, and difficult, aspect of the RF system. Without a good impedance match, the resonator does not couple well, and thus the RF field H_{RF} is too small to produce detectable FMR signals. Since the resonator is an open circuit, the impedance Z_0 depends on not only the permittivity ϵ_r and width w of both the resonator and feedline, but also depends on the length of the feedline and the length of the semi-rigid coax cable connecting the RF source to the microstrip. Furthermore, mounting a sample on the microstrip can also alter its impedance.

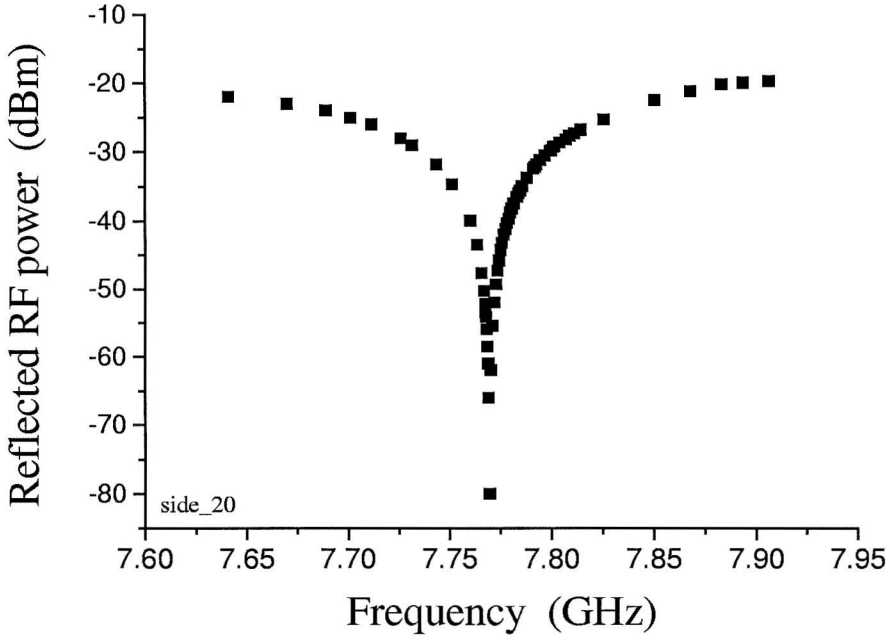

Figure 3.8: Reflected RF power spectrum of a microstrip resonator. The resonantor has a peak absorption at $f_{RF} = 7.77GHz$, and $Q \approx 70$.

Experimental adjustments can be made to modify the impedance. The easiest method is to shorten the feedline at the end connected to the RF launcher. Since the Duroid is thin, this can be achieved simply by cutting the substrate/feedline with regular scissors. Changing the capacitance under the RF launcher/feedline interface can also modify the impedance [43]. A similar effect can be achieved by adding silver paint or tin foil under the microstrip near the RF launcher. Often a combination of these techniques is needed to achieve the best impedance match. A good match will result in a return loss of $20dB$ of the RF power input on resonance.

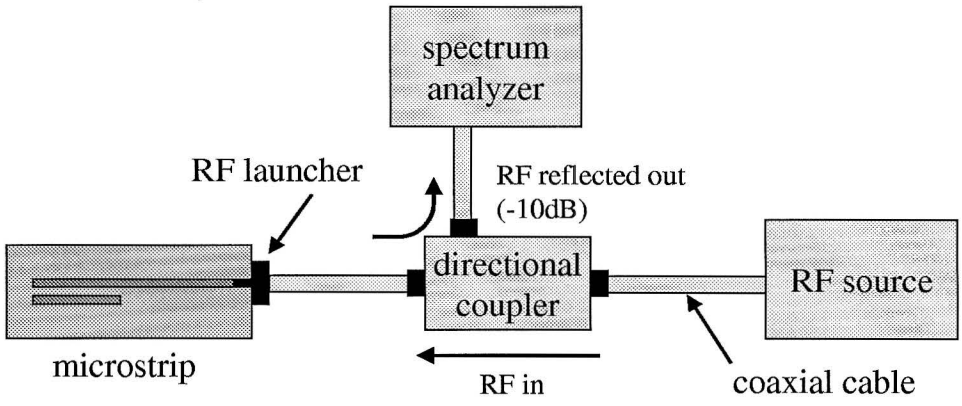

Figure 3.9: Block schematic of the microwave circuit used in the experiment. Power into and reflected from the microstrip resonator is measured.

3.4.3 Experimentally determined properties of our microstrip

UNIFORMITY

The uniformity of the RF field produced by the microstrip resonator was mapped out by observing the FMRFM signal of the R-Rough YIG sample (see Chapter 4 for description of sample). This sample, a small, roughly rectangular particle of YIG, was mounted on a commercial cantilever, and scanned over the surface of the microstrip. In this experimental set-up, the gradient field was supplied by a $\frac{1}{4}$" diameter NdFeB magnet.

In Figure 3.10(a), the YIG bearing cantilever was scanned across the width of both the resonator and the feedline approximately $400\mu m$ above the microstrip surface. The amplitude of the FMRFM signal of the magnetostatic modes are roughly equal between the resonator and the feedline. More importantly, the amplitudes are fairly symmetric and constant over the resonator's width. Thus, a micron scale sample placed approximately $400\mu m$ above the microstrip surface would be in a fairly uniform RF field.

The sample was also scanned over the length of the resonator, as shown in Figure 3.10(b). The FMRFM amplitude is again fairly uniform for the fundamental mode over a $4mm$ length of the resonator. The amplitude is still fairly uniform for the first higher order mode over $1mm$ length of the resonator. Our samples have dimensions typically tens

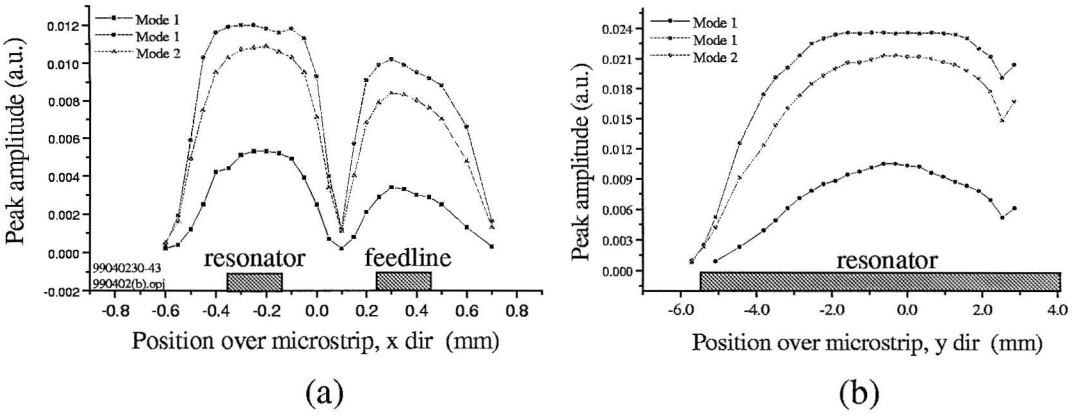

Figure 3.10: FMRFM signal amplitude from a YIG sample on cantilever. (a) Sample is scanned across width of the microstrip and the feedline. (b). Sample is scanned down the length of the microstrip.

of microns. Thus the RF field can be assumed to be fairly uniform over the entire sample.

Signal intensity

The signal intensity can be enhanced by increasing the RF power or by increasing the H_{mod} amplitude. However, increasing the RF power can lead to overdriving the resonance into a non-linear regime. This is discussed in detail in Chapter 4. However, we can determine the optimum operating RF power by measuring FMRFM signal amplitude vs. RF power, as shown in Figure 3.11(a). This spectra was taken with the R-Rough YIG particle mounted on the cantilever, located above the center of the microstrip resonator. When the resonance signal is overdriven, the signal amplitude levels off and eventually decreases due to its nonlinear response.

The signal amplitude also depends upon the distance from the sample to the microstrip resonator surface, and is shown in Figure 3.11(b). The RF substrate, Duroid, was chosen for its low permittivity, $\epsilon_r = 3.3$. The lower permittivity results in a greater fringe field effect, which is desired. However, if the sample is too close to the microstrip surface, the fringe effects from the edges of the microstrip may be weaker. Thus, there is a maximum

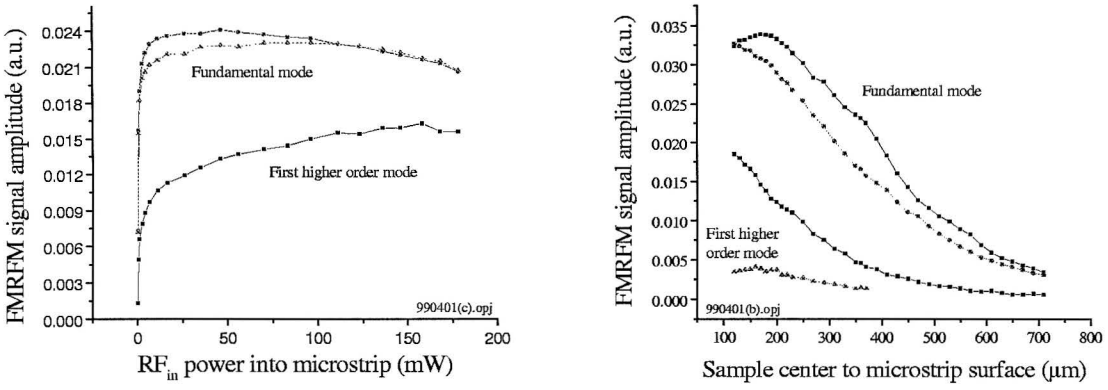

Figure 3.11: (a) FMRFM signal amplitude versus RF power into microstrip resonator. The signal levels off and eventually decreases due to overdriving the resonance. (b) FMRFM signal amplitude versus distance of sample center to microstrip surface. The signal peaks at approximately $200\mu m$ due to fringe effects.

signal amplitude of the fundamental mode at approximately $200\mu m$ above the microstrip surface. The higher order modes do not exhibit this effect due to the shape of the YIG particle. The rectangular end, in which the higher order modes persist, is farthest from the cantilever tip. Thus, the rectangular end is always further from the microstrip surface than the center of the sample, where the fundamental mode is maximum.

Another interesting feature of Figure 3.11(b) is the apparent slight oscillation of the signal amplitude as the sample is moved further away from the microstrip surface. These oscillations occur at approximately $100\mu m$ intervals. They could be due to variations in the RF field. However, near field analysis of RF fields is not available to verify this theory since RF applications are mainly interested in far field effects. No clear explanation for these oscillations has yet been found.

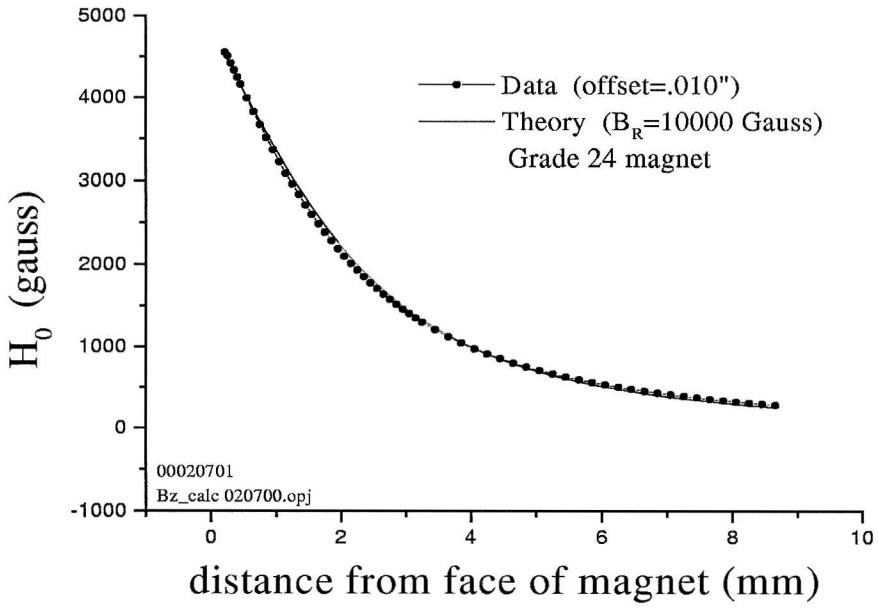

Figure 3.12: Calibration of the magnetic field vs. distance from the surface of the $\frac{1}{4}$" diameter NdFeB magnet.

3.5 "Old" versus "new" FMRFM apparatus

Towards the end of this study, a new FMRFM apparatus was designed and built. Measurements of spectra for the $20\mu m$ series were repeated in the "new" FMRFM set-up to calibrate the absolute $\vec{H}$ fields taken with the "old" FMRFM system.

In the "old" FMRFM set-up, the external magnetic field H was supplied by a small NdFeB permanent magnet with a $\frac{1}{4}$" diameter and a $\frac{1}{2}$" length. A solenoid sweeps the external field by $\pm 300\, Gauss$. The value of H was established by positioning the sample at a predetermined location in front of the face of the NdFeB magnet (Figure 3.12). Sample-to-tip distance could be resolved in $1\mu m$ steps with XYZ translation stages. Both parallel and perpendicular field geometries were available. The stages and magnets were mounted inside a large bell-jar for operation in vacuum, although much of the data was obtained at atmospheric pressure. The majority of the data presented in this study were obtained with this set-up.

In the "new" FMRFM, the external magnetic field H was supplied by a Lakeshore 4" water-cooled magnet, which has 6000 Gauss at a 2" separation between the pole faces. A computer-controlled current source sweep the field of this electromagnet. This apparatus was constructed recently, and its optimization is not yet complete. Currently, sample-to-tip distance can only be resolved in $3 - 5\mu m$ steps, and only perpendicular field geometry is readily available.

The higher fields allow characterization of metallic samples, such as Co, with the field perpendicular to the sample plane. The cantilever, mounted on a 4-quadrant piezo tube, will allow for nanometer control over the separation of the sample surface and probe magnet. The guts of the FMRFM are encased within a rectangular vacuum box mounted on a platform which can rotate $\pm 10°$ with respect to the normal of the magnet face.

3.6 NiFe on tips of ultrasharp cantilevers

Spatial sensitivity in FMRFM is determined by the characteristic size of the probe magnet and the gradient field. Early measurements used a macroscopic NdFeB magnet, $\frac{1}{4}$" in diameter and $\frac{1}{2}$" in length, which produced gradient fields of $\nabla H \approx .1 - 1\, G/\mu m$. Later, small NdFeB particles of dimension $20 - 50\mu m$, attached to commercial cantilevers and prepolarized in 8T fields, were used as probe magnets to produce gradient fields of $\approx 8G/\mu m$. However, these small NdFeB particles had irregular shapes, and the gradient fields were hard to model mathematically. For commercially available magnetically coated cantilevers for magnetic force microscopy (MFM), the whole cantilever, including its tip, is coated with magnetic material. For MFM, only the magnetic material on the tip makes significant contributions to the probe-sample interaction. However, this method of coating presents several problems for FMRFM and MRFM measurement, which require operation in external RF fields and at low temperatures (MRFM only).

- Differential thermal contractions between the native material (Si) of the cantilever and the coating layer of the metallic magnetic material (NiFe) results in stressing and bending of the resonator at low temperatures. By coating solely the tip of the cantilever, the stress causing bending is eliminated.

- Presence of a metallic layer of magnetic material (NiFe) results in parasitic heating of the mechanical resonator in an external RF field (see section Miscellaneous). By reducing the area of metallic material, this heating is greatly reduced.

- The magnetic material on the mechanical resonator results in a significant resonant frequency shift as the external magnetic field is swept. As the field is swept, it creates a steady but varying force on the cantilever, creating a constant frequency shift. By reducing the amount of magnetic material on the cantilever, this effect can be minimized.

Furthermore, resolution depends upon the dimensions and gradient field of the probe magnet. Effective reduction of the size of the probe magnet was achieved by coating NiFe, sputtered from a $Ni_{19}Fe_{81}$ Permalloy target, solely in the region of the tip onto ultrasharp tips of commercial cantilevers [44]. A picture of the tip, before and after coating, is shown in Figure 3.13. These probe magnets have regular shapes (conical or pyramidal tips), and the thickness of the NiFe is determined by sputtering. Thus, the gradient fields can be modeled and reproduced (Fig. 3.14). The processing details are included in Appendix C. It is significant to note that sputter conditions required optimization to produce stress free films. Stress in the films create significant problems in the quality of the probe magnet. Excessive stress in the film can cause the film to wrinkle or to pull away from the Si cantilever surface. Also, when exposed to the RF field, the increased temperature of the film could lead to excessive oxidization of the metal film (see section Miscellaneous: Thermal heating).

3.7 Fiber optic detection

The deflection of the mechanical resonator is detected by a fiber optic interferometer. A schematic of the interferometer is shown in Figure 3.15. The detail shows the path difference light beams travel to create constructive or destructive interference. A DC voltage across the piezo maintains a constant distance d between the fiber end and the cantilever surface using DC feedback.

An approximation of the light intensities for each arm of the interferometer is shown

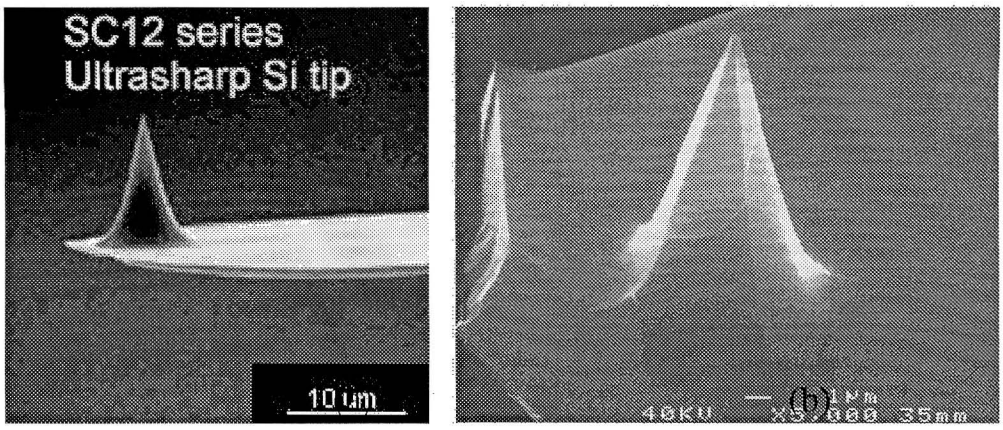

Figure 3.13: The uncoated SC12 series ultrasharp Si cantilever (courtesy of Silicon-MDT Ltd.) and the tip of cantilever after being coated with 1200 Å of NiFe.

in the schematic (Fig. 3.15). The laser diode outputs an intensity I_0 into arm #1. It passes through the 90/10 directional coupler, which directs 90% of the light to arm #2 and 10% of the light to arm #3. The cleaved end of the fiber of arm #3 is situated above the cantilever a distance d, typically $10 - 50\mu m$. The light then reflects off two surfaces separated by a distance d: the glass-air interface of the fiber, and the Si surface of the cantilever. The light, reflected from the Si surface, must couple back into the cleaved end of the fiber. The two reflected light beams recombine in the fiber to produce constructive or destructive interference. The reflected light is measured with a photodetector. The flatness of the surfaces (both the cleaved end of the fiber and the Si cantilever surface) are vital to achieving interference fringes.

Two different laser diode sources were used. The first system used a singlemode $3mW$ laser diode (Mitsubishi model 3411) with a wavelength of $\lambda = 834nm$. It was pigtail connected directly to an isolator and then to a 50/50 directional coupler with a continuous fiber [45]. The second system used a multimode $3mW$ laser diode (Mitsubishi model 40116R-01) with a wavelength of $\lambda = 794nm$. It was pigtail connected to a fiber that is terminated with an FC connector. The FC connector was "PC polished" to minimize reflections. It was then connected to a 90/10 directional coupler with FC connectors [45]. Both systems used 5/80 fiber, which has a core of $5\mu m$ and a cladding of $80\mu m$.

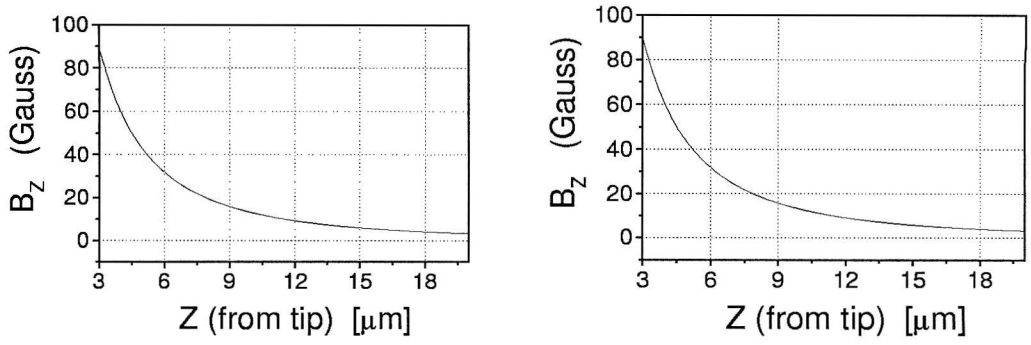

Figure 3.14: Calculated fields and gradients from NiFe coated cantilever tips. At $10\mu m$: $H_z \approx 13\,Gauss$, $\frac{dH_z}{dz} \approx 2.4\,G/\mu m$.

The photodetector, model 1801 from New Focus [46], outputs a voltage signal with both DC and AC components proportional to the light intensity incident onto its photodiode. It has a bandwidth of $125MHz$, a current gain of $40V/mA$, and an input noise current of $< 2pA/\sqrt{Hz}$ at 10MHz. The measured output noise level is typically $2nV/\sqrt{Hz}$ at $10kHz$. The DC signal is directed to a negative feedback circuit to maintain a constant distance between the fiber end and the cantilever surface. The distance is altered by applying a voltage across a piezo to which the cantilever is mounted, shown in Figure 3.15. The AC signal, produced by the oscillations of the cantilever, is directed to the lock-in amplifier and used as the reference frequency to determine FMRFM signals.

3.7.1 Intensity of the interference fringes

As the path difference between the fiber and the cantilever is varied linearly, the intensity due to constructive or destructive interference of the two beams varies sinusoidally. This will produce fringes in the photodetector output voltage as shown in Figure 3.16. The distance the light must travel to and from the cantilever surface is $2d$. Thus, the system obtains constructive interference for $2d = (n+\frac{1}{2})\lambda$ and destructive interference for $2d = n\lambda$, where n is a positive integer.

The visibility of the interference fringes is defined in the following method [47]. The

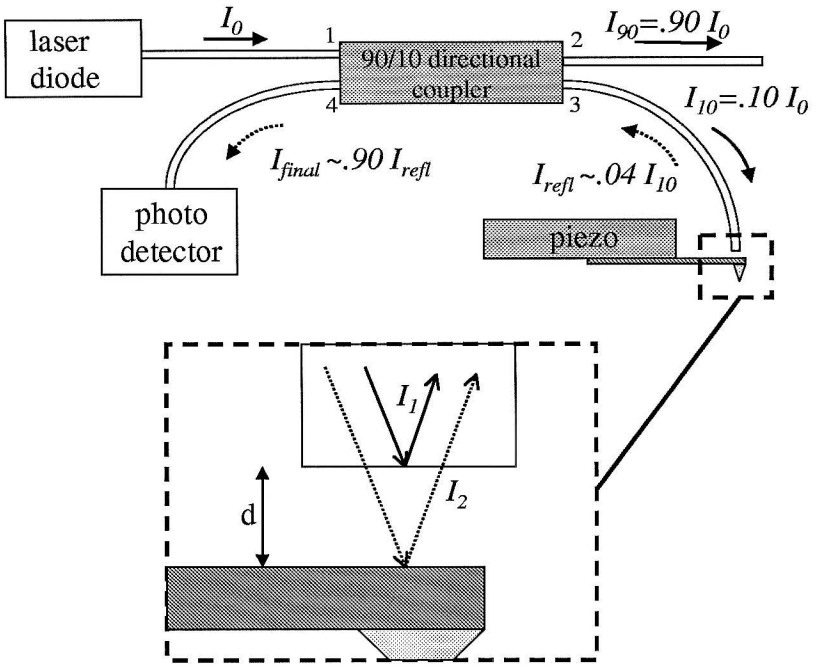

Figure 3.15: A schematic of the fiber optic interferometer. The maximum light intensity of each section of the interferometer is indicated. The detail shows the path difference the light beams, I_1 and I_2, travel to create interference fringes. The piezo maintains a constant DC distance d between the fiber and the cantilever.

intensity of the interference signal has a maximum value of

$$I_{\max} = I_1 + I_2 + 2\sqrt{I_1 I_2}, \tag{3.11}$$

where I_1 and I_2 are the intensities of the two beams. The intensity of the interference signal has a minimum value of

$$I_{\max} = I_1 + I_2 - 2\sqrt{I_1 I_2}. \tag{3.12}$$

The visibility V is defined by the relation

$$V = (I_{\max} - I_{\min})/(I_{\max} + I_{\min}) = 2\sqrt{I_1 I_2}/(I_1 + I_2), \tag{3.13}$$

where $0 \leq V \leq 1$.

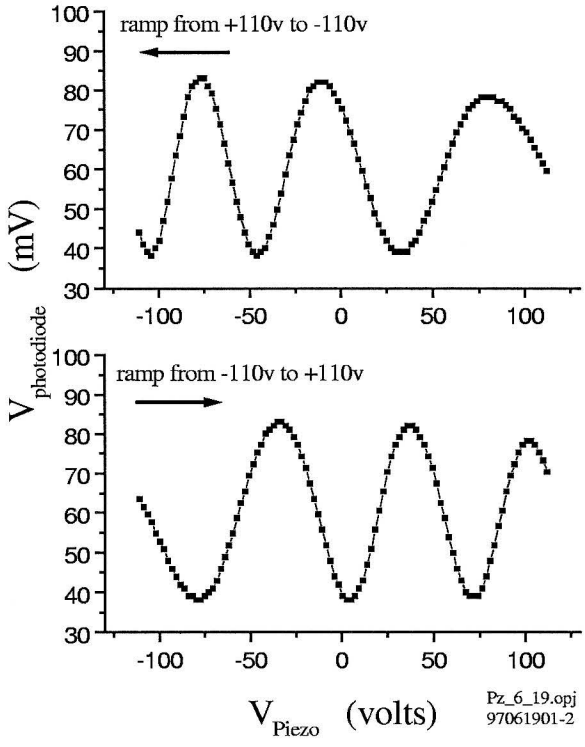

Figure 3.16: The voltage signal from the photodiode $V_{photodiode}$ as the voltage across the piezo V_{piezo} is varied. Interference fringes are observed. V_{piezo} varies the distance d between the end of the fiber and the cantilever. A lag in the response of the piezo to the applied voltage is evident.

The intensity of each beam is dominated by the reflection and transmission of the laser light at the fiber-air interface. The index of refraction of the fiber core is $n_{core} = 1.46$, and for air, $n_{air} = 1.00$. The reflection and transmission of light due to the fiber-air interface, derived by straightforward electrodynamics of light traveling through an interface, is given by

$$\begin{aligned} R &= \frac{(n_{core} - n_{air})}{n_{core} + n_{air}} = 0.04 \\ T &= 1 - R. \end{aligned} \tag{3.14}$$

For the fiber-air interface, the reflection is 4% and the transmission is 96%. A maximum visibility would be achieved if the total amount of light recoupled into the fiber from the Si

surface was approximately 4%.

Most of the transmitted light is lost traveling from the fiber to the Si surface and back over the distance $2d$. The light emerges from the cleaved fiber end over a solid angle. As this beam spreads out traveling over the distance $2d$, it further reduces the amount of light incident on the $5\mu m$ core of the fiber that can recouple into the fiber. If the cantilever and fiber end are not parallel, light reflecting from the Si surface will be directed away from the fiber. Also, the Si cantilever is not a perfect reflector, and will further reduce reflectivity.

In the FMRFM measurements, visibilities of 80-90% were typically achieved with careful alignment of the fiber and the cantilever. Since the visibility V is less than unity, not all of the light incident on the photodetector undergoes constructive or destructive interference. Therefore, there is a constant offset voltage, V_{offset}, as is observed in Figures 3.16.

3.7.2 Converting signal voltage to oscillation amplitude

An absolute calibration of the amplitude of the mechanical oscillations can be obtained with the interferometer via thermal oscillation amplitudes. These can be modeled exactly (see Appendix B). The total force (and therefore the total and number of spins in EPR/MRFM experiments) can be determined. The conversion of the photodetector signal in volts to an amplitude signal in Å is derived here.

Ramping the voltage across the piezo changes the distance d between the fiber end and the cantilever, resulting in interference fringes as shown in Figure 3.17. To maximize the response of the interferometer, d is chosen such that the photodetector DC signal is at the maximum slope of the fringe. i.e., the halfway point between the maximum and minimum DC signal. This steady-state position is maintained by a negative feedback circuit using the DC signal from the photodetector. Thus, if the distance between the fiber and the cantilever changes by a small amount x, it results in a large change in the photodetector output voltage, V_{signal}.

The signal as a function of distance is given by

$$V_{signal} = V_{offset} + A \sin\left(\frac{2\pi}{\lambda/2} x\right) \tag{3.15}$$

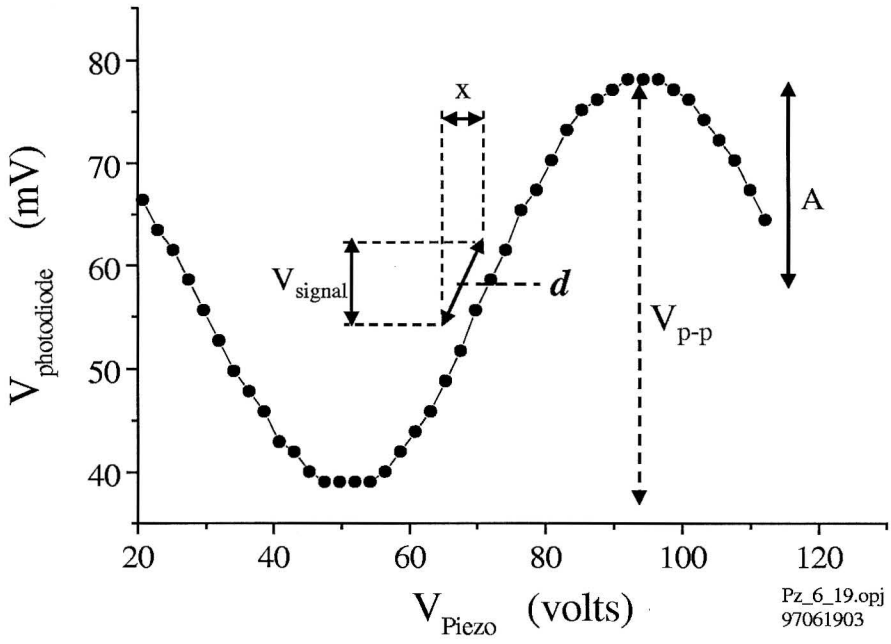

Figure 3.17: The output voltage of the photodector, $V_{photodiode}$, as the voltage across the piezo V_{piezo}, is ramped linearly. The signal shows a typical interference fringe of the interferomenter. See text.

where V_{offset} is a constant offset voltage due to *visibility* < 1, A is the amplitude of the fringe, and V_{p-p} is the peak to peak amplitude of the fringe. The value $\lambda/2$ appears in the denominator, rather than just λ, because the light must travel twice the distance x (to and from the fiber and cantilever). Taking the derivative of Eq. 3.15 and evaluating it at the equilibrium point $x = 0$ yields

$$\frac{\partial V_{sig}}{\partial x} = A\frac{4\pi}{\lambda}\cos(0) = \left(\frac{V_{p-p}}{2}\right)\frac{4\pi}{\lambda}, \tag{3.16}$$

where the relation $A = V_{p-p}/2$ has been used. For small oscillations about the steady-state position d, such as those due to cantilever vibrations, the change in the photodetector signal is approximately linear. Thus, ∂x is equated with the amplitude of the signal in units of distance $A\left[\text{Å}/\sqrt{Hz}\right]$. Similarly, ∂V_{sig} is equated with the change in voltage due to the signal from the photodetector $V_{signal}\left[mV/\sqrt{Hz}\right]$. The oscillation amplitude of the

cantilever is given in units of $\left[\text{Å}/\sqrt{Hz}\right]$ by the relation

$$A\left[\text{Å}/\sqrt{Hz}\right] = \frac{V_{signal}\left[mV/\sqrt{Hz}\right]}{V_{p-p}\,[mV]}\frac{\lambda\,[\text{Å}]}{2\pi}, \tag{3.17}$$

where $V_{signal}\left[mV/\sqrt{Hz}\right]$ is the amplitude of the photodetector signal in units of $mV/\sqrt{Hz}$, V_{p-p} is the voltage difference between the maximum and minimum of the fringe signal, and $\lambda\,[\text{Å}]$ is the wavelength of laser diode in Å.

3.7.3 Noise

There are four major sources of noise in the fiber interferometer: shot noise, back action noise, current fluctuations in the laser diode, and voltage fluctuations in the photodiode. The MRFM sensitivity will be limited by thermal noise provided that these sources produce noise levels below the thermal fluctuations of the mechanical resonator. Both the shot and back action noise are intrinsic to the interferometer. However, the current fluctuations in the laser diode and voltage fluctuations in the photodiode are instrumental and can be minimized through optimization.

Intrinsic noise

The shot noise in the optical fiber, similar to shot noise in resistors, is given by [48] [9]

$$A_{shot} = \sqrt{\frac{hc\lambda}{8\pi^2 I_0}\Delta f}, \tag{3.18}$$

where λ is the wavelength of the laser diode, I_0 is the intensity of the laser light, and Δf is the bandwidth of the measurement.

The back action noise, created by photons striking the surface of the mechanical resonator, is given by [48][9]

$$A_{back} = \frac{Q}{k}\sqrt{\frac{4I_0 h}{c\lambda}\Delta f}, \tag{3.19}$$

where Q and k are the quality and force constant of the cantilever.

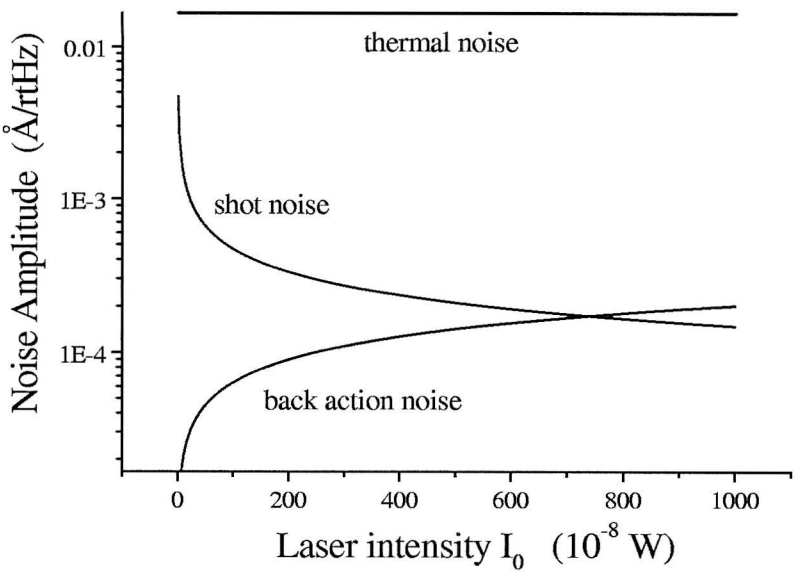

Figure 3.18: Noise amplitudes due to shot and back action noise compared to the thermal noise of the cantilever. The parameters are $T = 50mK$, $k = .05N/m$, $\lambda = 8750$Å, $Q = 10^5$, $\omega = 2MHz$, and $\Delta f = 1Hz$.

A comparison of the intrinsic noises in the system are shown in Figure 3.18 for a high Q, high frequency cantilever at low temperatures. Even in this regime that minimizes thermal noise, the thermal noise is orders of magnitude higher than the shot and back action noise of the fiber interferometer. Thus, thermal noise is the fundamental sensitivity limit in the MRFM system, even at low temperatures and for high frequency mechanical resonators.

Instrumental noise

The largest source of noise in the interferometer is caused by current fluctuations in the laser diode. Variations in the current directly translate to variations in the laser light intensity, and thus fluctuations in the photodetector signal. Current fluctuations have several sources: the current controller, temperature fluctuations, and reflections of the laser light back into the laser diode.

The current controller was built using the circuit schematic designed by Libbrecht and

Hall [49]. Pre-printed circuit boards and several of the low noise components were supplied by Libbrecht. This current controller has been optimized for low current noise to drive laser diodes. Typical current noise levels are $\leq 21nA$ for a $100kHz$ bandwidth ($66pA/\sqrt{Hz}$), and $\leq 45nA$ for a $1MHz$ bandwidth ($45pA/\sqrt{Hz}$). The best commercial current controller, the ILX model LDX-3620, has a minimum noise of $\leq 100nA$ for a $10kHz$ bandwidth and $\leq 850nA$ for a $10MHz$ bandwidth during battery operation. The current fluctuations of the Libbrect model produce a noise of $2nV/\sqrt{Hz}$ in the photodetector signal.

The current controller also has a dual stage temperature controller to stabilize the laser diode. Comparisons of the noise floor in the MRFM interferometer before and after temperature controlling the laser diode reduced the noise by a factor of 2 or more.

The typical observed noise floor in FMRFM experiments is $\sim 40\mu V/\sqrt{Hz}$, which corresponds to an amplitude noise of $\sim .005\text{Å}/\sqrt{Hz}$. This noise floor is much larger than the noise levels produced by the photodetector ($2nV/\sqrt{Hz}$) and the current source ($2.7nV/\sqrt{Hz}$). It is also significantly larger than the shot and back action noise. Thus, the noise floor is dominated by the only other noise source is the system, the current fluctuations in the laser diode caused by reflected light.

The main source of light reflected back into the laser diode is from the fiber interfaces throughout the system. Such interfaces occur at several points along the interferometer paths: the laser-fiber pigtail connection, the fiber-fiber interface connecting the pigtailed laser diode to the directional coupler, and the fiber-air interfaces at the end of arms #2 and #3 (Fig. 3.15). Noise can be minimized by optimizing the laser to fiber interface through the use of the pigtail connection. Index matching gel can be used in the fiber-fiber connections. All FC connectors at the end of fibers were "PC polished," which reduces the reflection to -20dB compared to a simple polish.

As an experimental note, it has been determined that a FC connection in the fiber arm between the pigtail laser and the directional coupler produces a negligible increase in noise. It is useful to be able to separate the laser diode and the coupler, especially if one of the components fail. However, a FC connection in the fiber arm between the cantilever and the coupler produces almost an order of magnitude increase in the noise floor.

Singlemode fiber was used throughout the interferometer system. Both a singlemode laser and a mutlimode laser, described earlier, were used. The singlemode laser was pigtailed into an isolator to reduce reflections of the laser light back into the laserdiode. The multimode laser did not have an isolator. However, multimode lasers are known to be more stable against reflected light than singlemode lasers. Similar noise floors were achieved with both systems, typically a few $\times 10^{-3}\text{Å}/\sqrt{Hz}$ at $10kHz$.

A variety of interferometers have been used throughout the literature. Systems have employed single and multimode laser diodes, with and without isolators, RF input into the current source to prevent mode hopping of multimode lasers, HeNe lasers with beam splitters, index matching fluids, and reference signals from the #2 arm of the directional coupler. The noise floors obtained in these systems ranged from $.034\text{Å}/\sqrt{Hz}$ for $0.1 - 1.0kHz$, to $5 \times 10^{-4}\text{Å}/\sqrt{Hz}$ for $1kHz$ and higher [50][51][52][53][54][55]. The best noise obtained was $1.7 \times 10^{-4}\text{Å}/\sqrt{Hz}$ for above $2kHz$ with a HeNe laser system [52]. However, the best noise floors were often obtained by reflecting off a pure Si substrate, rather than a cantilever. Typical noise floors in the literature, which include reflecting off a cantilever, were a few $\times 10^{-3}\text{Å}/\sqrt{Hz}$.

3.8 Miscellaneous

3.8.1 Cantilevers (thermal heating)

The commercial cantilevers used in early experiments (DPPH, Co films, and the early YIG studies) had a thin Al coating to enhance reflectivity. Unfortunately, when placed in the RF field, eddy current heating occurred. For YIG, an insulator, this heating was not a significant problem. For the thin Co films, eddy current heating of the cantilever and the film resulted in the destruction of several samples.

The thermal peak, a function of temperature and the physical characteristics of the mechanical resonator, has been used as a temperature sensor of the RF heating. The spectra of the Al coated commercial cantilever as a function of RF power into the microstrip, and the theoretical fits, are shown in Figure 3.19. The spectral density used to fit the spectra

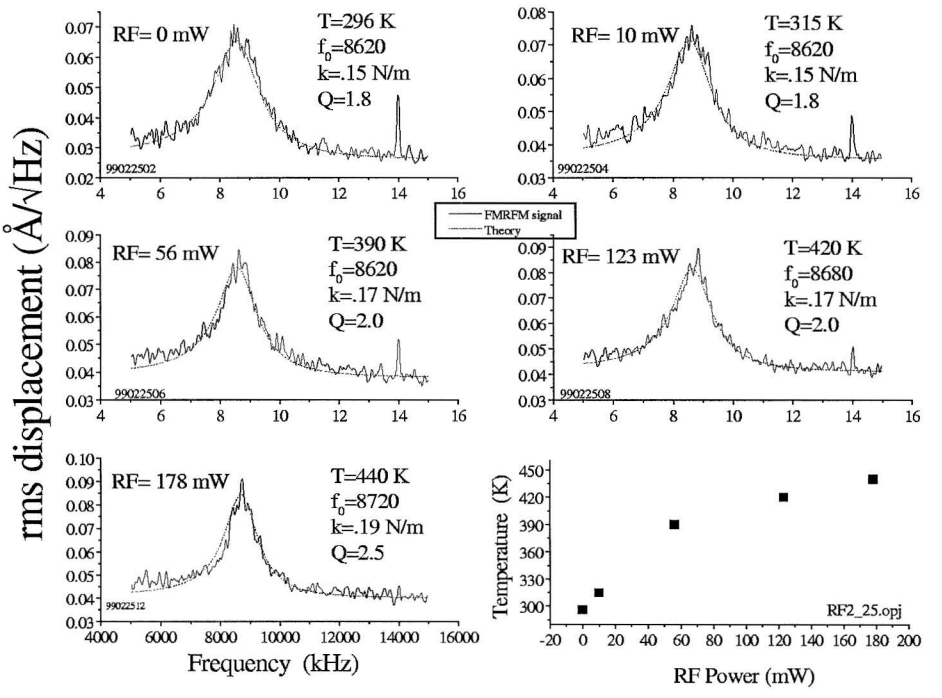

Figure 3.19: Spectra and theoretical fit of the RF heating effect on Al coated commercial cantilevers.

is derived in Appendix B. A significant increase in the temperature was required to fit the experimentally obtained thermal peak.

The lower right graph of Figure 3.19 shows the temperature of the cantilever versus RF input into the microstrip. A temperature increase of almost 100K is shown for our typical operating power of $56mW$. For the thin single and multilayer films ($\leq$ 100Å) sputter deposited onto the commercial cantilevers (discussed in Chapter 5), this large temperature appeared to result in the samples physically deteriorating on the cantilevers.

Spectra were also taken of a non-coated commercial cantilever, identical in physical properties to the Al coated cantilever, as a function of RF power. No change in the thermal peak spectra was observed over the range of 0 to $192mW$.

An Auger electron Scan (AES) was used to examine the physical effects of RF heating

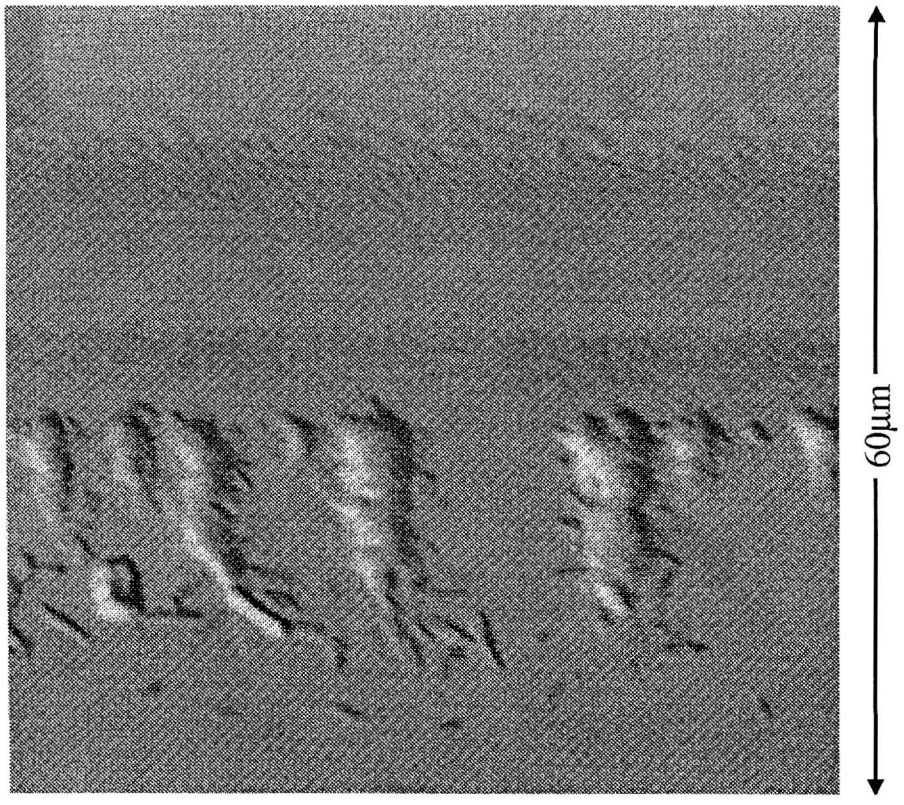

Figure 3.20: AES scan of the Co film after exposed to the RF field for 5 mintues. RF current heating results in surface stress and severe oxidation.

on Co thin films. Two 300Å thick Co film were sputter deposited onto a Si substrates at the same time in order to have identical deposition properties. One sample was placed in the RF field (similar to our cantilevers) for 5 minutes, and the other sample was not. AES scans of the two samples revealed that the RF heated Co film had an oxygen to cobalt ratio twice that of the non-RF exposed sample. Furthermore, the scans revealed increased surface roughness (bubbling of the surface) in the RF sample, shown in Figure 3.20. The surface bubbling could also be caused by stress in the film in addition to the heating effect. Heating would allow the stressed regions to pull away from the Si surface.

3.8.2 Temperature

All FMRFM experiments were performed at room temperature. Lower temperatures increase the sensitivity of the MRFM apparatus (see Chapter 2). However, there are several reasons for performing these studies at room temperature:

1. Lower temperatures increase the linewidth of ferromagnets. For thin metal films, this increase can be orders of magnitude. This would increase the difficulty of characterizing the samples and obtaining spectra, and would reduce the resolution.

2. Lower temperatures increases the RF heating problem. Air serves as the main medium for heat transfer from the sample. In vacuum, severe heating can destroy the sample.

3. The signals at room temperature were large enough to explore FMRFM capabilities and resolution.

4 Understanding FMRFM in microstructures (YIG studies)

Defining the concept of spatial resolution within a ferromagnetic sample, and understanding how FMRFM can provide local imaging, are complex issues. The resonance fields and the amplitudes of ferromagnetic modes involve complicated interactions between the sample, the external fields, and the probe magnet. In this work, extensive measurements and analysis have been performed on YIG microstructures to develop understanding of the FMRFM technique and spatial resolution in ferromagnetic materials.

Use of YIG microstructures provided several advantages. First, YIG is well studied, and the magnetostatic modes can be calculated explicitly. Thus, physical interactions between the sample and the FMRFM apparatus are more readily apparent and understood. Second, YIG is an insulator. This reduces the eddy current heating problem encountered with thin metallic films, as was discussed in Chapter 3. Third, the magnetostatic modes provide spatial variations in the sample's magnetization on the micron scale. This allows us to determine the ability of FMRFM to spatially resolve the varying mode amplitudes in an extended sample on a similar scale. This is an improvement over our previous measurements of thin metallic films, in which the entire sample of length of $40\mu m$ fit within the resonance volume determined by the gradient field. Local spatial variations across an extended sample could not be obtained in those studies (see Chapter 5). Finally, the micron dimensions of the YIG samples result in a total magnetic moment that produces a signal-to-noise (SNR) comparable to previous measurements of DPPH and Co films of micron dimensions. Comparable SNR enables understanding of the physical effects of each sequential improvement to the FMRFM apparatus in a controlled fashion. Data obtained from new techniques is compared with data obtained from earlier techniques to elucidate the improvements. For example, the comparison of FMR data obtained from a sample mounted on the cantilever

versus data obtained from a sample scanned by a probe magnet (which is mounted on the cantilever).

The chapter is organized into four main sections. In general, the first two sections describe the development and understanding of how the field from the probe magnet can affect the dispersion relation in two limits: (a) the low field limit (a few Gauss), in which the probe magnet only weakly perturbs the interaction volume (i.e., the region most strongly affected by the local gradient field) such that any effects are not discernible, and (b) the high field limit, in which the probe magnet perturbs the interaction volume very significantly, and that its effects are readily observable. The final two sections discuss the details of signal detection using the FMRFM technique. A summary of the key points of each section is given below.

The first section, "spatial resolution," includes physical details of the samples followed by the analysis of magnetostatic modes in two sets of YIG microstructures. Our early studies (parallel vs. perpendicular geometry) on a YIG particle yield a qualitative agreement between FMRFM measurements and established theory. Subsequent measurements upon a series of YIG rectangles yield a quantitative agreement between FMRFM measurements and the simple theory developed for microstructures. The detailed analysis of the YIG series establishes the mode amplitudes and resonance fields for a sample that is only weakly perturbed by a small field from the probe magnet. In these experiments, mapping of mode amplitudes within the sample was attained with an unprecedented spatial resolution of $15\mu m$.

The second section, "effect of the probe magnet on the dispersion relation," explores the regime in which the dispersion relation of the sample becomes significantly perturbed by a stronger field from the probe magnet. A simple theory is derived to approximate the observed effects upon the magnetostatic mode spectra from the perturbed interaction volume of the sample.

The third section, "effects of the FMRFM technique on signal detection," determines the dependence of the FMR signal on the external fields. The shape and intensity of the

FMR signal can be distorted if the RF and modulation fields are not optimized.

The forth section, "ongoing research," describes work that is still in progress to determine the effects of the FMRFM technique upon signal detection.

Two key results were obtained in these studies. First, the dispersion relation of the sample is relatively unperturbed when the field produced by the probe magnet is only a few Gauss. The resonance fields and intensities of the modes are largely determined by the sample dimensions and by the external field over the entire sample. They are not determined by the local gradient field from the probe magnet as they are for EPR and NMR MRFM. This result is established by the relatively good fit between experimentally and theoretically determined values of the modes.

Second, the dispersion relation of the sample is perturbed when the field produced by the probe magnet is $\sim 60G$ at the sample surface. The effect of the probe magnet is to modify the RF absorption of certain modes. However, the resonance fields of the perturbed modes are still largely determined by the average external field over the entire sample.

Detailed analysis of FMR mode amplitudes and field spacings have never been attained before on the size scale achieved in this work The FMRFM technique has yet to be optimized to determine the minimum detectable moment possible, but it is already sensitive to sample dimensions several orders of magnitude smaller than those which conventional methods can detect. This offers exciting prospects for measurements on individual magnetic microstructures.

4.1 Spatial resolution

In these studies, amplitude variations of FMR modes within small YIG structures have been resolved with a spatial resolution of $\leq 15\mu m$. The amplitude variations in the RF component of the magnetization within the sample correspond well to simple theoretical models. The sensitivity provided by FMRFM has enabled measurement upon the micron-scale samples, which are orders of magnitude smaller than those resolved via conventional methods.

Furthermore, the relative phase variations of the time-varying sample magnetization were detected with a spatial resolution of $2\mu m$.

4.1.1 Samples

The single crystal yttrium iron garnet (YIG) films used in these studies were grown on gadolinium gallium garnet (GGG) substrates by liquid phase epitaxy (LPE) [56]. They have known, but varying thicknesses and crystal axis directions. The vast majority of our data comes from a wafer (referred to as the "T-18"batch) of single crystal YIG with a thickness of $\approx 3\mu m$ on the polished face. The GGG substrate from which samples are patterned was cut into smaller pieces with a diamond scribe for processing purposes. The details of the physical characteristics of our YIG samples are listed below. Each unique sample has been given a short name, which will be referred to in the remainder of this paper. All of the following samples were from the "T-18" batch.

R-Rough This sample was approximately rectangular in shape, with a width of $20\mu m$, a length of approximately $150\,\mu m$, and a thickness of $3\,\mu m$. A diagram of the sample is shown in Figure 4.1. This sample was obtained by shattering a small piece of the YIG and choosing a chard of symmetrical shape and with very little GGG substrate attached. The chard was then affixed onto the end of a commercial cantilever, with its long axis parallel to the long axis of the cantilever. A probe station and Stycast 1066 was used to affix the sample to the cantilever. One end of the YIG had a rectangular shape, but the other end had a more triangular shape. For each mode, this created amplitude differences between the two sides, although their qualitative behavior was the same. The rectangular half, being more symmetric, produced modes that fit rough calculations for field spacing and amplitudes. The triangular half followed FMR theory qualitatively, but was too irregular for quantitative analysis.

R-Series A series of microscopic rectangles was ion milled from a $1cm \times 1.5cm$ section of the wafer, and are shown in Figure 4.2. The sample was patterned with photoresist

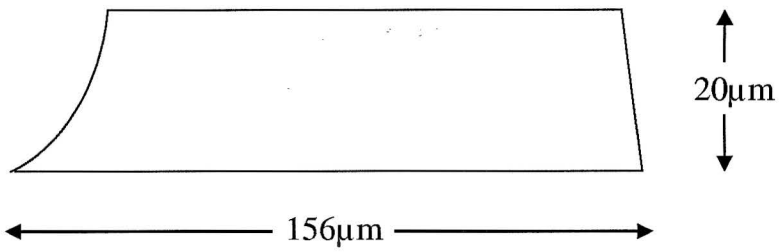

Figure 4.1: A schematic of the YIG sample R-Rough. A particle broken from a piece of single crystal YIG, $3\mu m$ thick, and affixed to a commercial cantilever with expoy.

at Caltech, and then ion milled at IBM by Richard Campbell [57]. A protective masking layer of photoresist was patterned onto the YIG surface using optical lithography. Details are given in Appendix C. Since the differential milling rates were approximately 3:1 (photoresist:YIG), a photoresist thickness of at least $15\mu m$ was required. The sample was patterned and ion milled in two separate sessions. Due to a calibration error of IBM's new ion milling machine, the first run resulted in milling to a depth of only $2\mu m$. The second run milled to an additional depth of $1.5\mu m$. Despite the two-step process, the resulting structures had uniform side walls.

The sample contains several series of YIG structures, all of which are $\sim 3\mu m$ thick:

- $20\mu m$ Series: These are rectangular in shape with width $= 18\mu m$. The series of lengths (L^{20}) include $L^{20} = 320, 160, 80, 40$, and $20\mu m$.
- $10\mu m$ Series: These are rectangular in shape with width $= 8\mu m$. The series of lengths (L^{10}) include $L^{10} = 160, 80, 40, 20$, and $10\mu m$.
- $100x100\mu m$: These are square in shape with width $= 98\mu m$ and length $= 97\mu m$.
- Arc Series: These are crescent shaped (C-shaped) with width $= 18\mu m$. The lengths are $45\mu m, 103\mu m$, and $90\mu m$.

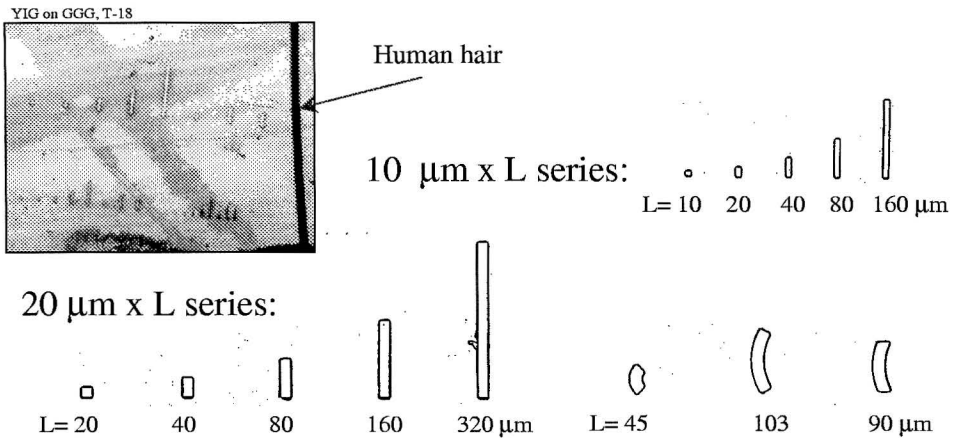

Figure 4.2: Photograph of the YIG structures on a $1cm \times 1.5cm$ GGG substrate. For size comparison, a human hair is included next to the structures. A detailed enlargement of the $20\mu m$ and $10\mu m$ series is also shown.

2mm Disks These samples were a set of $2mm$ diameter YIG disks. They were cut with a round saw bit and polished to reduce their thickness to approximately $1\mu m$. The disks were used previously in experiments of controlled chaos by P.E.Wigen [58].

4.1.2 Perpendicular vs. parallel geometry (early studies)

Early YIG studies [59] were performed on the sample *R-Rough*, a small single crystal YIG particle approximately rectangular in shape. The external field $\vec{H}$ was aligned both perpendicular and parallel to the plane of the YIG film, and the RF field was 7.74 GHz. These early studies demonstrated key properties of parallel and perpendicular FMR to verify the sensitivity the force detection method. A spatial resolution of $50\mu m$ was achieved with a NdFeB particle glued to a cantilever, and a resolution of $15\mu m$ was achieved with newly developed NiFe tipped cantilevers. Approximate calculations and modeling showed a reasonable fit to the data. These experiments were the first demonstration of spatial resolution on this size scale [59].

For the case where an external field is applied parallel to the YIG film plane ($\vec{H}$ || YIG film), a high coercivity magnet (or "hard" magnet) was used to create the gradient field.

This magnet consisted of a wedge shaped NdFeB particle, approximately $50\mu m \times 20\mu m \times 15\mu m$, glued to the end of a commercial AFM cantilever ($f_c \sim 8\,kHz$) and pre-polarized in an $8T$ field along the direction of $\vec{H}$. This was the predecessor to the ultrasharp tips, described in Chapter 3, and provided the first measurements of FMRFM with the probe magnet on the cantilever providing the gradient field.

For the external field applied perpendicular to the YIG film plane ($\vec{H} \perp$ YIG film), an improved detection cantilever was used. The probe magnet on the commercial AFM cantilever was created by sputtering 1200 Å of Permalloy (sputtered from a $Ni_{19}Fe_{89}$ target) solely in the region of the ultrasharp tip (see Chapter 3, Fig. 3.13). The cantilever frequency was $f_c \approx 18\,kHz$.

Perpendicular force geometry ($\vec{H}$ || YIG Film)

In this geometry (Fig. 3.3), the external field $\vec{H}$ is aligned parallel to the film plane, and directed along the $150\mu m$ length of the sample and along the long axis of the NdFeB particle. The z axis is defined to be along the direction of the external field $\vec{H}$. This geometry requires the use of the "perpendicular force geometry," where the force on the cantilever is $F = m\,\partial H_z/\partial y$ (i.e., the induced force and cantilever motion are perpendicular to $\vec{H}$). The external field was greater than $2\,kG$, ensuring that the sample was saturated. A tip-to-sample separation of $20\mu m$ was used.

In this field configuration, higher order modes are expected to occur upfield from the fundamental mode [17]. This was indeed observed. Figure 4.3 shows the evolution of the FMRFM spectra as the probe magnet on the cantilever was scanned from the center to the edge of the YIG film. The largest feature, the fundamental mode, was maximal when the probe magnet was positioned over the center of the sample, decreased to a minimum at the sample's edges, and then vanished when the probe magnet was far from the sample.

The smaller features correspond to higher order magnetostatic modes. These modes correspond to the discrete standing wave numbers k_z and k_x, where $\hat{z}$ and $\hat{x}$ are in the plane of the film. As the probe magnet is scanned towards the edge of the sample, the higher

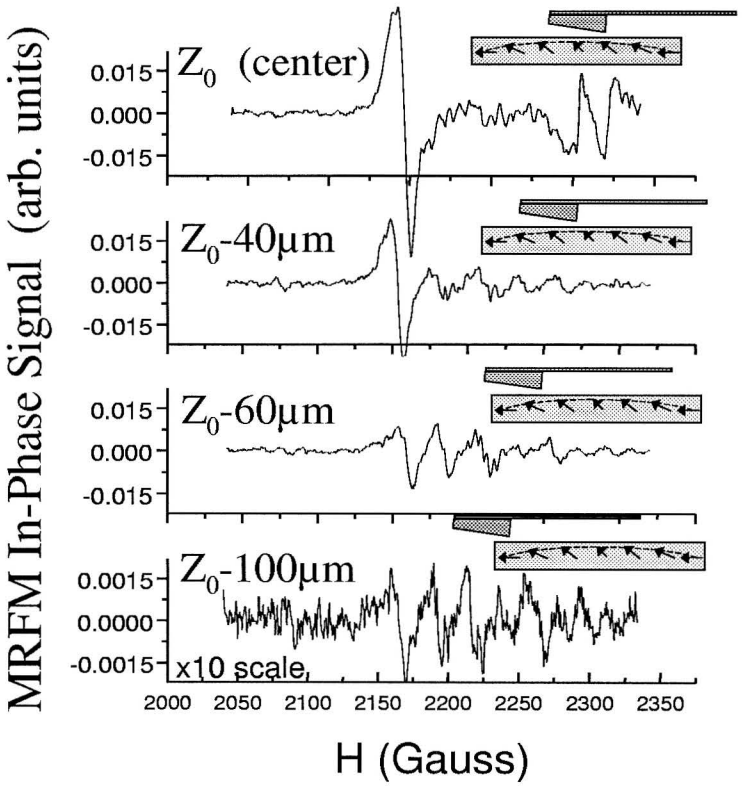

Figure 4.3: Spectra of the R-Rough YIG sample for the parallel field configuration. The sample is scanned from its center to its edge along the direction of its $150\mu m$ length. The variation of the amplitudes of the fundamental and higher order modes is observed.

order modes become more clearly defined in the spectra. This effect may be attributed to the rectangular shape at this edge of the sample, which creates more uniform boundary conditions, and thus better defined modes, than the asymmetric (roughly triangular) shape at the other end of the sample (Fig. 4.1).

Within the approximation of Story [29], samples with finite length L and width w lead to quantized values of the wave numbers, $k_z = \frac{n_z \pi}{l_z}$ and $k_x = \frac{n_x \pi}{l_x}$. The expected field spacings between the modes (k_z, k_x) were estimated using the "near fundamental resonance approximation," calculated by Hurben for thin films (see Ref. [31]). This approximation assumes very thin films ($L, w >> d$) of infinite lateral dimensions and the fundamental mode $k_y = 0$ along the direction of the thickness. The *R-Rough* sample has finite lateral

dimensions and is not very thin, thus the approximation may not yield very precise values. It is used here to determine rough values for the expected field spacing between modes. For $\vec{H}$ parallel to the film plane, the approximate dispersion relation is

$$\frac{\omega}{\gamma} \approx H + 2\pi M_S - \pi M_S d \left[\left(\frac{n_z \pi}{L} \right)^2 + \left(\frac{n_x \pi}{w} \right)^2 \right]^{1/2}, \tag{4.1}$$

where L, w, and d are the length, width, and thickness of the sample.

This relation (Eq. 4.1) does not include field shifts of the modes which may arise from either the anisotropy energies, or from the non-zero demagnetization factors of a sample with finite lateral dimensions (the approximation $N_x, N_z = 0, N_y = 4\pi$ no longer applies). However, these effects can be crudely modeled by replacing $4\pi M_S$ with $4\pi M_{eff}$, which includes the effects of the finite geometry and anisotropy energy. (From Chapter 2, Eq. 2.21, the effective field H_{eff} in the dispersion relation was defined by the relation $4\pi M_{eff} = 4\pi M_S - \frac{2K_{u2}}{M_S}$.)

Fitting the experimental and theoretical values of the resonance field of the fundamental mode yields a value of $4\pi M_{eff} = 1.4\,kG$, less than the bulk value of $1.750\,kG$ as expected. A superior method to approximate the modes of microstructures was developed (see Chapter 2) to include the demagnetization effects resulting from the sample dimensions. This improved approximation was used to evaluate data from the more precise rectangular *R-Series* samples in subsequent studies (see section "YIG microstructures").

The predicted field separations (Eq. 4.1) for the fundamental and higher order modes along the sample's $150\mu m$ length ($n_z = 1, 3$, and 5) are 13, 23, and 31 Gauss respectively. The hidden modes ($n_z = 2, 4, ...$) do not couple appreciably to the uniform RF field, due to absorption rules derived in Chapter 2, and are not observed. The experimentally measured mode separations for the observed modes are 26-29 Gauss, which correspond fairly well to the estimated values. The difference between the predicted and observed separations can be accounted for by the inhomogeneity of the internal field due to the non-rectangular shape of the sample. From Eq. 4.1, it is evident how the field separations depend directly upon the dimensions. Thus, the measured mode separations clearly do not correspond to the $20\mu m$ dimension, since the field separations for these modes should be of order $300G$.

This is an order of magnitude larger than the observed features.

In these experiments, spatial resolution appears to be determined by the dimensions of the probe magnet. Hence, the lateral resolution of the FMR modes was limited by the $50\mu m$ length of the NdFeB particle employed as the probe magnet. Only the fundamental mode exhibited significant amplitude variation as the cantilever was scanned across the $150\mu m$ length of the sample. Higher order modes have significant spatial variations that are smaller than the $50\mu m$ length scale of the particle. Thus, as expected, their contribution to variations in the FMR signal intensity tend to be spatially averaged.

The connection between the spatial resolution attained and the physical dimensions of the NdFeB particle were further verified by measurements of the signal intensity as the tip was moved away from the surface of the sample. Starting from $3\mu m$ above the sample surface, the signal intensity was reduced by half at a distance of $18\mu m$ above the surface. This is roughly consistent with the $15\mu m$ thickness of the NdFeB particle.

Parallel force geometry ($\vec{H} \perp$ YIG film)

In this geometry, the external field $\vec{H}$ is aligned perpendicular to the plane of the sample film and parallel to the long axis of the NiFe-coated cantilever tip. This is shown in Figure 3.2. Again, the z axis is defined to be along the direction of the external field $\vec{H}$. This configuration is what we term the parallel force geometry. In this case, the force on the cantilever is $F = m\ \partial H_z/\partial z$. The external magnetic field was greater than $4kG$, insuring that the sample and probe magnet were saturated. In the present case, the fundamental mode is expected to occur at much higher magnetic fields than for the parallel configuration. The applied field must provide enough energy to overcome the demagnetization field of the film (Eq. 2.22, Eq. 2.23). Also, from the dispersion relation (Eq. 2.33), the higher order modes are expected to occur downfield from the fundamental mode as the external field is swept [17]. Both characteristics were observed. As before, the detection cantilever was scanned from the center to the edge of the YIG film along its longest ($150\mu m$) dimension. The resulting spectra are shown in Figure 4.4.

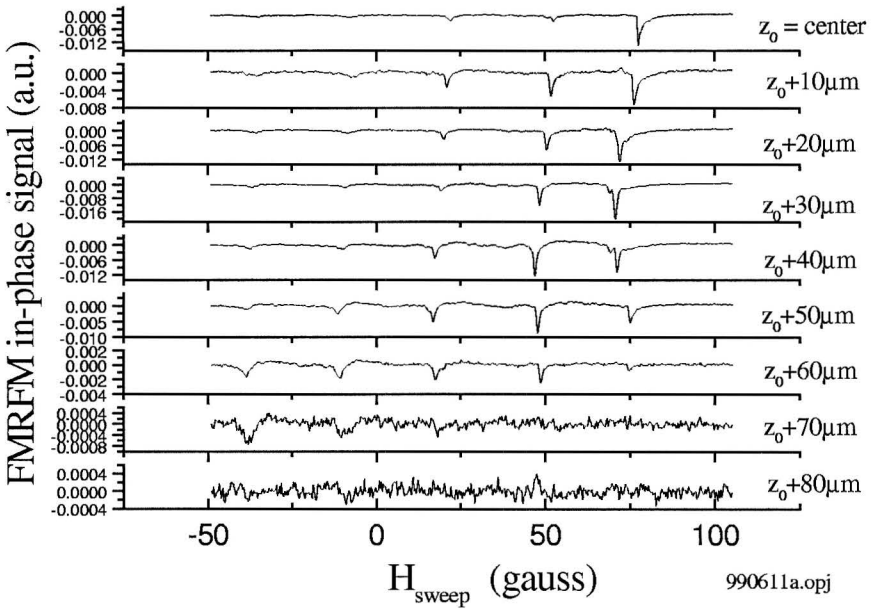

Figure 4.4: Spectra of the R-Rough YIG sample for the perpendicular field configuration. The sample is scanned from its center to its edge along the direction of its $150\mu m$ length. The variation of the amplitudes of the fundamental and higher order modes is observed.

The largest feature, the fundamental mode, was maximal when the probe magnet was positioned over the center of sample. It decreased to a minimum at the sample's edges, and then vanished when the probe magnet was moved past the sample edge (Figure 4.4). The cantilever with the NiFe-coated tip greatly improved the sensitivity. This probe magnet demonstrated a spatial resolution of $\approx 15\mu m$, consistent with the Si tip height of $12-15\mu m$. Amplitude variations in several higher order modes were also resolved. The first higher order mode has a wavelength one–third the length of the fundamental mode. Thus, the peak amplitude should occur approximately at $z \approx 50\mu m$, as was observed (Figure 4.5). Experimentally, the mode shapes and amplitude peaks within these samples are not as simple as predicted by idealized theory, since they are affected by the sample irregularities.

At the center of the film, the modes are found to be $\sim 27G$ apart. This is similar to values obtained in the parallel field configuration, as expected. Furthermore, the relative amplitude of the modes decrease as mode number increases — a behavior which follows the

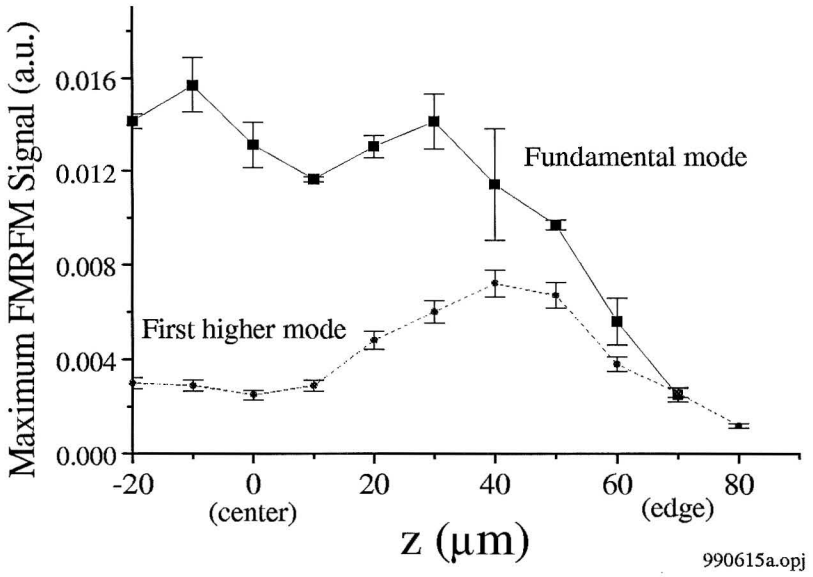

Figure 4.5: The amplitude of the fundamental mode and the first higher order mode of the *R-Rough* YIG sample, as the cantilever is scanned along the $150\mu m$ length of the film. H $\perp$ film plane.

predictions of Damon and Esbach (DE theory) [24].

In the parallel force geometry, scanning was typically performed $10 - 15\mu m$ above the surface of the sample. Measurements of signal intensity confirmed the estimated resolution of $15\mu m$, which corresponds to the probe magnet dimensions. For scans across the width of the sample, the signal strength was found to decrease by half within $15\mu m$ of the sample center. Raising the cantilever from the surface of the sample, the signal strength also decreased by half when the cantilever tip was about $15\mu m$ from the surface.

The data from this sample provided the first demonstration of spatial resolution of FMR on a microscopic level, and within an extended ferromagnetic sample. The spatial variations in the amplitudes of the magnetostatic modes of a microscopic YIG sample were observed on a $15\mu m$ scale, and could be qualitatively understood using DE theory. Several other characteristics were observed, such as the dependence of the field location of the higher order modes upon external field orientation, and an effective field reduced from

the bulk value ($4\pi M_{eff} < 4\pi M_S$) attributed to demagnetization factors and anisotropy energies. The spatial resolution corresponding to the dimensions of the probe magnet were also confirmed.

4.1.3 Shift of fundamental modes due to sample size

In subsequent work, the well defined geometries of the YIG samples in the *R-Series* produced "textbook quality" spectra. The high quality of the data permitted detailed analysis of the mode spectra for these samples. Such resolution has not been obtained before in microscopic samples. Scans across the sample revealed amplitude variations of the magnetostatic mode spectra with a spatial resolution of $15\mu m$. The data also demonstrates the ability of FMRFM to detect the relative phase of the magnetization oscillations.

Experimental details

The sample *R-Series* (Figure 4.2) contains two series of YIG rectangles, having thickness $\approx 3\mu m$. These series contain YIG structures with lateral dimensions of (a) $20\mu m \times 320, 160, 80, 40, 20\mu m$ and (b) $10\mu m \times 160, 80, 40, 20, 10\mu m$. Measurements were carried out with the external field perpendicular to the sample plane, and employed the parallel force geometry. An RF frequency of $7.6\,GHz$ was used.

The majority of the data was obtained from the "old" FMRFM set-up (as discussed in Chapter 3), with the external magnetic field H supplied by a small NdFeB permanent magnet ($\frac{1}{4}$" diameter, $\frac{1}{2}$" long). Measurement of the FMR spectra for the $20\mu m$ series were repeated in the "new" FMRFM set-up (also Chapter 3) to calibrate the absolute $\vec{H}$ fields taken with the "old" FMRFM system.

The cantilever frequency was $f_c \approx 18kHz$, and its force constant was $k = 0.1N/m$. Anharmonic modulation was used [5]. The external field was modulated, by the H_{mod} coils, with an amplitude of $35mV$ ($\approx 2Gauss$) at a frequency of $f_{H\,\text{mod}} = 13kHz$. The RF field was 100% amplitude modulated at a frequency of $f_{RF\,\text{mod}} \approx 31kHz$. The precise frequency

of this RF modulation was fine tuned to yield a difference frequency $|f_{RF\,\mathrm{mod}} - f_{H\,\mathrm{mod}}|$ that matched the cantilever frequency f_c.

Fundamental mode dependence on sample length

The spectra for the $20\mu m$ series, with lengths of $L^{20} = 320, 160, 80, 40$, and $20\mu m$, are shown in Figure 4.6. The spectra for $10\mu m$ series, with length of $L^{10} = 160, 80, 40, 20$, and $10\mu m$, are shown in Figure 4.8. As the sample lengths decrease, the shift of the fundamental modes $(n_x, n_y, n_z) = (1, 1, 0)$ to lower resonance fields is clearly evident. The dependence of the field spacing between higher order magnetostatic modes upon the sample size is also clearly manifested in these spectra. The experimental values compare well with the expected theoretical values, as shown in Figures 4.7 and 4.9.

The uncertainty of $\pm 5G$ in the external field is due to the thermal drift within the FMRFM apparatus. Heat was produced by the coils providing the $\pm 300G$ field sweep. The associated thermal expansion of various components within the apparatus resulted in the drift of the spacing between the sample and the NdFeB magnet which supplied the external field. The expansion reduced the external field at a rate of approximately $0.2G/\min$.

In the shorter samples, the demagnetization effect from the edges increases. This acts to reduce the internal fields, H_i, and shifts the fundamental mode to lower fields. The demagnetization fields, $H_{d,i}$, are calculated in Appendix D as a function of sample dimensions. The results are shown in the following tables:

For the $20\mu m$ series:

$L^{20} =$	$320\mu m$	$160\mu m$	$80\mu m$	$40\mu m$	$20\mu m$
$H_{d,z}$ (G)	1588	1587	1584	1570	1520
$H_{d,x}$ (G)	1	2	10	36	117
$H_{d,y}$ (G)	166	165	163	149	117

For the $10\mu m$ series:

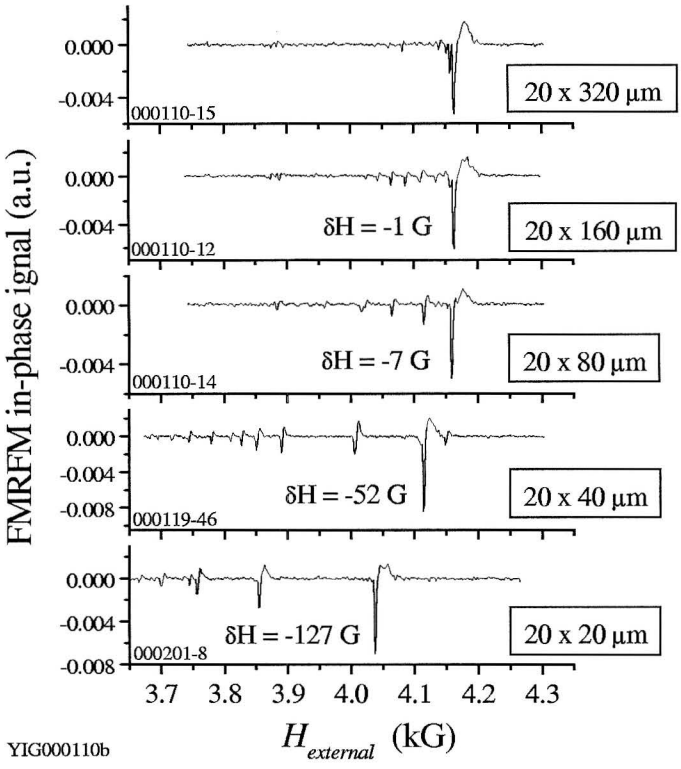

Figure 4.6: (a) Spectra of the $20\mu m$ series. The dependence of the mode on the sample length, due to increasing demagnetization effects on the internal field, is clearly evident.

$L^{10} =$	$160\mu m$	$80\mu m$	$40\mu m$	$20\mu m$	$10\mu m$
$H_{d,z}$ (G)	1429	1427	1419	1390	1298
$H_{d,x}$ (G)	1	6	20	74	228
$H_{d,y}$ (G)	326	322	316	290	228

The dispersion relation for these microstructures, developed in Chapter 2, determines the resonance fields of the fundamental modes as a function of sample dimensions. This yields

$$\left(\frac{\omega}{\gamma}\right)^2 \simeq [H - (H_{d,z} - H_{d,x})] \times [H - (H_{d,z} - H_{d,y})]\,. \tag{4.2}$$

Values were calculated for $d = 3\mu m$, $4\pi M_S = 1760G$, $g = 2$, $RF = 7.6GHz$, and the demagnetization fields $H_{d,i}$ listed in the tables above. The experimentally and theoretically

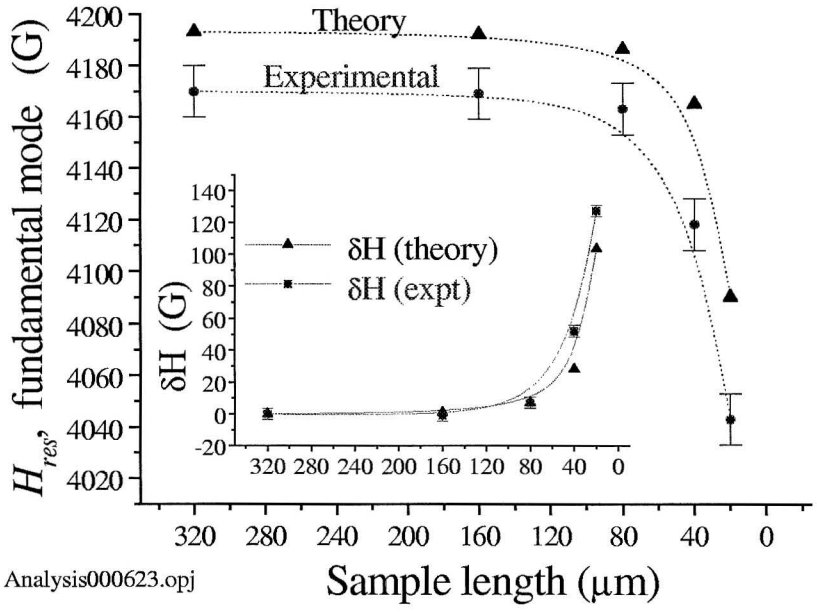

Figure 4.7: The resonance field H of the fundamental mode vs. sample length L^{20}. The offset from theory is due to crystalline anisotropy effects. (Insert) The field difference in the mode compared to the longest sample in the series ($L^{20} = 320\mu m$).

determined values, shown in Figures 4.7 and 4.9, are in excellent agreement, offset by a constant field. This offset may be attributed to anisotropy energies, which were not included in the theoretical estimates, or the uncertainty in thickness. Measurement of the FMR spectra for the $10\mu m$ series were not repeated in the "new" FMRFM set-up. Thus, a miscalibration of the external field strength could account for the larger field offset in the $10\mu m$ series spectra.

The field differences between the fundamental modes of each sample length is a good indicator of how well experimental values correspond to the theoretical predictions. Calculating the difference eliminates constant offsets in the field which may result from anisotropy energies and field calibration errors. The fundamental mode of the longest sample in each

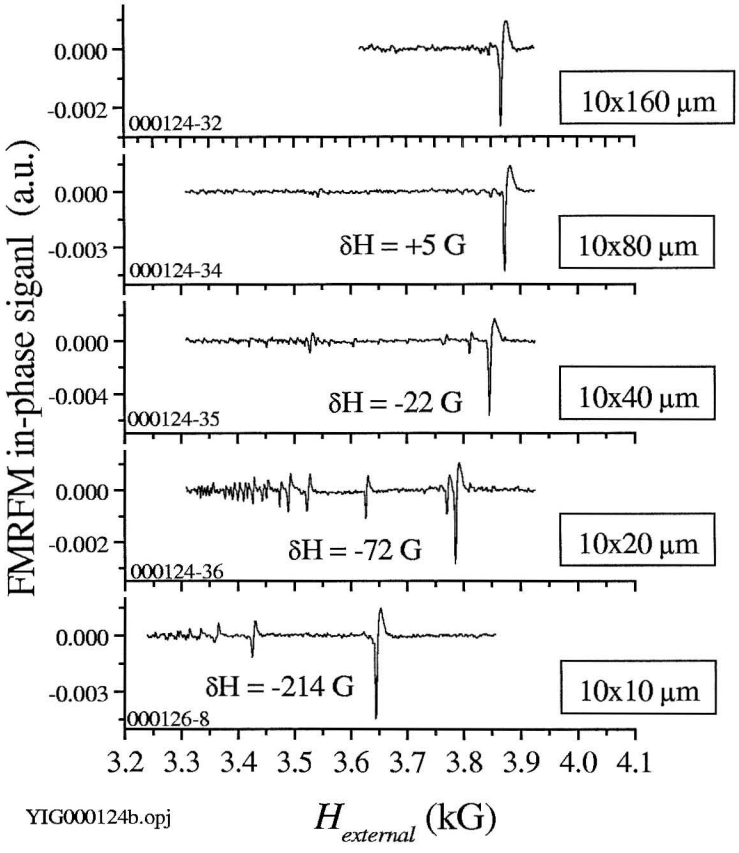

Figure 4.8: Same as for Figure 4.6, but for the $10\mu m$ series.

series, $H(L_0)$, is used as a reference point. The field difference δH is defined to be

$$\delta H = H(L_0) - H(L), \tag{4.3}$$

where $L_0 = 320\mu m$ and $L = 160, 80, 40, 20\mu m$ for the $20\mu m$ series, or $L_0 = 160\mu m$ and $L = 80, 40, 20, 10\mu m$ for the $10\mu m$ series.

The field differences, δH, of each series are shown in the inserts of Figures 4.7 and 4.9. The experimental differences correspond extremely well with the differences predicted by the dispersion relation (Eq. 4.2).

These FMR spectra were obtained with the magnetic NiFe tip of the cantilever $10\mu m$ above the sample surface. At this distance, the probe magnet produces a negligible additional local field at the sample (a few gauss). Consequently, perturbations from the

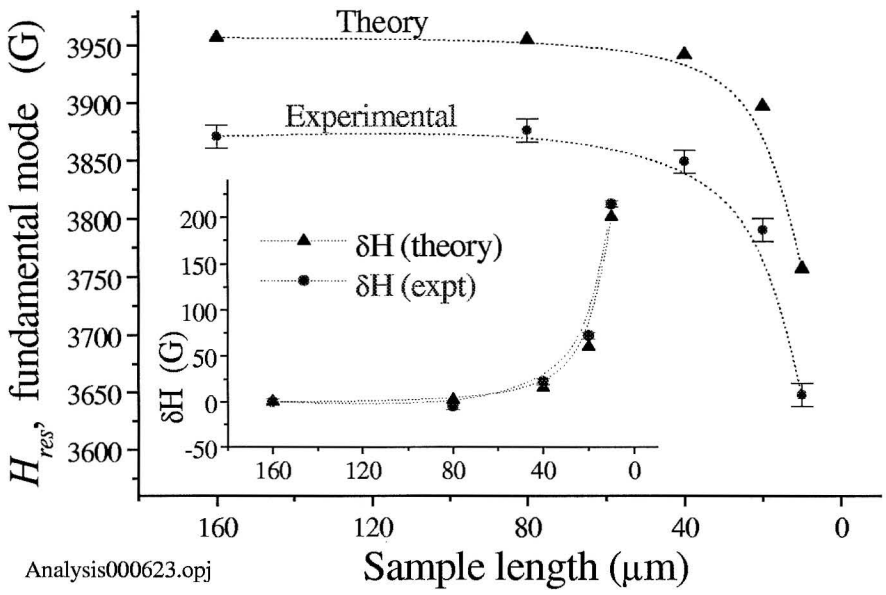

Figure 4.9: Same as for Figure 4.7, but for the $10\mu m$ series.

FMRFM technique to the dispersion relation were small, as is reflected by the samples closely following simple predictions.

4.1.4 Higher order modes

The magnetostatic modes for the samples shown in Figures 4.6 and 4.8 clearly show a dependence of the field separation between higher order modes upon the dimensions of the sample. For smaller structures, larger field separations are observed. The higher order modes also match theoretical calculations. Details of the magnetostatic mode spectrum for the sample having dimensions of $20\mu m \times 80\mu m$ are shown in Figure 4.10(a). The modes are identified by n_x, the number of half wavelengths along the sample's width, and by n_y, the number of half wavelengths along the sample's length. Comparison of the resonance field of the modes to theoretical calculations discussed below are shown in Figure 4.10(b). The two branches represent higher order modes along the width (where $n_x = 1, 3, 5...$, and $n_y = 1$) and higher order modes along the length (where $n_x = 1$, and $n_y = 1, 3, 5...$).

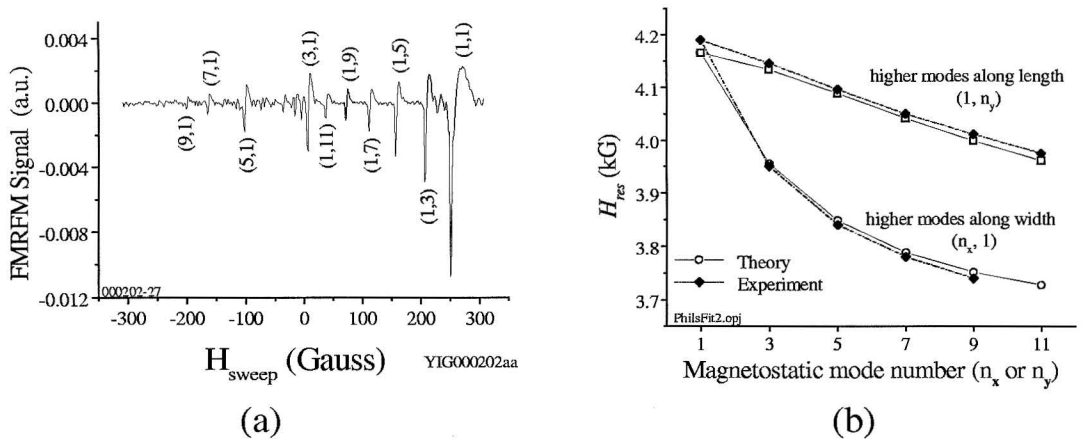

Figure 4.10: (a) A detailed spectrum of the $20 \times 80 \mu m$ sample showing the mode numbering (n_x, n_y). (b) The resonance field H_{res} of the fundamental and higher order modes of the $20 \times 80 \mu m$ sample. See text.

The expected fields of the fundamental and higher order modes were determined using an approximate dispersion relation developed by Kalinikos [32] (see Chapter 2). The approximation assumed that only the lowest order mode in the direction of the film thickness is excited ($n_z = 0$), and that the sample is infinite in the lateral dimensions. (Higher order modes along the thickness direction would have field separations due to exchange effects and would be separated by hundreds of gauss, well beyond the available sweep field. Thus, $n_z = 0$ is suitable for this study.) The dispersion relation is (Eqs. 2.38, 4.5)

$$\omega^2 = \omega_i \left[\omega_i + \omega_M \left(1 - \frac{1 - \exp\left(-k_t\ d\right)}{k_t\ d} \right) \right], \tag{4.4}$$

where d is the thickness of the film, $\omega_i = \gamma H_i$, $\omega_M = \gamma M_S$, and $H_i = H - H_d$. H_i is the internal field required to support the magnetostatic wave of the transverse wave number k_t. H_d is the demagnetization field at the center of the film when the magnetization is saturated normal to the plane of the film.

While this dispersion relation has been established for a laterally-infinite media as described in Chapter 2, it was applied here to approximate the dispersion relation for values of k_t that correspond to the allowed modes (k_x, k_y) of a microscopic structure. The transverse

wave number, k_t, is limited by the dimensions of the sample and has the discrete values

$$k_t = \left(k_x^2 + k_y^2\right)^{1/2} = \left(\frac{n_x^2\pi^2}{w^2} + \frac{n_y^2\pi^2}{L^2}\right), \tag{4.5}$$

where w is the width and L is the length of the sample. The dependence of the mode spacings upon the dimensions of the sample is now clearly evident in the dispersion relation.

The magnetostatic modes, shown in Figure 4.10, were calculated using the following parameters: $\frac{d}{w} = .17$, $4\pi M_S = 1760G$, $g = 2$ ($\gamma = 2.82$), $H_d = 1660G$, and $RF = 7.6GHz$. For the measured width of $18.5\mu m$, this requires the thickness to be $3.15\mu m$, which is within experimental error for layer thicknesses deposited by the LPE process. As a result of the ion milling process, the width of the sample is slightly less than the $20\mu m$ mask.

The calculated mode positions and the experimental observations, given in Figure 4.10, correspond extremely well. The correlation of the mode spacings with theory indicates that the probe magnet at this scan height does not have a large effect upon the dispersion relation. The field from the probe magnet may shift the resonance field or alter the field spacings between modes, but it does so only by an imperceptible amount.

4.1.5 Spatial resolution

The spatial resolution of FMRFM is demonstrated by the spectra observed for the $20\mu m \times 80\mu m$ film as it is scanned along the long axis of the sample, shown in Figure 4.11. The probe magnet is scanned approximately $5\mu m$ above the surface of the sample. The variance in the intensity of the modes as the magnetic NiFe-tip is moved along the long axis of the film is shown from the center to past the edge of the sample in Figure 4.12. The approximate spatial variation of the transverse magnetic moment (m_z) of the first few magnetostatic modes ($n_y = 1, 2, 3, ...$) are depicted in Figure 2.6 for reference.

The intensity of the fundamental mode is maximal in the center of the sample, and falls off in a fashion expected for the cosine dependence of a half wavelength over the length of the sample. For the first higher order mode ($n_x = 1, n_y = 3$), the amplitude should have a maxima at approximately $y = 0$ and $26\mu m$ and minima at approximately $y = 13$ and $40\mu m$

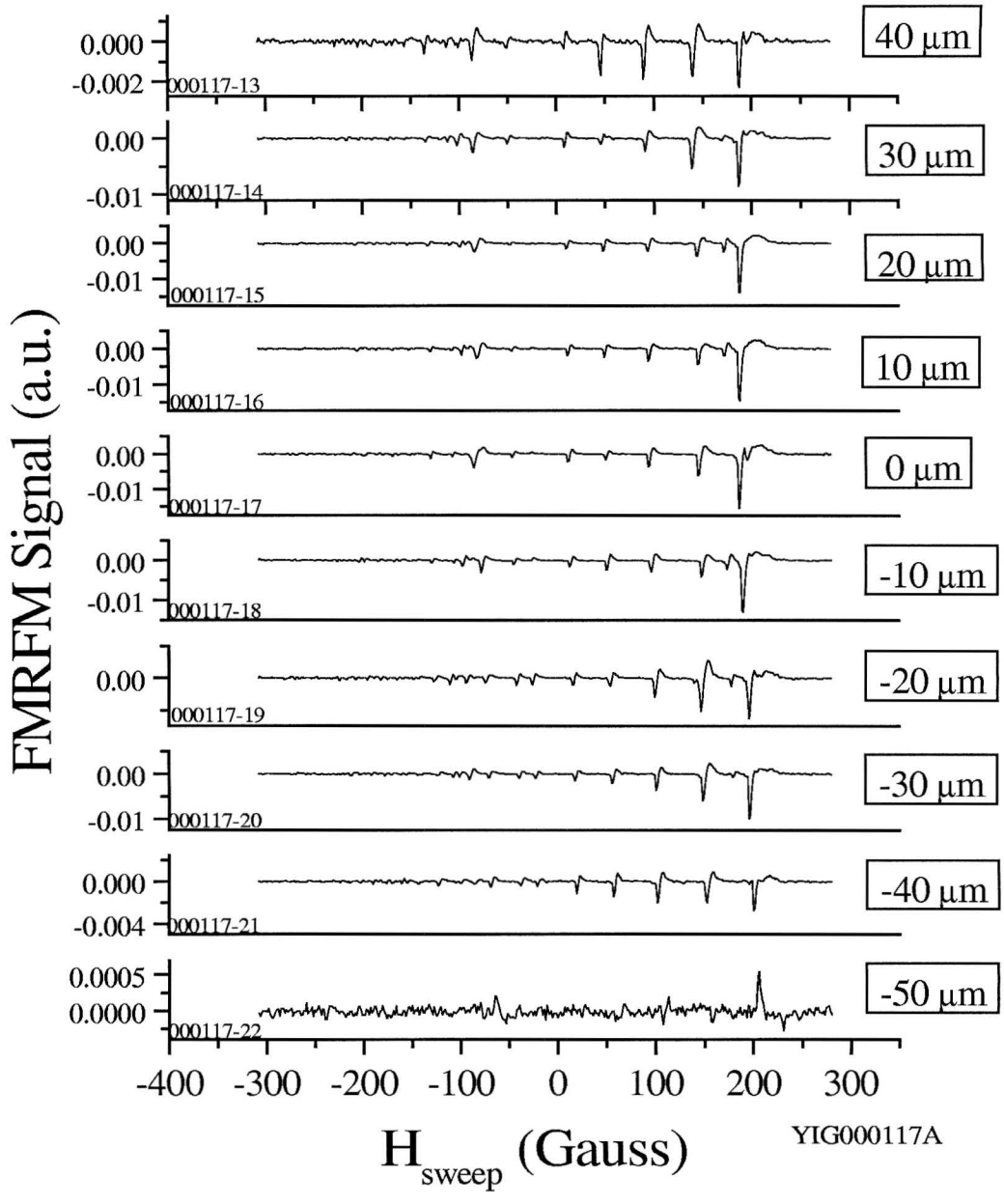

Figure 4.11: Spectra showing the amplitude variation as the magnetic tip is scanned along the length of the $20\mu m \times 80\mu m$ sample. Note the appearance of the "hidden" mode ($n_y = 2$) between the fundamental and the expected $n_y = 3$ modes.

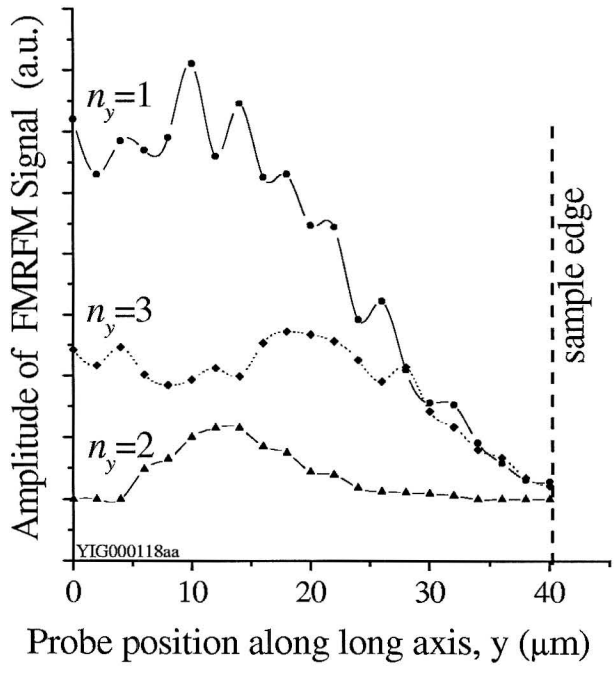

Figure 4.12: The amplitude of the resonance peaks of three different modes as a function of position along the length of the sample. The maximum and minimum of the signal amplitudes correspond to the sinusoidal spatial functions of the magnetic moment for each mode.

by simple geometry of a $n_y = 3$ mode. These were observed, as shown in Figures 4.11 and 4.12. The $n_y = 2$ mode will be discussed later.

For the $n_y = 3$ magnetostatic mode, which is approximated as a $\frac{3}{2}$ wavelength over the length of the sample, the transverse component of the magnetization should integrate to zero about the first node at $y = 13\mu m$. However, the probe magnet is sampling over a characteristic finite radius (the lateral resolution), which is determined by the dimensions and gradient field of the probe magnet. (i.e., the interaction of the probe magnet with the magnetic field of the sample falls off rapidly as the gradient field of the probe magnet decreases.) The FMRFM signal originates from the net moment of the magnetization in the z direction, which is non-zero on either side of the null. Thus, because the FMRFM signal is averaged over a finite area of the sample, a minimum rather than a null should be

observed in the signal intensity. This was indeed observed.

A lateral resolution of order $10\mu m$ can be determined by the variations of the $(n_x, n_y) = (1, 3)$ mode, shown in Figure 4.12. The expected maximum and minimum of the mode are clearly distinguishable. This resolution corresponds to the physical dimensions of the NiFe tipped cantilevers as expected.

A second very interesting feature of the $20\mu m \times 80\mu m$ spectrum is the excitation of a "hidden" mode, $n_y = 2$. In this experiment, the probe magnet was approximately $5\mu m$ above the sample surface and produced an additional field of $\sim 20G$ at the sample surface. This field is larger than that of the previous scans (a few gauss), which were obtained with the NiFe-tip $10\mu m$ above the sample. The field from the close proximity of the probe magnet breaks the symmetry of the field, which allows the hidden mode to couple more strongly to the RF field. This effect is discussed later in more detail in section "observation of a hidden mode." The observation of a hidden mode is among the first demonstrations of the probe magnet producing a local effect on the dispersion relation of a ferromagnetic sample.

4.1.6 Degenerate modes

For a perfect square sample, which has a length equal to width, there would be degenerate modes. For example, the resonance field for the $(n_x, n_y) = (1, 3)$ mode would be degenerate with the $(3, 1)$ mode. For the $20 \times 20\mu m$ sample, the difference in length and width is approximately $1\mu m$. This variation in dimensions, while not large, breaks the degeneracy and the two modes will resonate at slightly different fields H (approximately $5-10G$ apart).

In Figure 4.13, the spectra of the $20 \times 20\mu m$ sample is shown for $RF = 7.6GHz$, $P_{RF} = 10mW$, $H_{\text{mod}} \approx 3\,Gauss\,(35mV)$, and a tip to sample distance of $10\mu m$. Double peaks, corresponding to the slightly non-degenerate modes $(1, 3)$ and $(3, 1)$, were observed. When the probe magnet is at the center of the sample, the modes have comparable amplitudes. as expected. As the magnetic NiFe-tip is scanned to the sample edge along the x direction,

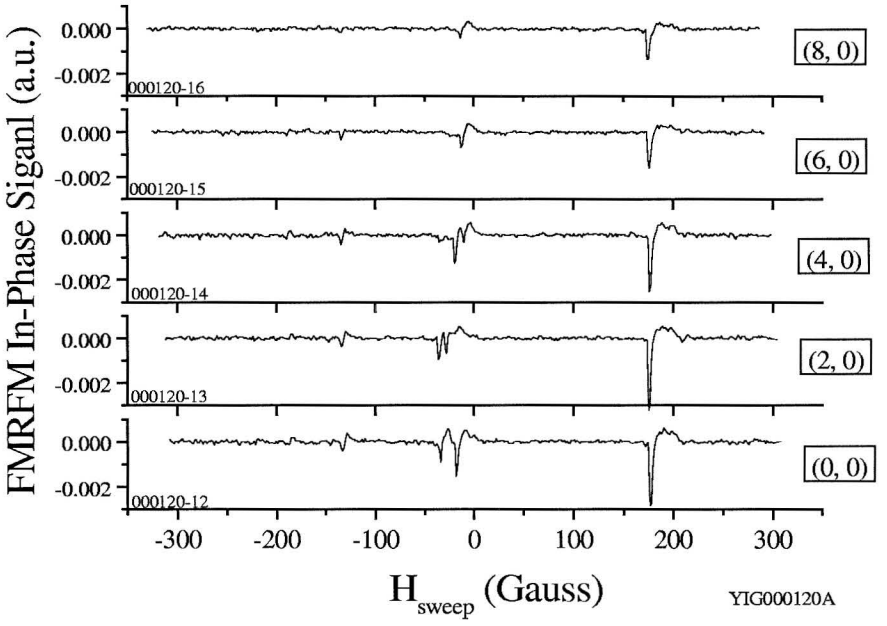

Figure 4.13: Spectra of the $20 \times 20\mu m$ sample, scanned from the center to the edge along the x axis. The double peaks correspond to the $\left(\frac{1}{2}, \frac{3}{2}\right)$ and $\left(\frac{3}{2}, \frac{1}{2}\right)$ modes. The degeneracy is "broken" by the $1\mu m$ difference between the length and the width of the sample.

both amplitudes decrease as expected. However, one mode is observed to dominate as the cantilever is moved off-center. Further measurements of this sample revealed that the observation of the double peaks was highly dependent upon the position of the cantilever with respect to the sample. A simple breaking of the degeneracy due to variations in the sample dimensions may not be the only factor.

4.1.7 Phase sensitivity

The FMRFM measurement utilizes a lock-in, at the cantilever frequency, to measure the amplitude of the FMR signal. The signal has a relative phase associated with it, which corresponds to the vector direction of the field produced by the oscillating magnetic moments in the sample. By measuring the relative phase as a function of position, the vector component of the oscillating magnetization in the sample is observed.

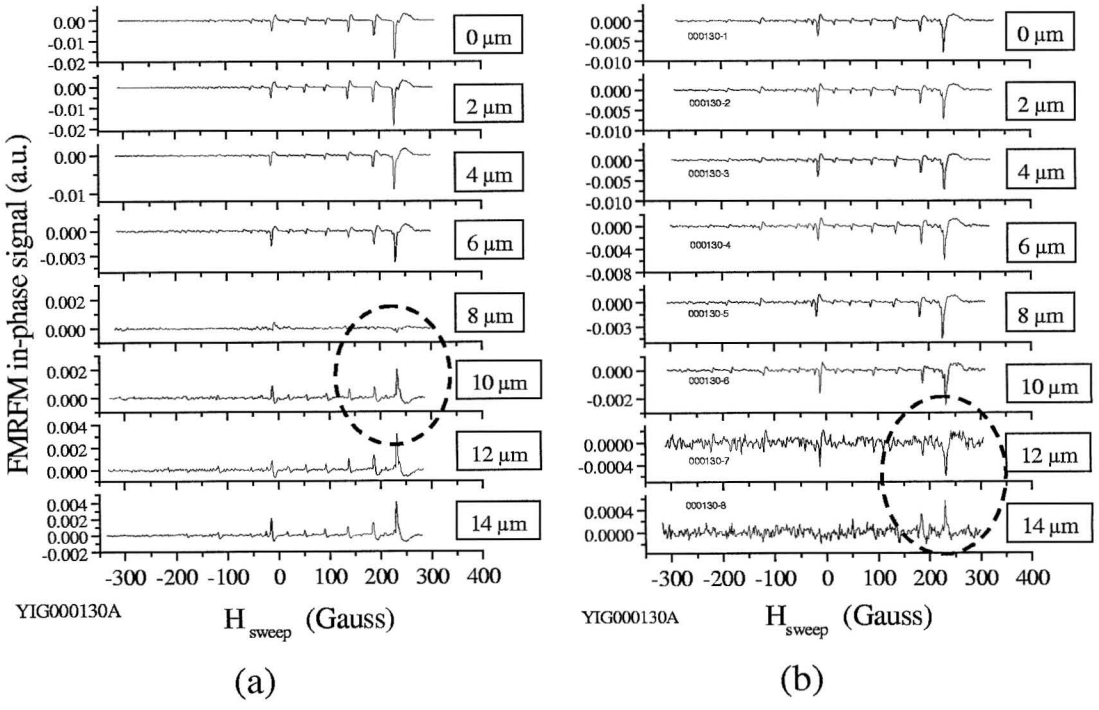

Figure 4.14: Spectra showing the phase sensitivity of FMRFM on the $20\mu m \times 80\mu m$ sample. (a) Scan from the center to the edge along the width of the sample, with a tip to sample height of $2\mu m$. (b) Same as (a), but with a tip to sample height of $10\mu m$. The phase flip of each scan is indicated by a dashed circle.

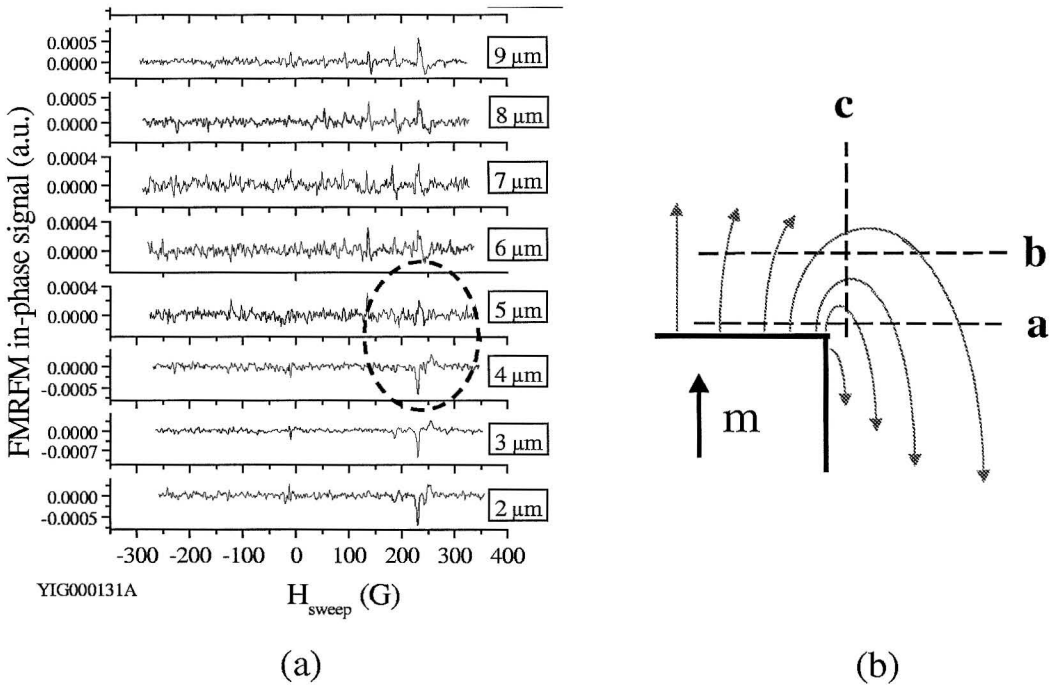

Figure 4.15: Spectra showing the phase sensitivity of FMRFM on the $20\mu m \times 80\mu m$ sample. (a) At the edge of the sample, the cantilever is raised from a height of $2\mu m$ to a height of $10\mu m$. (b) Cartoon showing scan paths across the sample width at heights of $2\mu m$ and $10\mu m$ (Fig. 4.14), and from the sample edge. The magnetic fields due to the sample's oscillating magnetization is shown for reference. The phase flip in each scan is indicated by a dashed circle.

The relative phase of the signal was determined for scans along three different paths of the $20\mu m \times 80\mu m$ sample, as shown in the cartoon Figure 4.15(b). The probe magnet was scanned along the width (x-axis), from the center to the edge of the film, at a height of $2\mu m$ and $10\mu m$ above the sample surface respectively (Fig. 4.14(a), (b)). As expected, the intensity of the modes are observed to decrease to zero at the edge of the sample. However, the relative phase of the modes flip 180° as the probe magnet is moved beyond the edge of the sample. The flip in the relative phase of the $10\mu m$ scan occurred $2\mu m$ further from the edge of the sample than the $2\mu m$ scan. This is indicated by the dashed circles in Figure 4.14. The corresponding vector components of the oscillating magnetization are shown as paths **a** and **b** in Figure 4.15(b). The relative phase flip of path **b** occurs further from the sample edge than path **a**, as was observed.

The probe magnet was then placed at the edge of the film at $x = 11\mu m$, between the x positions in which the relative phase was observed to change for paths **a** and **b**. The probe magnet was raised from the surface in $1\mu m$ steps, from $2\mu m$ to $10\mu m$, as shown as path **c**. The relative phase was expected to change between the heights of $2\mu m$ and $10\mu m$, corresponding to the relative phase flips obtained in paths **a** and **b**. This was indeed observed, at the height of 4-5μm, and shown in Figure 4.15(a). The FMRFM demonstrated a sensitivity to the relative phase of the vector component of the oscillating magnetization with a lateral resolution of $2\mu m$.

4.2 Effect of probe magnet on the dispersion relation

The probe magnet, which enables measurement of the local spatial variations in the FMR response within a sample, can also perturb the dispersion relation. In FMRFM, the probe magnet does not, in general, define a "sensitive slice" as it does in EPR or NMR MRFM. In the case of EPR and NMR, the gradient field of the probe magnet and the line width of the sample serve to create a resonant volume within the sample, termed the "sensitive slice," where the magnetic field satisfies the dispersion relation. Only spins within this localized volume are excited into resonance. In FMRFM, the dispersion relation and excitation of the spins is *not* defined locally because of the strong ferromagnetic coupling. But it may be detected by a *local* interaction with a probe magnet that is smaller than the sample. This *interaction volume* (i.e., the region most strongly affected by the local gradient field) determines the spatial resolution in the previous section (in which the low field from the probe magnet only weakly perturbs the dispersion relation).

In this section, the possible effects on the dispersion relation that result from "turning up" the field strength of the probe magnet are explored. There are various other sources of local perturbation which may affect the dispersion relation, such as thermal fluctuations or field inhomogeneities. Additionally, the field from the probe magnet may affect the dispersion relation over a small volume of the sample by breaking the symmetry of the field, and thereby alter the RF absorption (and signal intensity) of certain modes. In this study the first observations of what appears to be a probe-magnet-induced local perturbation on the dispersion relation are presented.

The close proximity of the probe magnet to the sample introduces a spatial inhomogeneity to the local field, $H \rightarrow H + \delta H$. The probe magnet can produce $\delta H \approx 40 - 100\,G$ near the surface of the sample in the region just below the probe when the NiFe tip is $5 - 2\mu m$ above the sample surface. Two possibilities of how the inhomogeneous field can affect the dispersion relation were discussed at the end of Chapter 2. However, this study finds neither a simple shift of the resonance fields nor any change in field spacing larger than

the experimental uncertainties. Instead, the RF absorption of particular modes appear to be affected due to a local perturbation of the dispersion relation. The probe magnet appears to induce three significant effects at close proximity ($2 - 5\mu m$): the observation of a "hidden" mode, the suppression of the fundamental mode, and the enhancement of higher order modes. The effects of the probe magnet on the dispersion relation are explored. These effects are vital to understanding how "spatial resolution" can be obtained in a ferromagnetically coupled sample via FMRFM.

4.2.1 Observation of a "hidden" mode

In order to observe a magnetostatic mode, its time-varying magnetization $m(r,t)$ must have a net moment along the orientation of the RF field [19]. The intensity of the RF absorption in a uniform RF field $\vec{H}_{RF}$, as described in Chapter 2, is

$$\langle \vec{m} \cdot \vec{H}_{RF} \rangle = \left\{ \frac{l_y A}{n_y \pi} \left[Z^i(z) \right]_{-d/2}^{d/2} + B \int_{-d/2}^{d/2} Z^i(z)\, dz \right\} \sin\left(\frac{n_y \pi}{2}\right) \frac{l_x}{n_x \pi} \sin\left(\frac{n_x \pi}{2}\right) \qquad (4.6)$$

where A and B are functions of ω, H_i, M_S, and H_{RF}; and $\vec{m}$ is the RF component of the magnetization. From this equation, it can be seen that there is a selection rule that no absorption should occur for any mode with either n_x or n_y an even integer. These are termed "hidden" modes.

In an *ideal* sample in a *uniform* field, the spatially antisymmetric hidden modes should have zero amplitude. However, thermal fluctuations, imperfections in the sample, and non-uniformities in the external fields may result in a small net moment of the magnetization in these modes. ("Net moment" refers to the spatial average over the entire sample.) Thus, hidden modes will couple to the RF field only weakly, and are therefore usually not detected. However, in our experiments where the probe magnet is brought close to the sample surface, the hidden mode $(n_x, n_y = 2, 2)$ emerged from the background noise. Its amplitude variation across the sample length is shown in Figures 4.11 and 4.12.

There are two possible mechanisms that could result in the detection of a hidden mode: the "shorting out" of the RF field and the local perturbation of the dispersion relation.

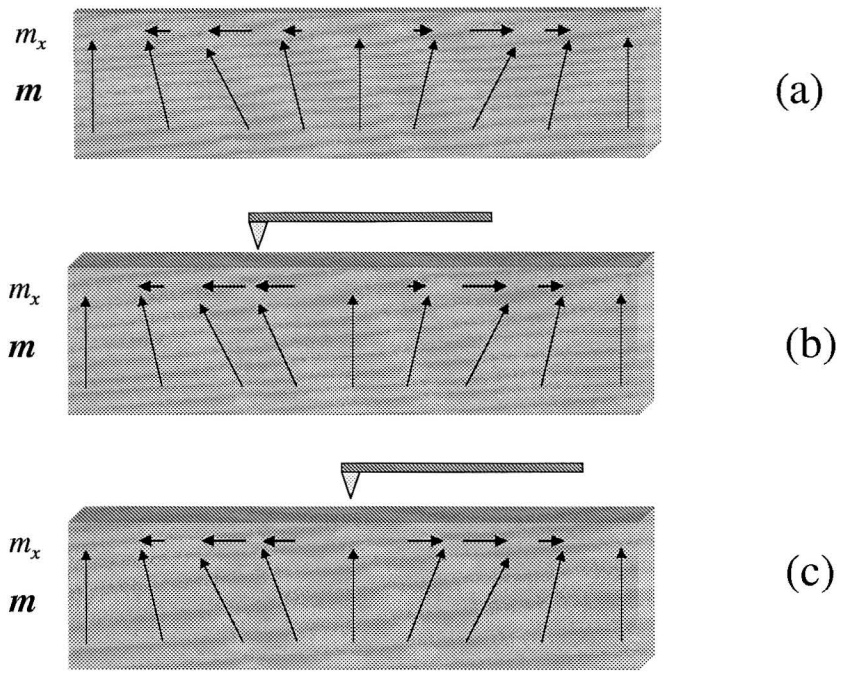

Figure 4.16: The $n_y = 2$ "hidden" mode which is not excited in a uniform field. (a) The mode shape in absence of any perturbation is antisymmetric about $y = 0$. (b) The mode perturbed by a probe magnet placed off sample center. (c) The mode shape perturbed by the probe magnet at exactly the sample center.

The probe magnet, which is metallic, could create a local nonuniformity in the RF field (i.e., "short out" the RF field over a small region). However, this effect should have similar effects upon all of the modes. This appears to be contrary to our observations of perturbations on *particular* modes. Furthermore, in the following sections a simple model is introduced, based upon local perturbation of the dispersion relation, which seems to qualitatively account for most of these observations. The remainder of this section will focus on this simple model, although the possibility of the "shorting out" of the RF field should be studied further in future experiments.

The field from the probe magnet is capable of locally perturbing the dispersion relation, introducing an additional non-zero net RF magnetization within the sample, which increases the signal intensity. A schematic depiction of this possibility is shown in Figure 4.16. For

a hidden mode in an ideal sample immersed in a uniform field (Fig. 4.16(a)), the RF component of the magnetization in the x direction, m_x, has zero net moment. The probe magnet, which can produce fields of order $\sim 40 - 50\,Gauss$ at the sample surface when located $5\mu m$ above it, can alter the magnetostatic modes of the sample. In this case, the magnetization m_x for antisymmetric modes can have a net moment greater than zero (Fig. 4.16(b)). This results in non-zero coupling of the mode to the RF field, and can thus produce a signal intensity large enough to be detected. Note that exactly at the center of the sample ($y = 0$), the perturbation of the antisymmetric mode is itself symmetric and thus ineffectual at inducing coupling to the RF field (Fig. 4.16(c)). Therefore, at this unique position, the intensity of the $n_y = 2$ mode should not be altered. This lack of increased excitation of the hidden mode with the probe magnet at $y = 0$ was verified experimentally, as shown in Figures 4.11 and 4.12.

4.2.2 Effect on the fundamental and higher order modes

The probe magnet, when brought to within $3 - 5\mu m$ of the sample surface, imposes a field of order $\sim 60G$ at the sample. When the probe magnet is centered above the $20 \times 160\mu m$ sample, the magnetostatic modes are visibly affected in two ways. The intensity of the fundamental mode is suppressed, while simultaneously the intensities of certain higher order modes become enhanced. These effects are both shown in Figure 4.17, and in more detail in Figure 4.18. We believe these results may represent the first demonstration of a direct, local alteration of the dispersion relation within a ferromagnetic sample. The observed effects of the probe magnet on the ferromagnetic modes can be modeled with a simple theoretical picture described below. This has been developed in collaboration with Dr. Wei Chen and Prof. Michael Cross. (Development of a more sophisticated model is currently in progress.)

Simple theoretical model

In paramagnetic resonance, the external field H and the RF frequency ω, are simply related by the dispersion relation. A modification in H results directly in a change in ω. However,

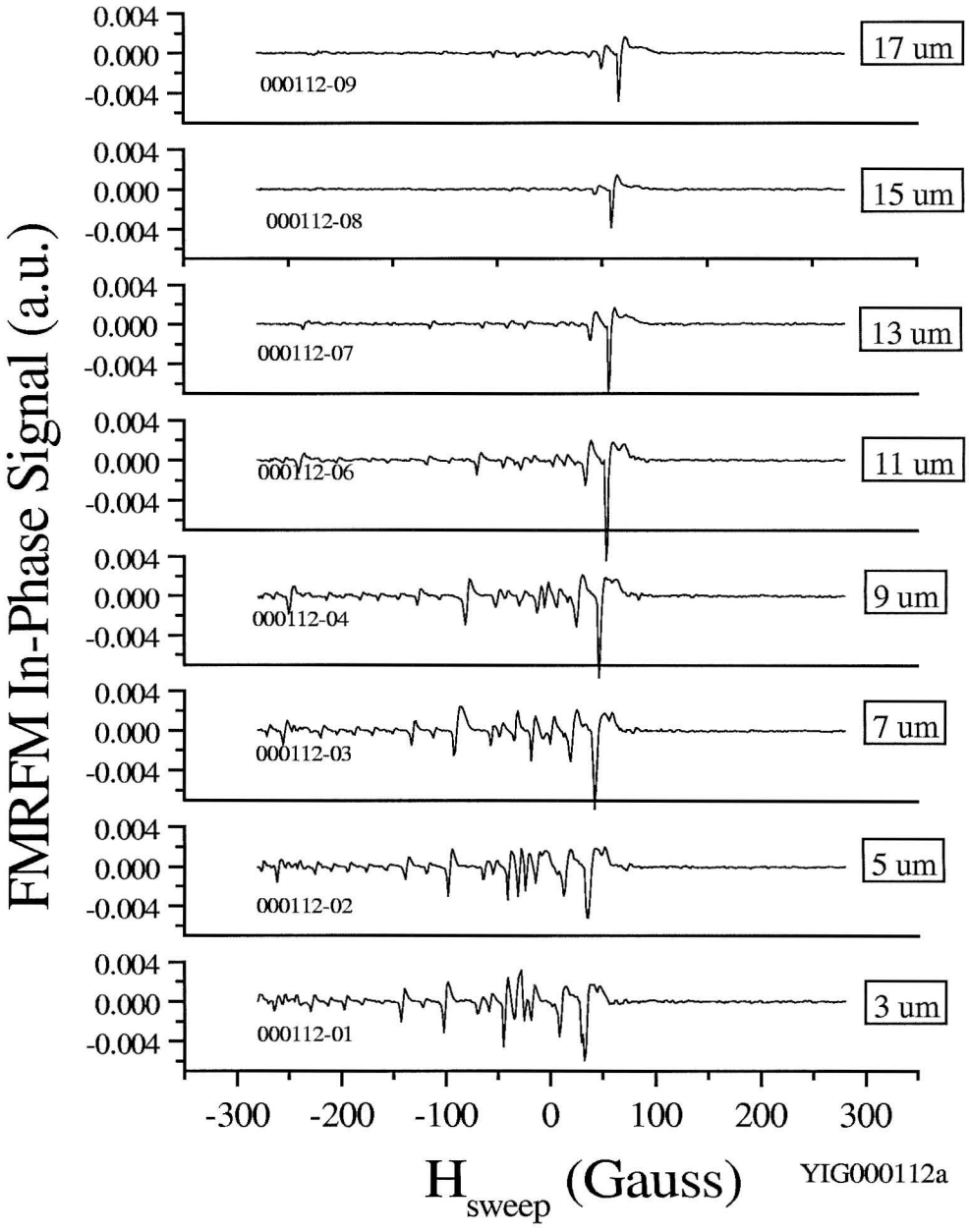

Figure 4.17: Spectra of the $20\times160\mu m$ sample as the probe magnet, a NiFe coated ultrasharp tip on a commercial cantilever, is brought close to the sample surface in $2\mu m$ steps. When the tip is $3-5\mu m$ above the surface, the effect on several of the higher order modes is observed. The constant drift is due to thermal expansion in the apparatus.

in ferromagnetic resonance, there is an additional variable – the wavenumber of the mode k – which determines the resonance condition. In this particular experiment, the probe magnet was brought closer to the sample surface, increasing the spatial variation of the external field in a localized region. The external field H and the RF field remained relatively constant over the majority of the sample. Thus, in order to satisfy the dispersion relation over the entire sample, it is theorized that the wave number k varies within the interaction region perturbed by the field from the probe magnet. Their effect has not yet been modeled in detail directly. However, the simple model described here qualitatively accounts for the observed effects by providing an approximate ratio of the signal intensities for the modes with and without the perturbing field.

Our approach to modeling the perturbing effect of the probe magnet is to seek a magnetostatic mode which satisfies the experimental conditions. This mode (a) exists in the presence of an inhomogeneous field $H + \delta H$ over a localized region of the sample, (b) is characterized by a resonance frequency ω everywhere in the sample, and (c) has overall boundary conditions determined by the finite dimensions of the sample. The magnetostatic mode of the entire sample is modeled following the theories of DE [24], Storey [29], and Kalinikos [32]. The following approximations of the above conditions are made to simplify the calculations. (A possible physical interpretation of the approximations are illustrated in Figure 4.20.)

1. The internal field H_i is modeled as existing over the length of the sample L, falling to zero abruptly outside this region since $\vec{m} = 0$ outside of the sample. The sample in which the perturbation of the mode intensities were observed has $L = 160\mu m$.

2. The gradient field from the probe magnet increases the external field in its vicinity, $H \rightarrow H + \delta H$. This perturbing field, δH, is modeled as constant field over a length l, falling to zero abruptly outside this region. The characteristic length scale of the interaction volume, l, will be assumed to be on order of the observed spatial resolution ($\sim 20\mu m$). The square shape, while unphysical, allows us to apply the methods of DE theory, and to draw qualitative, but crucial, insights.

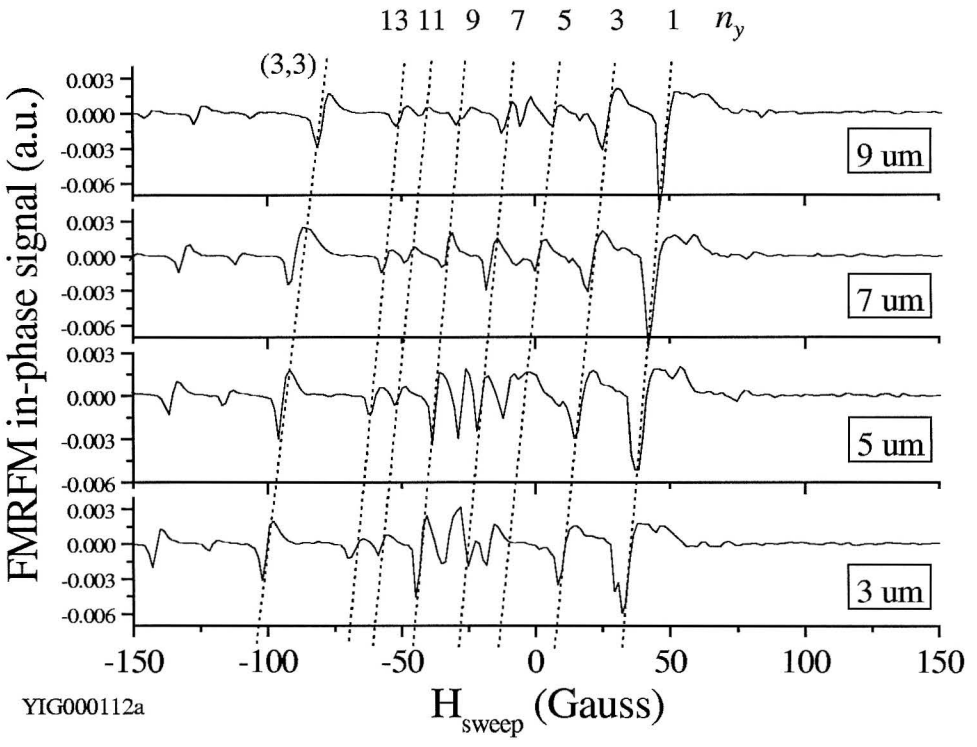

Figure 4.18: Enlargement of the spectra of the $20 \times 160 \mu m$ sample from Figure 4.17. The intensities of several higher order modes are affected while the fundamental mode is supressed. The wavenumbers of the modes along length, $n_y = 1, 3, 5, ...$, are indicated.

3. We assume only the uniform modes are excited in the z and x directions (i.e., set $k_z = k_x = 0$) , similar to the approximation made by Kalinikos ($k_z = 0$) [32]. This is motivated by the observations that only higher order modes corresponding to the sample length ($k_y = \frac{n_y \pi}{L}$) appear to be significantly perturbed by the probe magnet. Furthermore, this assumption will allow the boundary conditions to be satisfied simply.

Calculating the magnetic potential

The magnetic potential satisfying this field profile are adapted from DE theory and utilize the approximations listed above. In the theory of DE, the magnetic potential was derived

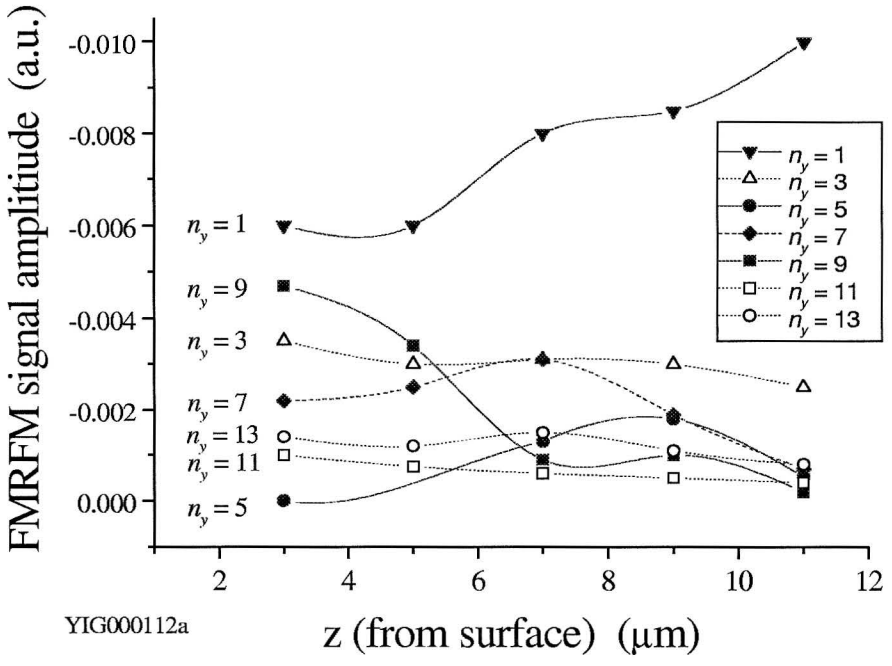

Figure 4.19: The signal intensities of the modes of the $20 \times 160 \mu m$ YIG sample. The wavenumbers of the modes $n_y = 1, 3, 5, ...$ are indicated.

from Maxwell's equation in the following manner. The condition $\vec{\nabla} \times \vec{h} = 0$ allows the introduction of a magnetic potential Ψ, where $\vec{h} = \nabla\Psi$. The internal magnetic potential is (from Chapter 2, Eq. 2.30)

$$\Psi^i(x,y,z) = X(x)Y(y)Z^i(z) = e^{ik_x x}e^{ik_y y}\left(a\sin(k_z^i z) + b\cos(k_z^i z)\right), \tag{4.7}$$

where k_i is the wavenumber and a and b are constants determined by the boundary conditions. Using the Kalinikos approximation, $k_z = k_x = 0$, the magnetic potential for the modes of an unperturbed sample are approximated as

$$\Psi = A\cos k_y(\frac{L}{2} + y), \tag{4.8}$$

where $k_y = \frac{n_y\pi}{L}$ is determined by the dimension of the sample. The form of Ψ was chosen to ensure that the magnetization at the ends of the sample was zero. i.e., the boundary condition $m\Big|_{y=\pm\frac{L}{2}} = 0$ is satisfied. For reference, Ψ simplifies to $\Psi = A\sin(\frac{n_x\pi}{L}y)$ for $k_y = \frac{n_y\pi}{L}$.

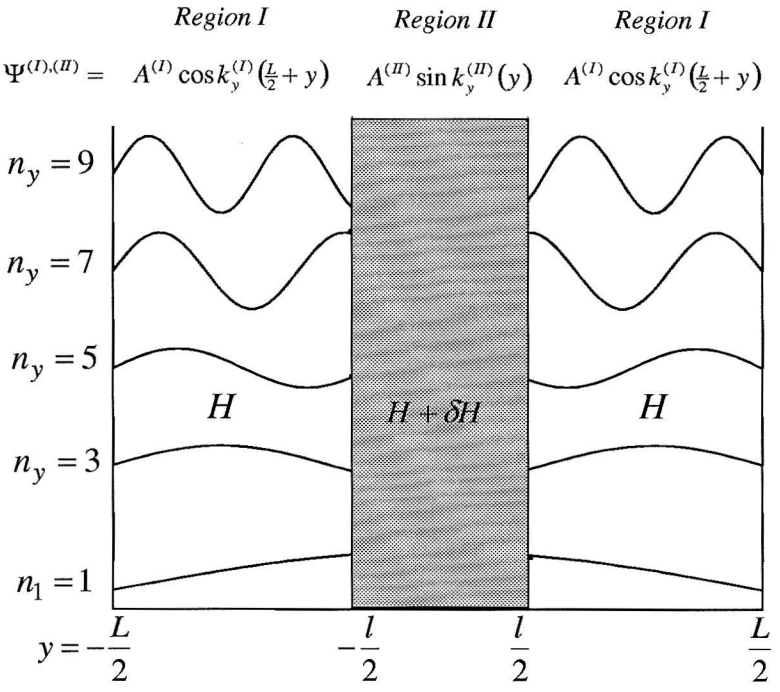

Figure 4.20: The field profile assumed for a sample with length L in an external field H, and a pictorial representation of the magnetiostatic modes. The field from the probe magnet is modeled as having a characterstic length l and field δH. This adds to the uniform ambient field, H. The modes and their possible modifications are depicted for $k_y^{(I)} = k_y$, and $k_y^{(II)} < k_y$. Here the regions (I, II) are indicated for the case of finite δH.

The probe magnet is assumed to induce a small, but finite, perturbation upon the sample, and thus will have a negligible effect on regions outside the interaction volume. This assumption is supported by two observations: (a) the field of the probe magnet ($\sim 60G$) is small compared to the external field ($\sim 4200G$) and (b) the resonance field positions of the perturbed sample correspond fairly well to the values predicted by the low field limit, in which the probe magnet only weakly perturbed the dispersion relation (section 4.1). Therefore, the magnetic potentials of the regions outside and inside of the perturbed interaction volume (regions I and II, respectively) are approximated to have similar forms as the unperturbed sample (Fig. 4.20). These are:

$$\begin{aligned}
\Psi^{(I)} &= A^{(I)} \cos k_y^{(I)}(\frac{L}{2}+y) \qquad \text{for} -\frac{L}{2} < y < -\frac{l}{2} \\
\Psi^{(II)} &= A^{(II)} \sin k_y^{(II)} y \qquad\qquad \text{for} \quad -\frac{l}{2} < y < \frac{l}{2} \\
\Psi^{(I)} &= A^{(I)} \cos k_y^{(I)}(\frac{L}{2}+y) \qquad \text{for} \quad \frac{l}{2} < y < \frac{L}{2}
\end{aligned} \tag{4.9}$$

where $A^{(I)}$ and $A^{(II)}$ are coefficients to be determined by the boundary conditions. Here the variable $\Psi^{(I)}, \Psi^{(II)}, k_y^{(I)}, k_y^{(II)}, A^{(I)}$ and $A^{(II)}$ refer to the perturbed sample case where $\delta H \neq 0$. The values and Ψ, k_y, and A refer to the unperturbed sample case where $\delta H = 0$.

Maxwell's equation, $\vec{\nabla} \times \vec{h} = 0$, requires that the magnetic field, $b_y = h_y + 4\pi m_y = (1+\chi)\frac{\partial \Psi}{\partial y}$, is continuous across the boundaries at $y = \frac{l}{2}$, -$\frac{l}{2}$. This boundary condition was also applied in DE theory to determine coefficients of the magnetic potential inside and outside of the sample [17]. Since we have made approximations similar to those of Kalinikos, $k_z = k_x = 0$, the magnetic potentials in the x and z directions are constant, and the boundary conditions are automatically satisfied.

For the derivative in the y direction (along the sample length), a relationship between the coefficients$A^{(I)}$ and $A^{(II)}$ is determined:

$$(1+\chi^{(II)})A^{(II)}k_y^{(II)} \cos\frac{k_y^{(II)}l}{2} = (1+\chi^{(I)})A^{(I)}k_y^{(I)} \sin k_y^{(I)}(\frac{L}{2}-\frac{l}{2}). \tag{4.10}$$

$k_y^{(I)}$ and $k_y^{(II)}$ are the wavenumbers of the dispersion relation outside and inside the interaction volume (for the case of a perturbing gradient field), and have not been fixed by the boundary conditions. $\chi^{(I)}$ and $\chi^{(II)}$ are the susceptibility in each region. For thin ($d << L$) ferromagnetic materials, the susceptibility determined by DE theory yields $\chi \approx -\frac{2}{k_y d} >> 1$ (for small values of k_y). Thus, the relation of the coefficients may be further approximated as

$$\frac{A^{(I)}}{A^{(II)}} \approx \frac{\chi^{(II)}k_y^{(II)} \cos\left(k_y^{(II)}\frac{l}{2}\right)}{\chi^{(I)}k_y^{(I)} \sin\left(k_y^{(I)}(\frac{L}{2}-\frac{l}{2})\right)} = \frac{\cos\left(k_y^{(II)}\frac{l}{2}\right)}{\sin\left(k_y^{(I)}(\frac{L}{2}-\frac{l}{2})\right)}. \tag{4.11}$$

The wavenumbers $k_y^{(I)}$ and $k_y^{(II)}$ can be related through the dispersion relation because ω is constant — FRMFM excites with a uniform driving field over the entire sample. This

relation is derived in the next section. This leaves two unknowns, $A^{(II)}$ and $k_y^{(I)}$, but only one equation. We obtain the extra requisite information in the following way. The resonance fields for the modes in the perturbed sample correspond approximately to those observed in a uniform external field. In the simple theory derived for YIG microstructures in a uniform field (Chapter 2), the wavenumbers are determined by the sample dimensions, $k_y = \frac{n_y \pi}{L}$. In the present case, within our model the majority of the perturbed sample is located in a uniform field. Thus, we assume that the wavenumbers in the regions outside of the interaction volume are approximately the same as that for the sample unaffected by the local gradient field. i.e., we assume $k_y^{(I)} \approx k_y$.

Determining $k_y^{(II)}$

A relationship between the wavenumber $k_y^{(II)}$and $k_y^{(I)}$ can be derived from the dispersion relation. From the theory of Kalinikos [32], the approximate dispersion relation is (for $k_z = 0$)

$$\omega^2 = \omega_i \left[\omega_i + \omega_M \left(1 - \frac{1 - \exp\left(-k_t\ d\right)}{k_t\ d} \right) \right], \tag{4.12}$$

where $k_t = \left(k_x^2 + k_y^2\right)^{1/2} = \left(\frac{n_x^2 \pi^2}{w^2} + \frac{n_y^2 \pi^2}{L^2} \right)^{1/2}$, $\omega_i = \gamma\left(H + H_d\right)$, $\omega_M = \gamma(4\pi M_S)$, and w, L, and d are the width, length and thickness of the sample. For this simple model, in which $k_x = 0$ is assumed, the transverse wave number reduces to $k_t = k_y^{(I)} = \frac{n_y \pi}{L}$.

For a sample with length much greater than thickness ($L >> d$), the exponential in the dispersion relation (Eq. 4.12) may be expanded to obtain

$$\omega^2 \approx \gamma H_i \left[\gamma H_i + \gamma(4\pi M_S) \frac{k_y d}{2} \right]. \tag{4.13}$$

The RF frequency, ω, is constant, hence, (Eq. 4.13) indicates that a small increase in the external field ($H \rightarrow H + \delta H$) will yield a decrease in the wave number ($k_y^{(I)} \rightarrow k_y^{(I)} - |\delta k|$). This indicates that the wavenumber of the region inside the interaction volume is less than the wavenumber of the regions outside the interaction volume: $k_y^{(II)} = (k_y^{(I)} - |\delta k|) < k_y^{(I)}$. To approximate the magnitude of the change in the wavenumber, we take the derivative of

Eq. 4.13, which yields the relation

$$0 = \gamma^2 \left(2H_i\ \delta H_i\right) + \gamma^2 \left(\delta H_i 4\pi M_S \frac{k_y d}{2} + H_i 4\pi M_S \frac{\delta k_y\, d}{2} \right). \tag{4.14}$$

For the $20 \times 160 \mu m$ YIG sample, the internal field H_i is of order $2500\,G$ while the increase in the field δH_i is only of order $\sim 60\,G$. Also, $\frac{k_y d}{2} << 1$ for the first few modes. Thus, the second term in Eq. 4.14 is much smaller than the first term, and is therefore neglected. The approximate change in the wavenumber is

$$\delta k = \frac{\delta H}{(4\pi M_S)} \frac{4}{d}. \tag{4.15}$$

For the experimental conditions, $\delta H = 60\,G$, $4\pi M_S = 1760\,G$, and $d = 3\mu m$, Eq. 4.15 yields a shift in the wavenumber of $\delta k \approx \frac{1}{22\mu m}$.

In the approximation for δk, we have derived the change in the wavenumber for low order modes, and, furthermore assumed that it is the same for all modes. This approximation will be justified by two observations resulting from this simple theory. First, only *particular* higher order modes exhibit significant effects from the probe magnet. These will be primarily determined by the ratio of the characteristic lengths, $\frac{L}{l}$, and not by the strength of the additional field (within the assumed weak perturbation limit). Second, the effect of the probe magnet on the fundamental mode $n_y = 1$ directly depends on the strength of the additional field. The derivation of δk (Eq. 4.14), which assumed low order modes (see discussion leading to Eq. 4.15), yields the most reliable approximation for $n_y = 1$.

Effect on signal intensity

An increase in the signal intensity of certain higher order modes (n_y) is observed in the FMRFM data (Fig. 4.18). The absolute magnitude of the increase cannot be determined by our simple model. However, the *relative* intensity of the modes within the perturbed and unperturbed samples may be approximately derived. We consider only the relative intensities within the interaction volume, which is the region generating a force upon the mechanical resonator.

The signal intensity is proportional to the component of the RF magnetization in the thickness (z) direction, m_z. Thus, to compare the relative signal intensities, the term $m_x^2 \cdot \vec{H}_{RF}$ is integrated over the sample volume (whereas RF absorption is simply $< m_x \cdot \vec{H}_{RF} >$). The intensity of the signal from an unperturbed sample over the interaction region $-\frac{l}{2} < x < \frac{l}{2}$ is

$$I \propto \int_{-l/2}^{l/2} (A^{(I)} \cos k_y^{(I)} y)^2 \, dy = (A^{(I)})^2 \left(\frac{l}{2} + \frac{1}{2k_y^{(I)}} \sin 2\alpha \right) \tag{4.16}$$

where α is defined as $\alpha = \frac{k_y^{(I)} l}{2}$. Similarly, the signal intensity from a perturbed sample generated from the interaction region is

$$I^{(II)} \propto (A^{(II)})^2 \left(\frac{l}{2} + \frac{1}{2k_y^{(II)}} \sin 2\alpha' \right) \tag{4.17}$$

where α' is defined as $\alpha' = \frac{k_y^{(II)} l}{2}$ (the prime denotes the perturbed case). Using the relation of the coefficients from Eq. 4.10 and the approximation $k_y^{(I)} \approx k_y$, the relative intensities as a function of k_y is

$$\frac{I^{(II)}}{I} \approx \left(\frac{\sin^2 \left(\frac{k_y L}{2} - \alpha \right)}{\cos^2 \alpha'} \right) \left(\frac{\frac{l}{2} + \frac{1}{2k_y^{(II)}} \sin 2\alpha'}{\frac{l}{2} + \frac{1}{2k_y} \sin 2\alpha} \right). \tag{4.18}$$

The relative intensities of the signals ($I^{(II)}/I$) as a function of α are shown in Figure ??(b). The modes $n_y = 1, 3, 5, ...$ are denoted, and the wavevectors for the perturbed sample, $k_y^{(II)}$, were calculated from Eq. 4.15. The relative intensities exhibits significant changes for those modes where $\alpha = \frac{k_y l}{2} \approx m\frac{\pi}{2}$, where $m = 1, 3, 5, ...$ By contrast, the relative signal intensities change only slightly for the lowest order modes, such as $n_y = 3$.

From this simple picture it is clear that the modes closest to $\alpha = \frac{k_y l}{2} \approx m\frac{\pi}{2}$ should exhibit the most significant changes in intensity when the probe magnet is brought near the sample surface. These modes can be interpreted as those closest to fitting an integral number of half wavelengths within the interaction region, $-\frac{l}{2} < y < \frac{l}{2}$.

For the $20 \times 160 \mu m$ sample with a characteristic length of $l = 20 \mu m$, the condition for

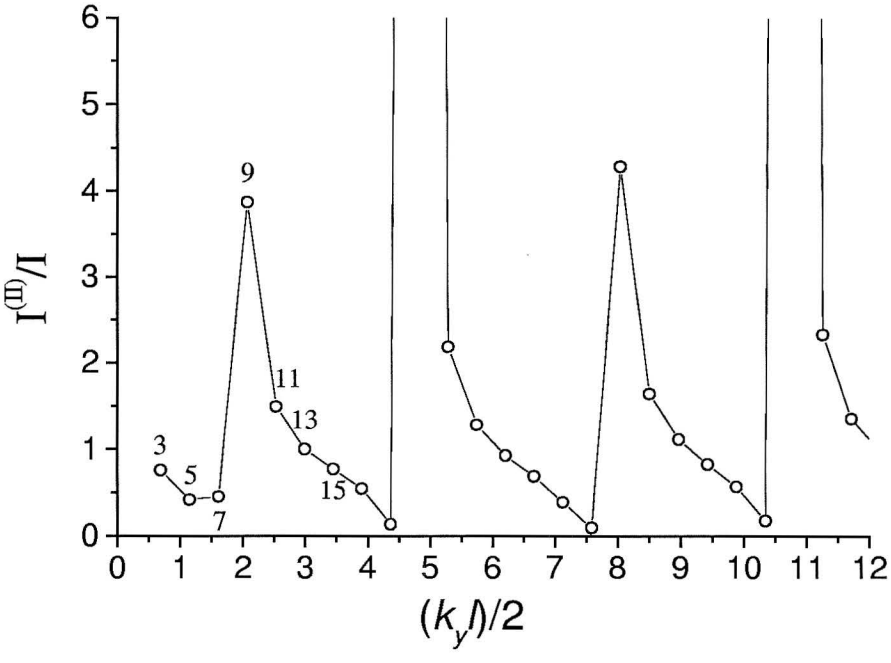

Figure 4.21: The relative intensities $I^{(II)}/I$ as a function of α. The first few modes $n_y = 1, 3, 5, ...$ are indicated. See text.

$m = 1$ yields:

$$\begin{aligned} \alpha &= \frac{k_y l}{2} = \frac{n_y \pi}{L} \frac{l}{2} \\ \Rightarrow \quad n_y &\approx \frac{L}{l} = \frac{160\mu m}{20\mu m} = 8. \end{aligned} \tag{4.19}$$

Even though $n_y = 8$ is itself a "hidden" mode, the modes with values closest to it should exhibit relatively large changes in the observed FMRFM signal intensity. The FMRFM spectra of the $20 \times 160\mu m$ sample with the probe magnet close to the surface is shown in detail in Figure 4.18. The $n_y = 3$, 11, and 13 modes are relatively unchanged, as expected. The observed signal intensities of the $n_y = 7$ and $n_y = 9$ modes are enhanced, exhibiting significant changes as predicted.

The signal intensity of the fundamental mode ($n_y = 1$), however, is observed to decrease as the probe magnet is brought near the sample surface. The wavenumber of the fundamental mode is $k_y = \frac{\pi}{160\mu m} = \frac{1}{51\mu m}$, which yields $k_y^{(II)} < 0$ (for $\delta k \approx \frac{1}{22\mu m}$). Negative wavenumbers, within the approximations of Kalinikos, are unphysical and should not exist. Thus, we can only infer that something different should happen to the fundamental mode when the probe field pushes $k_y \rightarrow 0$. This is clarified within the more sophisticated model of Chen *et al.*, which is currently under development.

4.3 Effect of the FMRFM technique on signal detection

4.3.1 Line shape distortion and broadening

The fundamental mode of the YIG FMRFM spectra is often distorted – sharp and narrow on the low field side, and rounded and wide on the high field side. Also, the total line width of the fundamental mode varies from $8 - 15G$ in typical measurements, and is even wider for high RF power measurements. This is in contrast to conventional FMR spectra, where the typical resonance signal is Lorentzian and has a line width of $1 - 3G$. These two phenomena, the distorted line shape and the broadened line width in FMRFM spectra, are directly related to the RF power input to the microstrip and appear to result from overdriving the resonance.

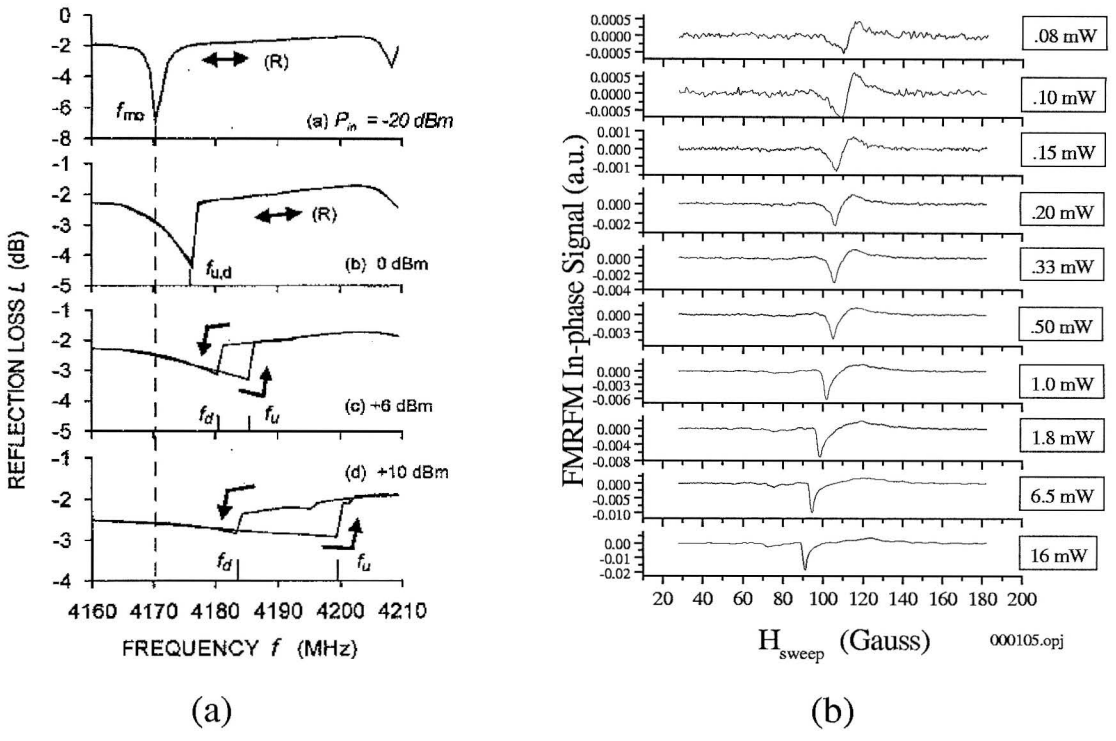

(a) (b)

Figure 4.22: (a) The foldover effect. After Fetisov *et al.* [62]. (b) FMRFM spectra as RF power is increased. Note that the distorted resonance shapes and shifts to lower fields (higher frequencies) correspond between the Fetisov data and FMRFM data.

The FMR spectra of the $20 \times 160 \mu m$ YIG sample as a function of RF power input into the microstrip is shown in Figure 4.22(b). The distortion of the fundamental mode as the power is increased can be clearly observed. To interpret the distortions as a result from overdriving the resonance, a comparison of these FMRFM spectra to similar measurements performed by Fetisov *et al.* [62] is given below.

In the linear regime, the FMR is driven by a low power RF source, and the magnetic moment precesses uniformly with a small angle about its equilibrium position. The resonance has a Lorentzian response, as is shown in Figure 4.23(a). At high RF powers, the precession angle increases, which will increase the effect of the nonlinear terms in the dispersion relation. (The dispersion relation was derived by assuming small precession angles

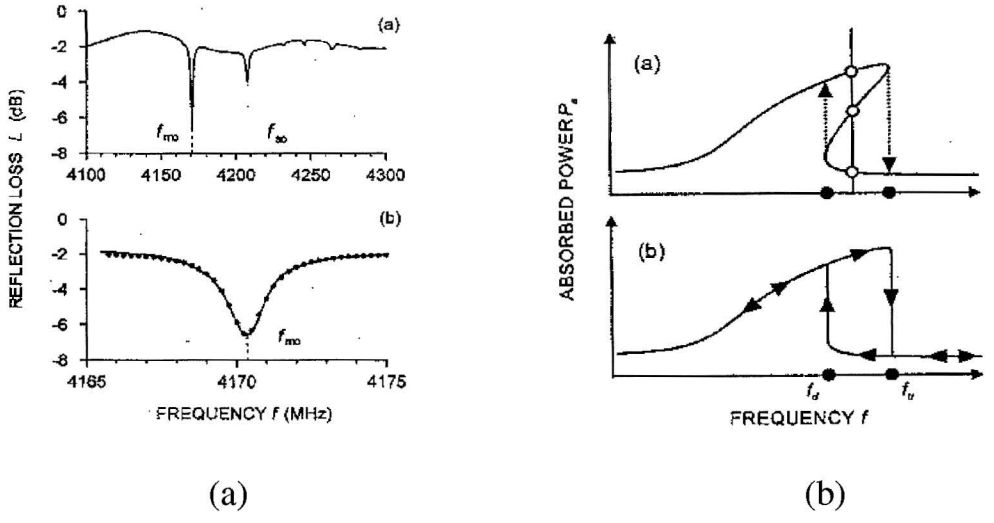

(a) (b)

Figure 4.23: (a) The Lorentzian shape of a low RF power resonance of a YIG sample. (b) The classic foldover effect. After Fetisov *et al.* [62].

and linearizing about equilibrium. See Chapter 2.)

A nonlinear response at high RF powers, known as the "foldover" phenomena in FMR, was first proposed by Anderson and Suh [60]. The form of the foldover effect was first depicted by Weiss [61]. This is the classical response of a overdriven nonlinear oscillator, which has two stable responses corresponding to the direction of the field (or frequency) sweep, as shown in Figure 4.23(b). Anderson and Suh also proposed that a larger precession cone reduces the static component of the magnetization perpendicular to the film plane. This will result in a resonance field shift towards lower fields.

The nonlinear response of YIG to increasing RF power has been studied extensively for many years. However, it was only in the recent measurements of Fetisov *et al.* (Nov 1999) [62] that influences from Q cavity interactions, heating, and magnetocrystalline anisotropy energy were excluded. This was the first time a direct comparison of experimental results with the classical foldover effect of Anderson and Suh could be made.

The measurements by Fetisov *et al.* were performed on a YIG single crystal sample ($1mm$ square, $4.9\mu m$ thick) mounted on top of a non-resonant microstrip ($3mm$ long, $50\mu m$

wide). Their conditions are very similar to those of this study, and provide an excellent basis for evaluating the nonlinear effects found in the FMRFM spectra.

Fetisov *et al.* obtained FMR spectra over a wide range of continuous wave (CW) RF powers, shown in Figure 4.22(a). The spectra were obtained by sweeping frequency (instead of the external field). A Lorentzian frequency response was observed at low RF powers, P_{RF}, ranging from -60dBm to -20dBm. At higher RF powers, the frequency response showed a distortion of the resonance signal ($P_{RF} = 0dBm$). As the RF power is further increased, the classical foldover response is obtained at 6 and $10dBm$. Our FMRFM spectra are shown as a function of increasing RF power in Figure 4.22(b), and sweeping upfield. The distortion of the lineshape and the increase in line width of the fundamental mode for increasing RF powers is quite evident, and mimics the data of Fetisov *et al.*

There are several critical features of the Fetisov *et al.* data that can be compared with the FMRFM data. First, the fundamental mode becomes distorted, but still nonhysteretic, over a large range of RF powers (-20dBm to 0dBm). Upfield and downfield sweeps, at powers of $P_{RF} = .08mW$ and $16mW$, were obtained via FMRFM on the $20 \times 160\mu m$ YIG sample, and are shown in (Figure 4.24). No shifts larger than the typical experimental uncertainty of $\pm 4G$ were observed. For powers up to $16mW$, the FMRFM spectra are distorted but still reversible. Note that at the lowest power, $P_{RF} = .08mW$, the lineshape is no longer distorted, but is the derivative of a Lorentzian as expected.

Second, the spectra of Fetisov *et al.* were obtained with frequency, not field, sweeps. A shift in the resonance frequency to higher frequencies (for swept ω measurements) corresponds to a shift in the resonance field to lower fields (for swept H measurements). This shift to lower fields as the RF power was increased was observed in the FMRFM data, shown in Figure 4.22(b). This shift directly stems from the larger cone of precession, which decreases the component of the static magnetization normal to the film plane.

Third, Fetisov *et al.* also performed pulsed measurements to avoid heating effects. Sample heating can produce an effect similar to those of the foldover effect. However, experiments performed in 1987-1991 demonstrated that pulse measurements eliminate this response [62], although distorted line shapes and increased line widths were still present.

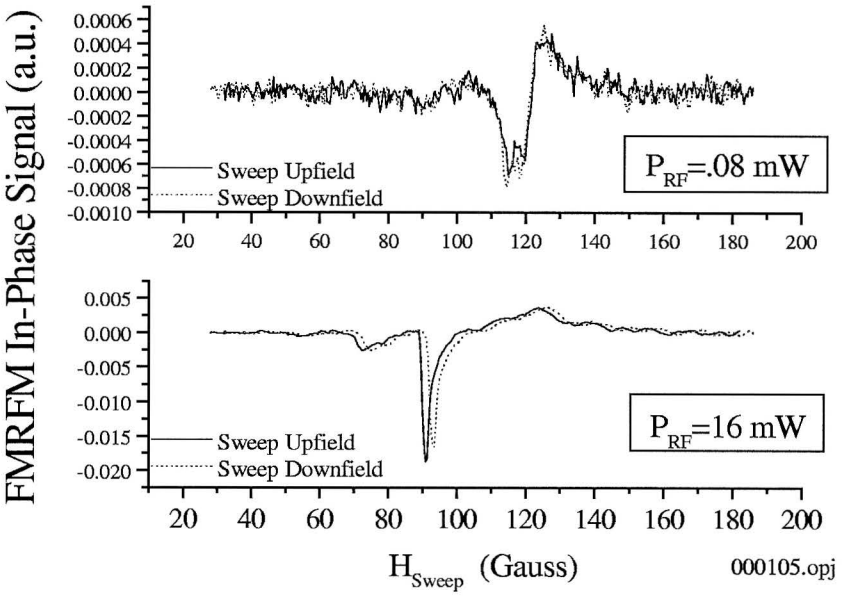

Figure 4.24: Spectra of the fundamental mode of the $20 \times 160\mu m$ sample as the field is swept upfield and downfield. Sweeps were performed at low RF power ($0.08\,mW$) into the microstrip and high power ($16\,mW$). No hysterysous larger than the experimental error of $\pm 4G$ is evident.

The pulse measurements of Fetisov *et al.* matched their down-sweep frequency spectra taken with CW power. They found no heating effects for the pulse lengths ranging from $1 - 100\mu s$ at a $1kHz$ repetition rate. In this work, FMRFM data is obtained through the anharmonic modulation technique. This involves modulation of the RF power amplitude at $31kHz$, while the external field is modulated simultaneously at $13\,kHz$ by a few gauss. This technique is roughly similar to the pulse method used by Fetisov *et al.* The pulse lengths and repetition rates are on the same order as the modulations used in FMRFM. The use of anharmonic modulation may be why classic foldover effects at high RF powers were not observed, even though the RF input powers were similar to Fetisov *et al.*

LINE WIDTHS

The resonance line width is a measure of the rate at which energy is lost from the uniform precession mode. There are two kinds of losses which are directly related to temperature and surface effects [63].

1. Spin-Lattice Relaxation – Energy is directly transferred from the fundamental mode into lattice vibrations. This coupling between the spin system and atoms is provided by relatively few ions (i.e., rare earths) that are coupled to both the magnetic spin system and the crystal lattice.

2. Spin-spin Relaxation – Energy is transferred into spin-wave modes which are degenerate with the fundamental mode precession. This coupling may be provided by any imperfection in the crystal. For single crystal YIG, surface imperfections provide most of the scattering centers.

The line widths of $2mm$ YIG polished disks were obtained by both FMRFM and conventional FMR methods. This was used to determine if the FMRFM technique altered the line width (excluding overdriving effects due to RF power) instead of additional losses due to sample dimensions and preparation. The larger $2mm$ samples were used because conventional FMR methods cannot resolve signals from samples with microscale lateral dimensions. The observed line widths obtained with FMRFM were $3G$, for the field parallel to the film plane, and $4G$, for the field perpendicular to the film plane. The observed line widths obtained with conventional RF absorption measurements were $3G$ for the field both perpendicular and parallel to the film plane. These measurements indicate that the FMRFM system does not affect the line width adversely. The FMR spectra obtained with RF absorption were provided by Prof. P.E.Wigen [64].

The line widths of the microscale rectangular YIG samples were larger than the bulk line widths of the $2mm$ YIG disks. The fundamental and higher order modes have line widths of $6G$ in a perpendicular magnetic field (Fig. 4.22). The line widths were obtained at low RF powers to avoid nonlinear effects. For higher RF powers, the line widths ranged from 8-15 Gauss.

The increased line width can be explained by surface effects. The edges of the YIG are not polished and are not truly perpendicular (3° wall slant). Both effects are from the ion milling procedure. These unpolished, slanted edges account for 17% or more of the surface area. The line width is highly dependent upon the smoothness of the surface, and rougher surfaces correspond to wider line widths [65]. Thus, an increase in the line width as a result of the ion milled edges is expected.

4.3.2 Effect of H_{mod}

The modulation field, H_{mod}, adds a small oscillating magnetic field on top of the large external field as it is swept through resonance: $H_{res} + H_{\mathrm{mod}} \cos(\omega_{\mathrm{mod}} t)$. (See anharmonic modulation, Chapter 3.) The FMRFM signal intensity depends directly upon the field strength of H_{mod} and the line width of the sample, ΔH. Increasing H_{mod} can increase the signal intensity. However, if H_{mod} is too large relative to the line width, it will reduce the signal amplitude and average out features in the resonance signal.

To maximize signal intensity, the external field at the sample must be modulated completely in and out of the resonance condition. This maximizes the change in the magnitude of the oscillating component of the magnetization, m_z. The resonance condition is satisfied over a field equal to its line width ΔH centered at H_{res}. If H_{mod} is less than the line width ($H_{\mathrm{mod}} < \Delta H$), then the external field will not be modulated completely in and out of the resonance condition. If $H_{\mathrm{mod}} \approx \Delta H$, the modulation will move the external field completely in and out of the resonance condition, and will have the maximum contribution to FMRFM signal intensity. If H_{mod} is further increased ($H_{\mathrm{mod}} > \Delta H$), the finite contribution to the FMR signal (from m_z) will be averaged out over a larger field modulation, resulting in a decrease in signal intensity and an increase in apparent ΔH. Thus, the signal intensity as a function of H_{mod} amplitude will reach a maximum when $H_{\mathrm{mod}} \approx \Delta H$.

However, the H_{mod} serves as an averaging mechanism. If $H_{\mathrm{mod}} = 5G$, then any signals within the $5G$ sweep will contribute to the signal. For example, $H_{\mathrm{mod}} >> \Delta H$, the narrow line width resonance will appear to be $5G$, but at a lower amplitude than if $H_{\mathrm{mod}} \approx \Delta H$. Furthermore, if two narrow line width resonance features were separated by less than H_{mod},

they would not be resolved but appear as one peak with $\Delta H \approx H_{\text{mod}}$. The effect of H_{mod} on two narrow line width features is shown in Figure 4.25.

The FMRFM signal of the $20 \times 160 \mu m$ sample as a function of H_{mod} is shown in Figure 4.25. For an input voltage of $35 - 55mV$, an H_{mod} of $3 - 5Guass$ is produced by the small modulation coils. Only one resonance peak is observed for these H_{mod} amplitudes. By reducing H_{mod}, smaller features of the resonance line shape are observed. The double peaks in the fundamental mode are resolved at $2G$ apart at an input voltage of $25mV$. The double peaks are due to the substrate/YIG interface, where there is a mix of YIG and GGG. This $2G$ double peak is often seen in YIG samples, and has been observed in samples from the T-18 substrate in previous conventional FMR experiments performed by P.E. Wigen.

4.3.3 Effect of θ_{RF} on RF magnetization in the sample

The finite dimensions of our sample have effects on the magnitude of the RF component of the magnetization, m_z. This effect, due to sample dimensions, has large effect on the signal intensity and can be approximated from demagnetization arguments.

The RF source for our FMRFM apparatus is a microstrip resonator. The sample is directly mounted onto the microstrip. The RF field H_{RF} may be orientated relative to the sample at an arbitrary angle θ_{RF}, while keeping the sample plane perpendicular to the external polarizing field. A schematic of the orientation is shown in Figure 4.26(a) for the parallel force geometry. The normal operating orientation, for spectra presented elsewhere in this chapter, are obtained with the long axis of the sample perpendicular to the RF field ($\theta_{RF} = 0°$).

The FMRFM spectra versus the RF field orientation to the sample is shown in Figure 4.26(b). The maximum intensity is obtained for the RF field perpendicular to the sample's long axis, $\theta_{RF} = 0°$. The intensity then decreases as the RF field approaches parallel to the sample's long axis. This effect can be qualitatively explained by the demagnetization effect on the RF component of the magnetization, $\vec{m}$.

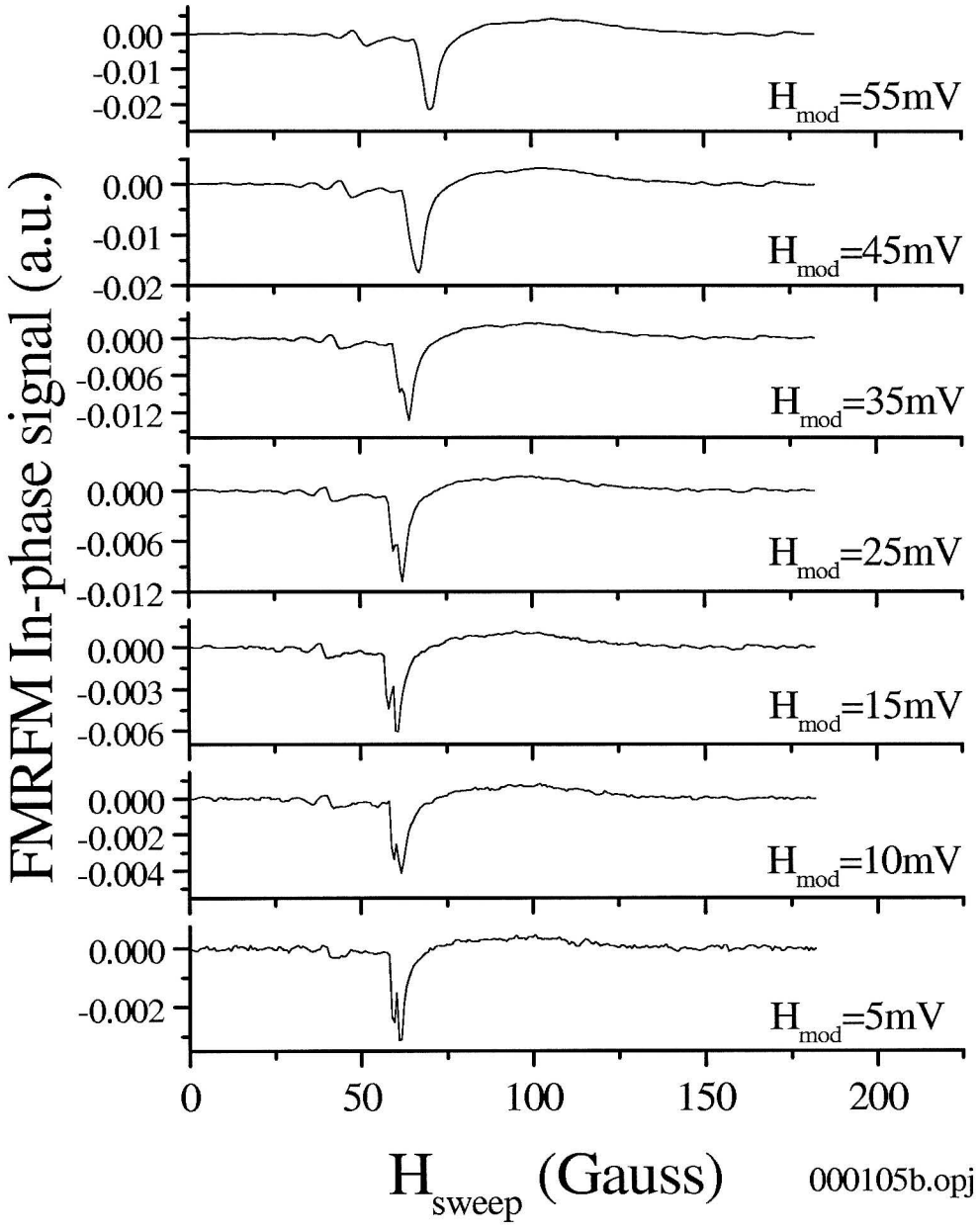

Figure 4.25: Spectra of the $20 \times 160 \mu m$ YIG rectangle as a function of H_{mod} intensity. The double resonance peaks, spaced at $2Gauss$ apart, are resolved for $H_{\text{mod}} \approx 25mV$.

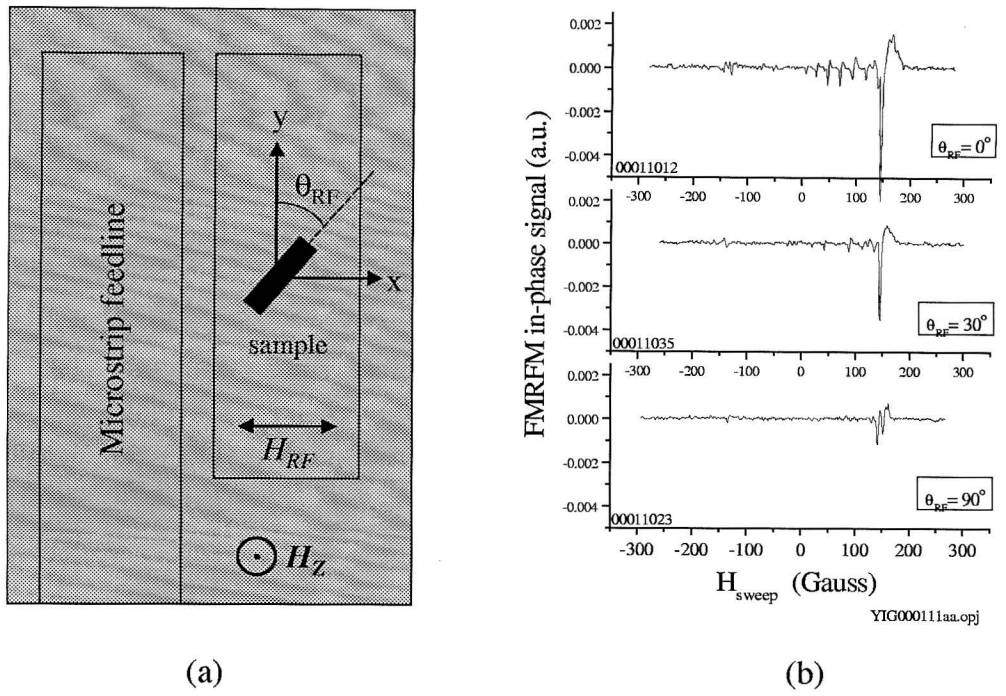

Figure 4.26: (a) Schematic of the orientation of the YIG rectangular sample with respect to the RF microstrip resonator. The RF field is in the x direction, and the external magnetic field is in the z direction. (b) Spectra of the $20 \times 160 \mu m$ YIG sample as a function of RF angle.

Consider the effect of the sample's orientation to the RF field for a single moment in the sample. For this approximation, the spatial dependence of the RF component of the magnetization is neglected, and $\vec{m} = (m_x, m_y, m_z)$. The magnetization $\vec{m}$ will create an opposing demagnetization field in the sample for each direction. From the torque equation 2.7, $\frac{d\vec{M}}{dt} = \gamma \vec{M} \times \vec{H}$, the dependence of the magnetization on the RF field is

$$\begin{aligned} m_y &\propto M_z \times H_{RF} \quad \text{RF field parallel to sample long axis,} \\ m_x &\propto M_z \times H_{RF} \quad \text{RF field perpendicular to sample long axis,} \end{aligned} \tag{4.20}$$

where the external field is taken to be in the z direction.

When the RF field is parallel to the sample's long axis (i.e., both are in the x direction), it creates a magnetization in the y direction, m_y. This moment, in turn, creates a demag-

netization $4\pi m_y$ across the width of the sample. Likewise, the RF field perpendicular to the sample's long axis creates a demagnetization $4\pi m_x$ along the length of the sample. Since the width is much smaller than the length of the sample ($w = 20\mu m$, $l = 160\mu m$), the demagnetization across the width is much larger than the demagnetization across the length, $4\pi m_y >> 4\pi m_x$. Since more energy is required for the moment to overcome the larger demagnetization, the tilt of the precession angle of the magnetic moment is reduced along the y direction. Thus, the reduced tilt of the magnetic moment for the $\theta_{RF} = 90°$ orientation results in a reduced FMRFM signal, as was observed (Fig. 4.26(b)).

The effect of the reduced tilt on the FMRFM signal intensity can be estimated from demagnetization arguments. The demagnetization field depends on the dimension of the sample, as has been shown previously (see section: "Fundamental mode dependence on sample length"). For simple approximation purposes, the demagnetization is considered to depend linearly upon the sample dimension. The demagnetizations $4\pi m_y$ and $4\pi m_x$ are compared to the demagnetization across the thickness of the sample $4\pi m_z$. The demagnetization in the z direction is the same for all orientations. Thus, for the two extreme cases of $\theta_{RF} = 0°$ and $\theta_{RF} = 90°$, the demagnetization effects are approximated as

$$\frac{h_d(m_y)}{h_d(m_z)} \propto \frac{20\mu m}{3\mu m} \quad \text{and} \quad \frac{h_d(m_x)}{h_d(m_z)} \propto \frac{160\mu m}{3\mu m}. \tag{4.21}$$

Thus, the relative intensities of the FMRFM signal are approximated as

$$\frac{h_d(m_x)}{h_d(m_y)} \approx \frac{160\mu m}{20\mu m} \approx 8. \tag{4.22}$$

From the spectra in Figure 4.26(b), the observed relative intensities of $\theta_{RF} = 0°$ and $\theta_{RF} = 90°$ are approximately 4. This is in good agreement considering the extreme approximations made.

4.4 Ongoing research

In the course of this study, several phenomenon were observed that warrant further study and understanding. These will be pursed in our MRFM group in future experiments.

4.4.1 Unidentified resonance

A new FMRFM apparatus was designed and recently built for use in a Lakeshore water-cooled electromagnet. This electromagnet supplies a uniform external magnetic field over a $1cm$ diameter, and can reach fields as high as $6000G$ for a 2" pole separation. This new apparatus was used to verify earlier results obtained with the "old" FMRFM apparatus, and to calibrate the absolute fields of the resonance spectra.

In the course of verifying previous spectra, sweeps to higher magnetic fields, unobtainable in the old FMRFM apparatus, revealed a new unidentified resonance. This resonance, shown in Figure 4.27, is present for all samples in the $20\mu m$ series. A similar resonance, at a slightly higher field, is also present for the $2mm$ YIG disk. The resonance is at lower fields for the $100 \times 100\mu m$ sample.

This unidentified resonance is quite large compared to the fundamental modes of the $20\mu m$ YIG series. It also persists when the probe magnet is located between samples, and far from the sample surface (tip-to-sample distance of $1mm$). The resonance does not shift with respect to sample dimensions in the $20\mu m$ series. The resonance also occurs at $H \approx 4.5kG$, much higher than the expected resonance of $\approx 4.2kG$ for the fundamental mode of the $20x320\mu m$ sample. It is even higher than the expected resonance of $H \approx 4.35kG$ expected for the fundamental mode of a bulk YIG sample. The resonance for the $2mm$ disk is $4.6kG$, much higher than the expected $4.23kG$ from conventional FMR measurements. (Measurements of the YIG disk with conventional FMR methods were performed at $9.215GHz$ and yield an $H_{eff} = 1.868kG$, and $\gamma = 3.175$ ($g = 2.245$). These measurements were provided by P.E. Wigen.) The lack of dependence of the resonance field on the sample dimension, and also the high resonance field, indicate that this is not likely an FMR signal from the YIG.

No resonance was observed for spectra taken with a bare GGG substrate nor with the probe magnet located above the bare microstrip. This rules out possible resonance from these sources.

Spectra were also taken from samples not from the T-18 batch, as shown in Figure 4.28.

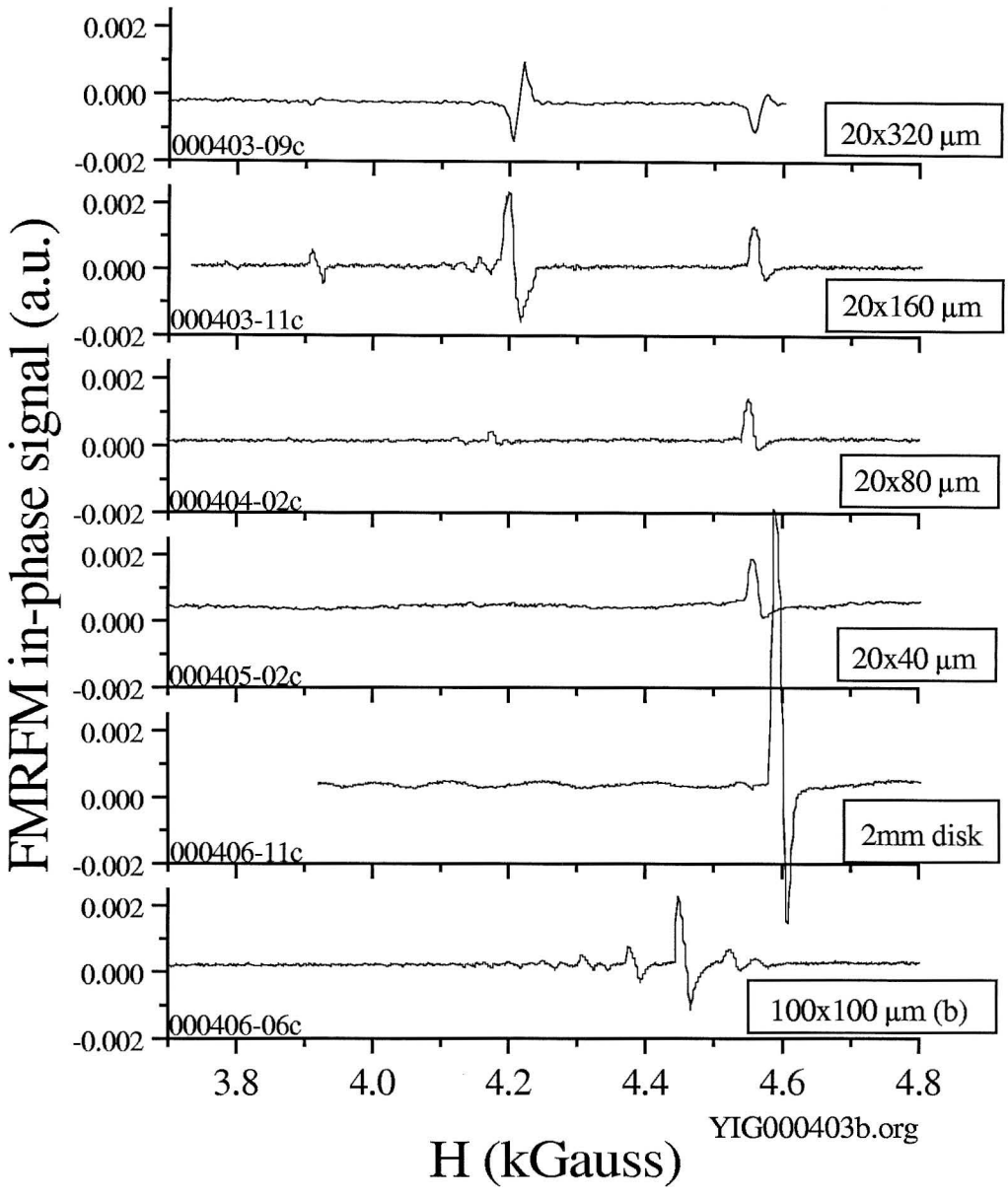

Figure 4.27: Spectra from the $20\mu m$ series, the $100 \times 100\mu m$ sample, and the $2mm$ disk. All samples were from the T-18 YIG batch. The $20\mu m$ series and the $100 \times 100\mu m$ sample are on the same GGG subtrate.

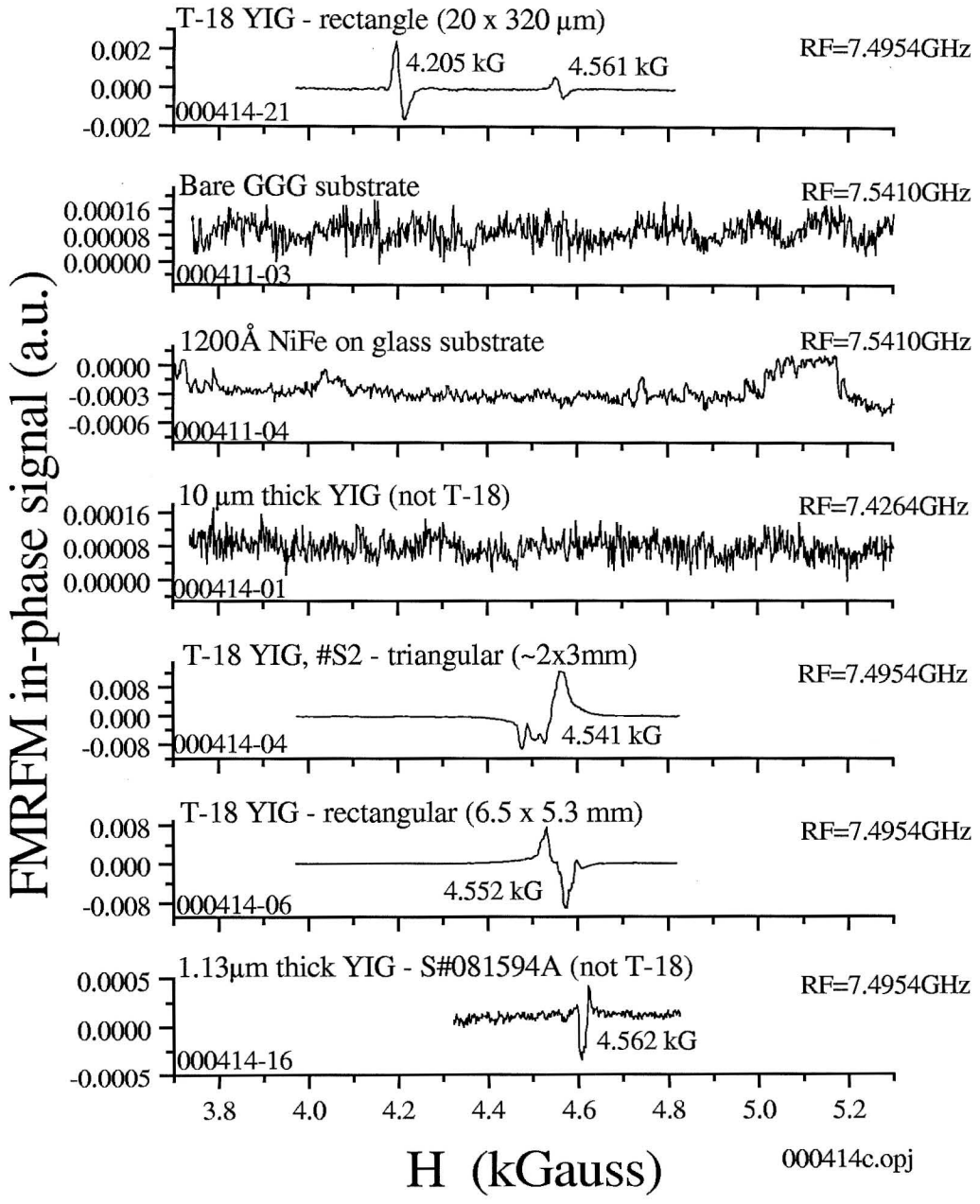

Figure 4.28: Spectra from several different types of YIG samples. See text.

The unidentified resonance was observed in all of the T-18 YIG samples and the $1.13\mu m$ thick YIG sample (S#081594A, not T-18). Regular FMRFM signals have been obtained previously with all these samples. The resonance was not observed in the $10\mu m$ thick sample. This particular sample has its c-axis parallel to the plane of the film, as was determined from acid etching. Thus, its resonance properties are very different from the pure YIG crystal with the c-axis perpendicular to the film plane.

A possible source for the unidentified resonance is an FMR signal from the NiFe probe magnet. The FMR signal for NiFe ranges from $2kG$ for the external field in the plane of the film plane to $10kG$ for the external field perpendicular to the film plane. The cantilever tip, coated with 1200Å of NiFe, has a 10° angle from the axis. Furthermore, the cantilever is mounted at a 15° angle with respect to the sample's normal. Thus, the tip surface has angles ranging form $5° - 25°$ from the external magnetic field. A FMR signal from a NiFe thin film with the external field at 25° could have a resonance around $4kG$.

Another possible source of the unidentified resonance is coupling between the NiFe tip and the YIG sample. This could explain why the resonance is only observed in YIG samples with the c-axis perpendicular to the film plane.

A remote possibility is that the unidentified resonance could be a surface mode. This is unlikely, as the field is fairly uniform and perpendicular to the sample. Only volume modes are allowed for a uniform field perpendicular to the film plane (see Chapter 2).

The most likely source of the unidentified resonance is an FMR signal of the NiFe tip.

4.4.2 Coupling problems

The NiFe tipped commercial AFM cantilevers provide uniform magnetic probes of small dimensions with high gradient fields. However, they require the parallel force geometry, which has two drawbacks. When the magnetic NiFe-tip of the cantilever is brought close to the surface, $\leq 1\mu m$, the cantilever experiences a degradation of Q, and the probe magnet can stick to the surface of the sample.

There is a large magnetic attraction between the probe magnet and the sample which causes the cantilever to flex in the direction of the sample. This force can result in the

magnetic NiFe-tip snapping to the sample surface when the probe magnet is brought too close. This could be solved by using a perpendicular force geometry, where the deflection of the mechanical resonator is parallel to the sample surface. Thin magnetic films, which produce high gradient fields, can be deposited on cantilevers or beams to act as the probe magnet (see Appendix E).

Interactions between the probe magnet and the sample cause a degradation of Q of the cantilever. While the exact source of this has yet to be determined, there are two possible explanations. First, simple aerodynamic damping of the cantilever when it is close to the surface can reduce the Q. The YIG FMRFM measurements were all performed in ambient pressure, which would maximize this effect. Second, magnetic energy dissipation in the NiFe tips due to domain wall fluctuations could also lead to damping the cantilever oscillation. Grutter *et al.* have suggested that oscillations of the domain wall widths in the sample, due to the alternating magnetic fields created by oscillating NiFe-tip, create magnetoelastic emission of phonons [66], [67]. Thus energy is transferred from the cantilever magnetic probe tip and dissipated via phonons in the sample, producing a measurable reduction of the Q of the cantilever. Our samples are saturated in a large external field, and a degradation of Q is not likely to be due to domain wall fluctuations in the sample. However, there could be domain walls in the NiFe tip, which could be affected by this mechanism.

The source of the degradation of Q, and new mechanical resonators to prevent sample to surface sticking, are being further pursued in our group.

5 Thin ferromagnetic metallic films

Studies on single and trilayer Co films were performed to demonstrate the ability of FMRFM to characterize ferromagnetic metallic thin films on a microscopic scale. These measurements were the first demonstration of FMRFM applied to thin magnetic films and multilayer samples. They demonstrate the ability of this technique to distinguish and characterize the anisotropy energy and thickness of separate layers in samples with lateral dimensions on the microscale. Part of the following results have been published in reference [68].

The abilities of FMRFM were demonstrated by two critical measurements that characterized important properties of the samples (see Chapter 2).

1. H_{res} as a function of θ_H, K_{u2}: Anisotropy energy is a good characterization of surface and interface smoothness of each layer in the sample. The resonance field H_{res} depends critically upon the uniaxial anisotropy energy of the thin film, K_{u2}, and upon the angle of the external field relative to the normal of the film plane, θ_H. The dispersion relation, from Chapter 2 Eq. 2.21, is

$$\left(\frac{\omega}{\gamma}\right)^2 = H\left[H\cos\left(\theta_0-\theta_H\right)+H^{eff}\cos\left(2\theta_0\right)\right]\frac{\sin\theta_H}{\sin\theta_0}, \tag{5.1}$$

where $H^{eff} = \frac{2K^{eff}}{M_S} = \frac{2\left(K_{u2}-2\pi M_S^2\right)}{M_S}$. From this dispersion relation, resonance measurements as a function of θ_H, or at a known fixed angle, can determine the uniaxial anisotropy energy of the thin film, K_{u2}. Samples with different anisotropies will exhibit different dependencies on θ_H.

2. H_{res} as a function of t_{film}: For Co films thinner than 100Å, the resonance field, H_{res}, is a function of thickness of the film, t_{film}. For a film with the external field in plane, the dispersion relation simplifies to $\omega = \gamma\sqrt{H\left(H+4\pi M_{eff}\right)}$, where $M_{eff} = 4\pi M_S - \frac{2}{M_S}K_{eff}$. However, in this regime, the effective anisotropy energy

K_{eff} involves two contributions: a volume (K_V) and a surface (K_S) component. As discussed in Chapter 2, K_{eff} is defined by the empirical formula [21]

$$K_{eff} \approx K_V + \frac{2\ K_S}{M_S\ t_{film}}. \tag{5.2}$$

As the film becomes thinner, the effects of the surface (pinning, anisotropies, defects) become increasingly important. FMR measurements can determine the thickness, volume (K_V) and surface (K_S) anisotropies of each layer.

In these studies, two series of samples were characterized. First, single layer 500Å and 1000Å thick ferromagnetic films from two different sample preparation techniques were measured, and the anisotropy energy and angle dependence of a single layer deduced. As described below, the results obtained were consistent with expectations. Detailed measurements of the resonance field as a function of the angle of the external field relative to the normal of the film plane, θ_H, fit theoretical predictions extremely well.

Second, multilayer ferromagnetic films for various thicknesses of $\leq$ 100Å were characterized, and their thickness and angle dependence deduced. The experimentally determined anisotropies and thickness were consistent with values found in the literature. These studies demonstrate the accuracy and applicability of FMRFM on ferromagnetic multilayer films.

5.1 Single layer films

5.1.1 Experimental details

The following measurements were conducted with the sample deposited onto a commercial AFM cantilever, as shown in Chapter 3, Figure 3.1. The gradient fields, $\frac{\partial H_i^{bar}}{\partial z}$, and the external magnetic field, H^{bar}, were supplied by a macroscopic $Nd_2Fe_{14}B$ permanent bar magnet, $\frac{1}{4}$" diameter and $\frac{1}{4}$" long. The perpendicular force geometry was employed, in order that both the axis of the bar magnet and the plane of the sample are parallel. This is defined to be the z axis. The displacement of the cantilever was in the y direction. The force on the cantilever, derived in Chapter 3, was

$$F_y = m_y \frac{\partial H_y^{bar}}{\partial y} + m_z \frac{\partial H_y^{bar}}{\partial z}, \tag{5.3}$$

where m_y and m_z are the components of the magnetic moment of the Co film along the y and z axes. The dominant external field was in the z direction, which results in $m_z >> m_y$. In order to create a significant force for detection, the film must be placed off the z axis of the bar magnet to obtain a finite value of $\partial H_y^{bar}/\partial z$. As a result, the external field at the sample is orientated at an angle, ϕ_H, with respect to the film plane (n.b., $\phi_H = \frac{\pi}{2} - \theta_H$).

Measurements were conducted with an RF field of $7.9GHz$ in ambient pressure and temperature. Anharmonic modulation was used to obtain the FMRFM signal.

The polycrystalline Co films were deposited onto the flat area near the tip of single crystal Si commercial AFM cantilevers. Two deposition methods, sputter [69] and evaporation [70], were used in order to compare differences in anisotropies due to deposition techniques. Each Co film had a Ag polycrystalline underlayer to act as a buffer between the Co and Si surface. Buffer layers have been shown to improve the magnetic qualities of the magnetic films. Finally, each Co film was capped by a protective polycrystalline Ag layer. All layers were deposited in immediate succession in the same run without breaking vacuum. The sizes and locations of the samples on the cantilever were determined by a simple shadow mask.

Results from three samples are included in this study: Sample 1, with a thickness of 1000Å, was sputter deposited at a substrate temperature of $< 50\,^{\circ}C$ onto a 30Å Ag buffer layer. Samples 2 and 3, with thicknesses of 1000Å and 500Å respectively, were thermally evaporated onto 50Å Ag buffer layers with unknown substrate heating. All samples were capped with a 10-15Å protective layer of Ag.

The gradient field produced by the bar magnet was $\frac{\partial H_y^{bar}}{\partial z} \sim 0.15\ G/\mu m$. For our Co samples, which are $\sim 100 - 200\mu m$ long, the gradient field corresponds to a field difference of $15 - 30\,G$ across the film: $\frac{\partial H_y^{bar}}{\partial z} \cdot L = (.15\frac{G}{\mu m})(100\mu m) = 15G$. However, the resonance line width of the Co films are $50 - 100\,G$. Since the line width is greater than the field difference across the film, the entire sample fits inside the resonance volume and contributes to the FMRFM signal at H_{res}. Hence, these experiments do not provide lateral spatial resolution of the magnetostatic modes within the sample.

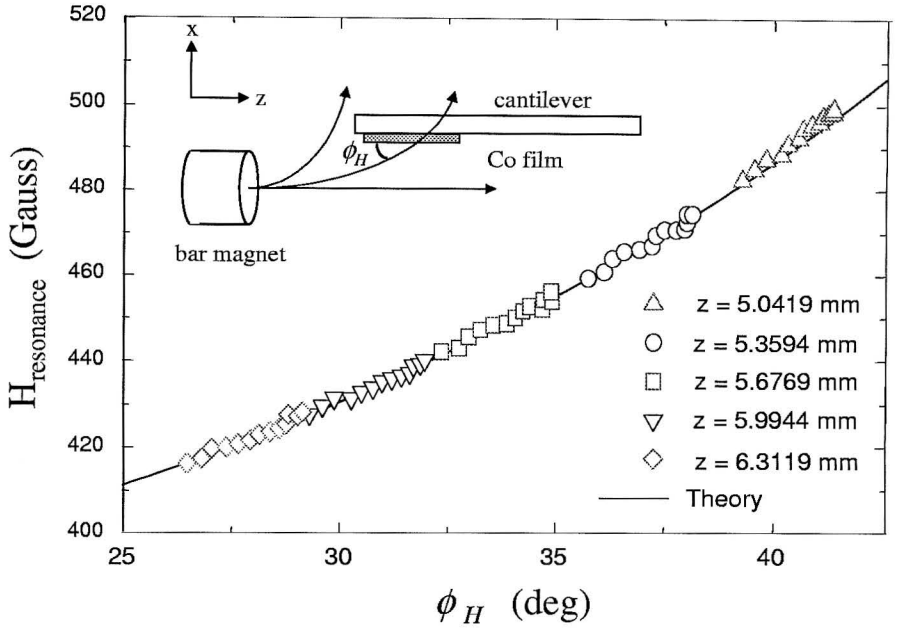

Figure 5.1: Dependence of the resonance field on the angle ϕ_H between the external magnetic field and the film plane for the sputtered Co sample. The solid line is a theoretical fit from classical FMR theory with $g = 2.18$ and $4\pi M_{eff} = 17.6kG$. The inset shows a schematic of the FMRFM apparatus.

5.1.2 Angle dependence and anisotropy energy measurements

The anisotropy energy K_{u2} of the sputtered film was determined by the dependence of the resonance field on the angle ϕ_H, as shown in Figure 5.1. The angle ϕ_H was varied by displacing the Co film with respect to the bar magnet in either the x or z direction, thus changing the x and z components of the magnetic field applied to the film. In Figure 5.1, several measurements along the x direction at each position of z were taken.

The solid curve in Figure 5.1 is the theoretical prediction from FMR theory (Eq. 5.1). For the sputtered film, a uniaxial anisotropy energy of $K_{u2} \sim 0$ was assumed, and the bulk demagnetization field of $4\pi M_{eff} = 17.6kG$ was used. This assumption reflects the quality of the films, produced under optimized deposition conditions [69]. Excellent agreement between theory and experiment was obtained, as shown in Figure 5.1.

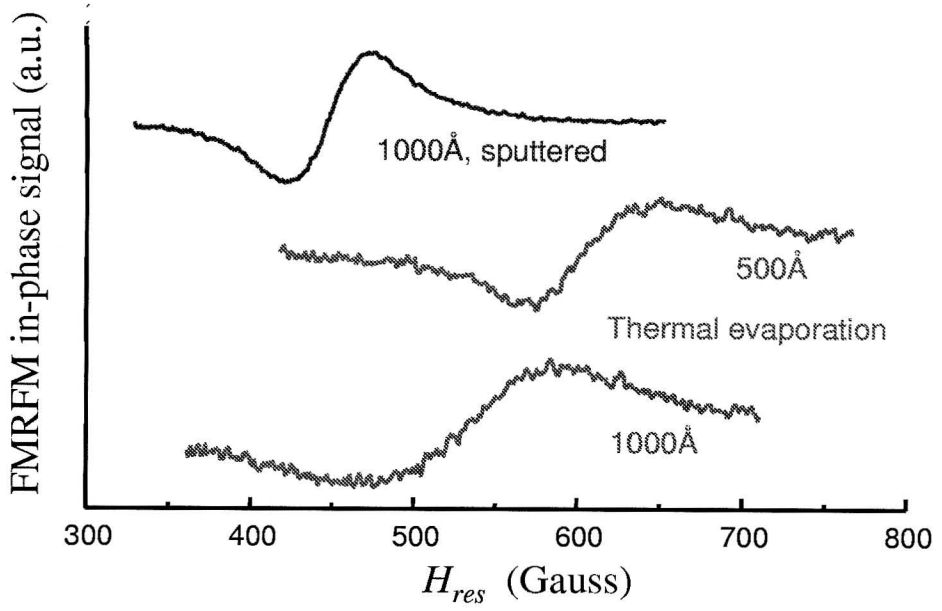

Figure 5.2: Spectra from three different single layer Co films. Two different deposition methods were used, as indicated. The shift in resonance is due to different anisotropies in the samples. The angle between the sample and the external field is $\phi_H = 33°$. RF = 7.9GHz.

The spectra of the three samples obtained at $\phi_H \simeq 33°$ is shown in Figure 5.2. These spectra reveal the samples' dependence on the anisotropy and film quality due to the deposition method and film thickness. The resonant field H_{res} for evaporated films is larger than that for the sputtered film, indicating additional anisotropy in the evaporated films. The additional anisotropy could arise from stresses in the film resulting from non-optimal deposition conditions. The thermally evaporated samples were not optimized for stress free films due to difficulty of controlling the deposition rates of Co at its high melting temperature.

A bulk value for the saturation magnetization for Co, $M_S = 1400 emu/cm^3$ is assumed for these samples, all of which have thicknesses greater than 100Å. From the dispersion relation, the values $\frac{2K_{u2}}{M_S} \sim 0$ for the sputtered film, $\frac{2K_{u2}}{M_S} \sim 2.8kG$ for the 1000Å evaporated film, and $\frac{2K_{u2}}{M_S} \sim 4.9kG$ for the 500Å evaporated film were deduced. The uniaxial anisotropy energy, K_{u2}, can be increased as a result of surface imperfections or stress at the layer interface. The evaporation conditions were not optimized to eliminate interlayer

stress and imperfections, as were the sputtered films. Thus, as expected, the results that were obtained indicate that the evaporated samples developed larger stresses and surface imperfections, and hence larger anisotropies, than the sputtered films.

The results apparently also indicate that the effects of stress and surface imperfections increase with decreasing film thickness. The surface imperfections increase K_S, and thus their effects on the resonance condition are averaged over the volume of the sample. Therefore, as the volume increases, the relative effect due to the surface decreases, as was observed.

A dependence of the sample homogeneity on the deposition process is also evident in Figure 5.2. The sputtered sample has the narrowest line width, approximately $45G$. A difference in line widths could be obtained if the samples were of different lengths and if the resonance volume was smaller than the sample dimensions (i.e., $\frac{\partial H_y^{bar}}{\partial z} > \Delta H$). In this regime, the longer sample will contribute to the resonance signal over a wider field as the resonance volume is swept through the sample. This extended signal could be interpreted as a wider line width. This effect is depicted in Figure 5.3, where the resonance volume (Δz) is swept through samples of different length, L_1 and L_2.

However, the sputtered sample ($\sim 200 \times 50\mu m$) had larger lateral dimensions than the evaporated samples ($\sim 100 \times 50\mu m$). The resonance volume compared to the sample length cannot explain the wider line width. Therefore, the variation in the line width reflects the quality or the homogeneity of the Co film.

The spectra indicate that sputtering produced a more homogeneous film than does evaporation. This is to be expected since the thermally evaporated films were deposited on a non-temperature controlled substrate optimization of their magnetic properties was not attempted. Of the two evaporated samples, the 500Å film has a narrower line width than the 1000Å film. The 1000Å film was evaporated in two stages (i.e., two wire boats containing Co were used) which could have caused additional inhomogeneities.

These experiments demonstrated the ability of the FMRFM to observe variations in the anisotropy energy and the quality of microscopic thin films. The gradient field was not large

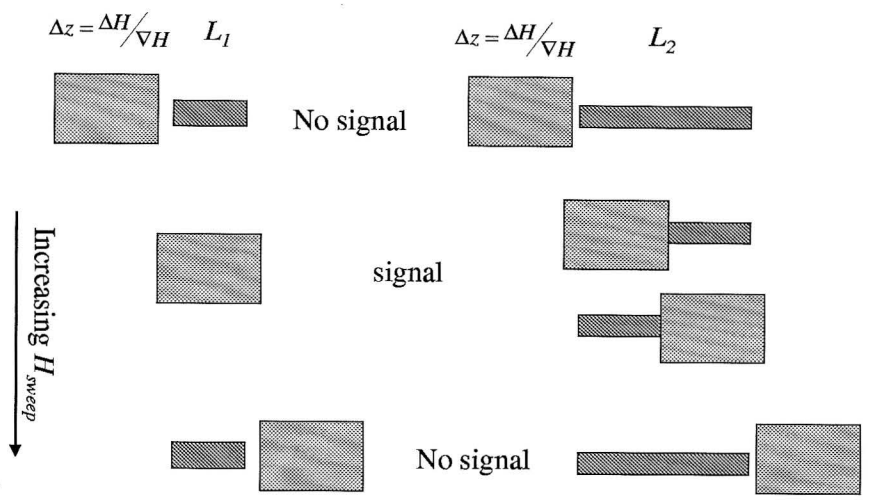

Figure 5.3: A pictorial of an apparent increase in line width as a result of the resonance volume being smaller than the sample length. See text.

enough to distinguish FMR signals from different locations within the sample. However, the large signal intensities in ambient temperature and pressure indicate that the sensitivity of this FMRFM apparatus is adequate to detect FMR signals from samples as thin as 20Å. This was verified in our experiments on multilayer films for samples of thickness 100Å and 50Å, with lateral dimensions of $40\mu m$.

5.2 Multilayers - (Co/Cu/Co)

Spectra from microscale Co/Cu/Co trilayer samples have been obtained, and their thickness and anisotropies were determined. The thickness of the various layers are 100Å or less, so that these samples resemble materials used in giant magnetoresistance (GMR) devices. At such thicknesses, bulk values of the demagnetization field and anisotropy energies no longer apply. Much experimental work has been done recently in the field to determine anisotropy energies due to thickness and interface layers [21][71][72][73][74][75][76].

In this study, two experiments were performed on the Co/Cu/Co samples to demonstrate the ability of FMRFM to characterize micron scale multilayers. First, for films of thickness $\leq$100Å, the resonance signal H_{res} is a function of thickness. The volume and surface

anisotropy energies, and the thicknesses of the layers, were determined. Second, the resonance field depends upon the angle of the external field to the normal of the film plane, θ_H. The different anisotropies of each layer also result in different dependencies of H_{res} on θ_H. Both effects were observed.

5.2.1 Experimental details

The experimental apparatus was the same as used for the single layer experiments described above.

The samples were sputter deposited onto the flat area near the tip of commercial single crystal Si AFM cantilevers [69]. They were $40 \times 40\mu m$ square. Their geometry was determined by a shadow mask placed over the cantilever during sputter deposition. For the data presented here, each trilayer was composed as follows: 30Å Ag buffer layer; a 15Å, 35Å, or 50Å Co layer; a 150Å Cu spacer layer; a 100Å Co layer; and finally a 35Å Cu protective top layer. The relatively large (150Å) Cu spacer layer ensured that there was no magnetic coupling between the Co layers. Coupling was intentionally avoided in these first experiments in order to determine the ability of FMRFM to resolve *individual* layers in multilayer devices. Each cantilever had a 100Å Co layer which yields a "reference" resonance signal. Samples on different cantilevers could then be compared using the position of this 100Å Co resonance as a common external magnetic field value.

The gradient field produced by the bar magnet was $\sim 0.15\ G/\mu m$. For these Co samples, which are $40\mu m$ long, this corresponds to a field difference of $6G$ across the film. The resonance line width of the Co films are $50 - 100G$. Since the line width is greater than the field difference across the film, essentially the entire sample meets the resonance condition. Thus, the applied gradient field does not allow resonance signals arising from lateral spatial dependencies to be distinguished within the sample.

5.2.2 Anisotropy and thickness dependence

The thickness and anisotropy energy of two samples, both with layer thickess of 50Å Co/ 150Å Cu / 100Å Co, were determined. The spectra of one such sample is shown in Figure

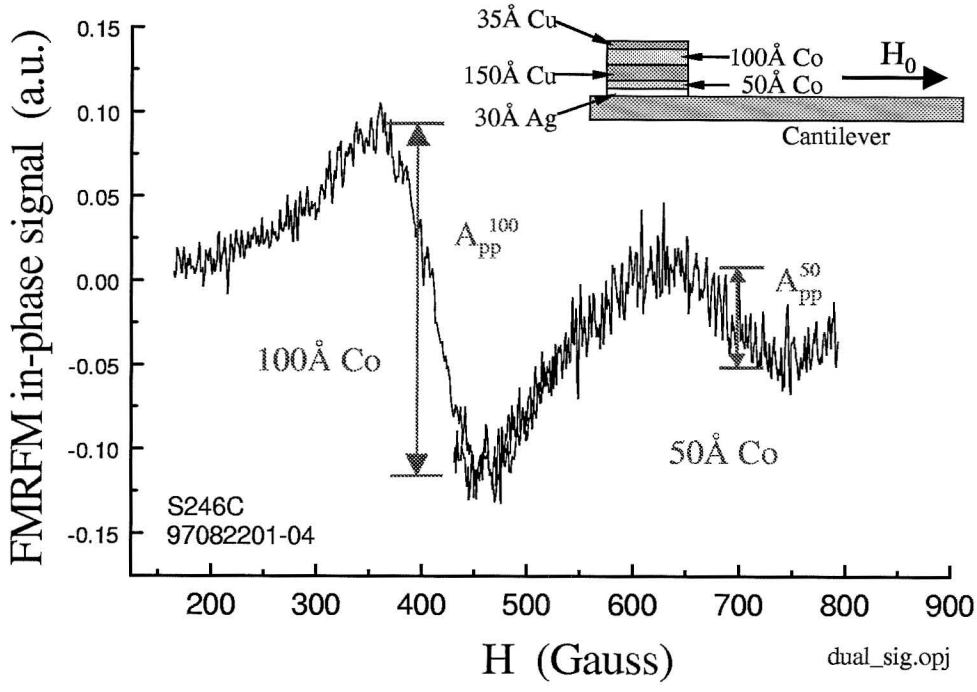

Figure 5.4: The spectra from the (50Å Co/ 150Å Cu / 100Å Co) trilayer sample. The peak-to-peak amplitudes of the resonance from the 100Å and 50Å layers are indicated as A_{pp}^{100} and A_{pp}^{50}, respectively. The insert shows a schematic of the sample on the cantilever.

5.4. The peak-to-peak amplitudes of the resonance from the 100Å and 50Å layers are indicated as A_{pp}^{100} and A_{pp}^{50}, respectively. The line widths of each resonance are $114G$ and $117G$ respectively. The insert shows a schematic of the sample on the cantilever.

The FMRFM signal amplitude is determined by $\vec{F} = \vec{m} \cdot \nabla \vec{H}$, and the RF component of the magnet moment, m, is proportional to the thickness of the sample. Therefore, the amplitude of the FMRFM signal is approximately proportional to the thickness of the sample for constant ∇H. For the 50Å Co/ 150Å Cu / 100Å Co sample, the relative amplitudes are $A_{pp}^{50}/A_{pp}^{100} \approx 0.3$. If the thicker 100Å layer is assumed to be accurate, the thickness of the 50Å layer must be less than expected (discussed below). From this simple ratio, the thickness of the layers are approximately $t_{Co}^{50} \sim 30$Å and $t_{Co}^{100} \sim 100$Å.

There are several possible sources for the thickness discrepancy of the 50Å layer. First, the $40 \times 40 \mu m$ mask window could interfere with deposition by *reducing* the total Co

deposited or by reducing the amount of Co deposited near the edges of the mask opening. Second, the large lattice mismatch between the Ag/Co interfaces known to create stress and interface roughness. This can result in what is commonly termed a magnetic "dead layer." The Ag/Co dead layer could have very different resonance properties than the pure Co, and thus would reduce the overall resonance intensity. Dead layers of $5-8$Å have been reported in the literature for sputtered Co/Mn samples [74]. Third, the Ag layer could be too thin to act as a good buffer layer between the Co and the Si cantilever surface. This would further increase the rough surface interface between the Ag and Co layers. The apparent reduction of the Co thickness due to the Ag/Co interface is most like a combination of these effects.

In contrast, the Cu/Co/Cu interfaces is not expected to suffer as acutely from these effects. The Cu layers acts as a "smoothing" agent, and can reduce the roughness to a few monolayer thickness [77]. The 100Å Co layer has a 150Å Cu buffer layer separating it from the Co/Ag layer and the Si cantilever. Thus, the value of the thickness for the Cu/100Å Co/Cu layer is expected to be more accurate than the Ag/50Å Co/Cu layer. The data confirms these expectations.

The volume and surface anisotropy energies of the 100Å and 50Å Co layers can be estimated by fitting their resonance fields to the empirical formula

$$4\pi M_{eff} \approx \frac{2}{M_S}\left(K_V + \frac{2\ K_S}{M_S\ t_{film}}\right). \tag{5.4}$$

Each Co layer has different anisotropy energies due to the different interface types. The range of values of K_V and K_S (and the resultant $4\pi M_{eff}$) determined by the experimental data are shown in the following tables for each interface type. For reference, typical values of the anisotropy fields found in the literature are included [21] [72][75][71].

For the Cu/Co interface:

$4\pi M_{eff} \approx \frac{2}{M_S}\left(K_V + \frac{2\ K_S}{M_S\ t_{film}}\right)$	Fitted (our data) (Cu/Co interface)	Typical values (Cu/Co interface)
t_{Co} (Å)	100	10 - 50
K_V $(\times 10^6 erg/cm^3)$	0.9 - 1.2	0.9 - 2.0
K_S (erg/cm^3)	0.1 - 0.2	0.1 - 0.35
$4\pi M_{eff}$ (kG)	$\sim$ 15.7	14-16.8

For the Ag/Co interface:

$4\pi M_{eff} \approx \frac{2}{M_S}\left(K_V + \frac{2\ K_S}{M_S\ t_{film}}\right)$	Fitted (our data) (Ag/Co interface)	Typical values (Ag/Co interface)
t_{Co} (Å)	30	15 - 30
K_V $(\times 10^6 erg/cm^3)$	1.4 - 2.0	1.0 - 1.4
K_S (erg/cm^3)	0.4 - 0.5	0.2 - 0.4
$4\pi M_{eff}$ (kG)	$\sim$ 9.4	9.5 - 10.5

The experimentally determined values fall within the values typically found in the literature. These measurements verify the ability of FMRFM to determine anisotropy energies and thicknesses for microscale samples.

5.2.3 Angle dependence

The resonance field H_{res} is a function of the angle between the external field and the plane of the film., ϕ_H. Since the two layers of different thicknesses have different anisotropy energies, their angular dependence are expected to differ. The spectra of the (50Å Co/ 150Å Cu / 100Å Co) sample is shown in Figure 5.5 as a function of ϕ_H. The zero crossings of the spectra, which determine the resonance field for each spectra, are indicated by the dashed lines. The increase in the resonance field as an increase in ϕ_H is observed. The observed resonance field dependence on ϕ_H also differs between the two layer thickness, as expected. This provides further verification that the anisotropy energies of the two Co layers are different, as calculated in the above tables.

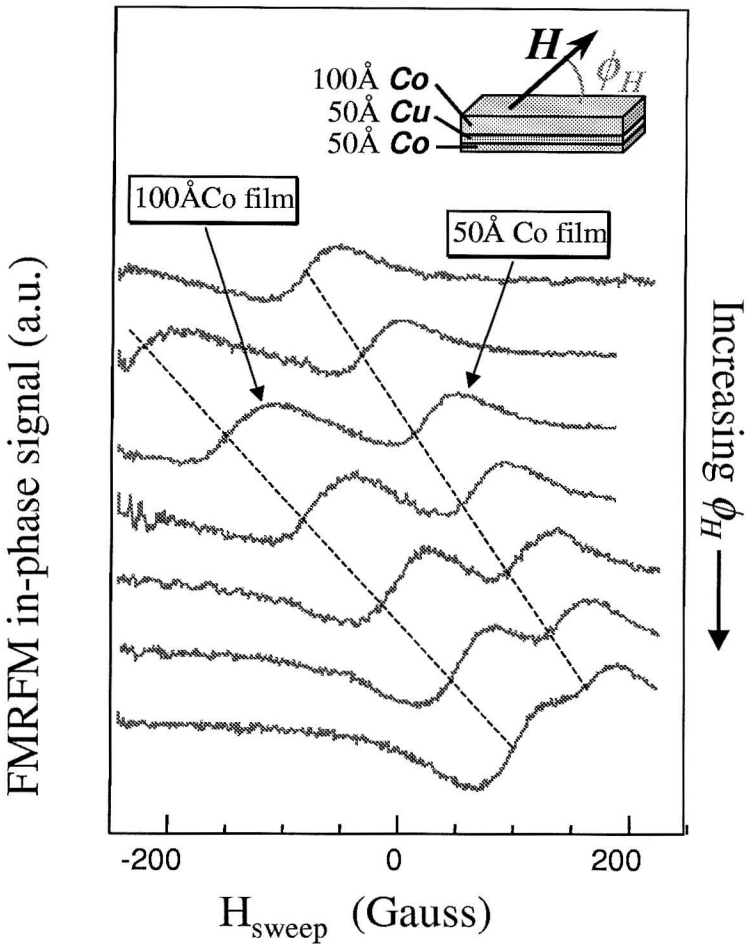

Figure 5.5: Spectra of the (50Å Co/ 150Å Cu / 100Å Co) sample as a function of the angle ϕ_H between the external field H and the film plane. See text.

5.2.4 Other samples of varying thickness

The series of multilayer samples included samples with Co thickness of 15Å, 35Å, and 50Å, in addition to the 100Å reference layer. The spectra of these three samples are shown in Figure 5.6. The resonance from the 100Å Co layer in each sample, and the 50Å layer, were observed. However, the resonance for the 15Å and 35Å layers were not observed. Possible reasons could be due to surface roughness or poor film quality due to deposition nonidealities. These effects, which were found to have reduced the thickness in the 50Å layer, could also have reduced the thickness of the 15Å and 35Å layers. This would result

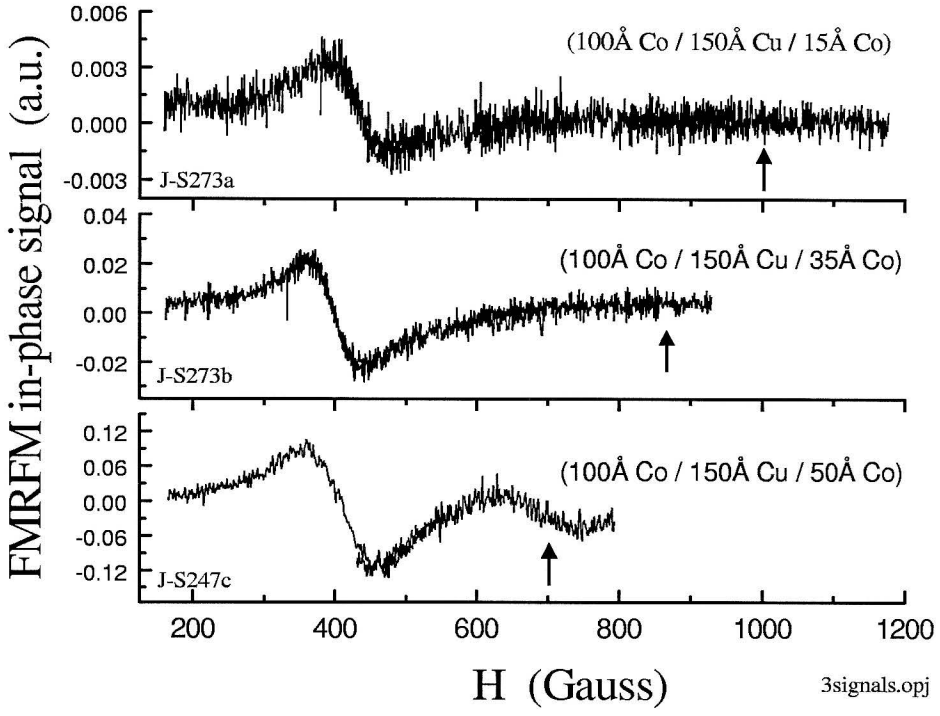

Figure 5.6: Spectra from the three trilayer Cu/Co/Cu samples. The resonance from the 100Å layer in each sample is evident. The expected positions of the resonances are indicated by arrows. Signals from the 15Å and 35Å layers were not observed.

in shifting the resonance fields several hundred Gauss, beyond the range of the available field sweep. Alternatively, the layers could have been too thin to produce a large enough FMRFM signal; note that the S/N of the 50Å layer is only ~ 2.

The S/N of the FMRFM can be increased by performing the experiment in vacuum, which greatly increases the Q of the cantilever. At ambient pressure, the Q is typically ~ 25, whereas in vacuum ($\leq 60mTorr$) the Q is typically 10^3. However, attempts to measure the samples in vacuum resulted in the destruction of the samples due to eddy current heating (see Chapter 3). Heat sinking the Co films, which were deposited onto Si cantilevers, was not possible. Future experiments are currently in progress in which the probe magnet is affixed to the cantilever. This will allow direct heat sinking of the sample.

These first studies on Co trilayers serve to demonstrate the ability of FMRFM to measure

the anisotropy energy, thickness, and interface roughness of very thin magnetic multilayers of microscale lateral dimensions. Distinct signals from thin Co/Cu/Co trilayers were observed, with thickness of ~50Å and ~100Å. The lateral size of these sample, $40 \times 40 \mu m$, are much smaller than the typical scale (mm^2) of samples required in conventional FMR. The volume and surface anisotropies, K_V and K_S, were approximated and met experimental values found in the literature.

Both FMRFM and conventional FMR have the ability to measure the surface effects on anisotropies as films become thinner. However, to our knowledge, effects on anisotropy energies due to the reduction of lateral dimensions have not yet been studied. Conventional FMR cannot provide measurements upon samples of micron dimensions. FMRFM, on the other hand, has the potential to characterize these lateral effects on such micron scale samples.

6 Conclusion

6.1 Spatial resolution

The experiments on YIG microstructures establish the physical principles of spatial resolution in FMRFM for two regimes related to the additional field from the probe magnet: (1) low fields (a few Gauss), which yield no discernible perturbation of the magnetostatic modes, and (2) higher fields ($\sim 60G$), capable of producing a measurable effect on the RF absorption of certain modes. Two types of spatial resolution, which we term spatial sensitivity and direct spatial resolution, are explored.

"Unperturbed" magnetostatic modes in YIG microstructures (low field limit)

The dispersion relation of the YIG samples in the geometrical series *R-Series* remains relatively unperturbed by the probe magnet when the NiFe-tipped cantilever is located at least $10\mu m$ above the sample surface. The small additional field supplied by the probe magnet at this distance is only a few Gauss. The minimal effect of the probe magnet is reflected in the excellent agreement between experimental and theoretical values of the magnetostatic modes as a function of sample dimensions (Figs. 4.6, 4.8, 4.7, 4.9, and 4.10).

The observed agreement of experimental and theoretical values confirms that the FMRFM technique provides measurement of ferromagnetic resonance in microscopic samples with reasonable accuracy. It also validates the assumptions made in the approximation of the dispersion relation for microstructures. In these approximations, the internal fields H_i were evaluated only at the center of the sample and were determined for a sample completely saturated along each axis. At the center of the sample, H_i is a minimum and therefore defines the bottom of a "potential well" which establishes the position of the

eigenvalue of the fundamental mode. The data suggest that the internal field can be approximated by this simple method, and, at first pass, it is not necessary to perform explicit calculations with extensive computer modeling [29].

The simple model further assumes that the internal field was uniform across the dimensions of the sample. The good fit between theoretical and observations for higher order modes indicate that variations of the internal field were small enough to justify this assumption. The measured variations in the mode amplitudes further verify that the approximated values of the wavenumber, assumed to be half wavelengths defined by the width and length of the sample ($k_y = \frac{n_y \pi}{w}, k_z = \frac{n_z \pi}{L}$), were reasonable.

Perturbed magnetostatic modes in YIG microstructures (higher field limit)

When the probe magnet is brought within a few μm of the sample surface, the additional field it supplies ($\sim 60G$) perturbs the dispersion relation of the sample (Fig. 4.18). The signal intensities of certain modes are observed to behave differently than those observed in the low field limit: the amplitude of the fundamental mode decreased, and the amplitudes of the higher order modes $n = 7$ and $n = 9$ are observed to increase. The simple model developed in Chapter 4.2 qualitatively accounts for these effects by decreasing the wavenumber of the mode in a small localized region (the interaction volume). The ratio of the signal intensities for the perturbed and unperturbed regimes (Eq. 4.18) indicate that modes with wavenumbers satisfying

$$\alpha = \frac{k_y l}{2} \approx \frac{\pi}{2} \tag{6.1}$$

should exhibit the largest changes in intensity. This was indeed observed. The perturbation appears to alter the RF absorption (i.e., signal intensity) of certain modes over a small, localized volume of the sample.

The observation of a "hidden" mode (Figs. 4.11, 4.12) further demonstrates the ability of the probe magnet to locally affect the dispersion relation in the higher gradient field regime. As the probe magnet was scanned across the sample dimensions, the localized perturbation from the high gradient field appears to create asymmetry in these suppressed

modes. The increase of the net magnetization of a hidden mode ($n_y = 2$), which results from the asymmetry, increases the coupling of the RF field to the mode. The resulting increase in signal intensity of the hidden mode is large enough to be observed.

In both cases, the resonance field H_{res} is still largely determined by the dimensions of the sample and by the external fields outside the interaction volume of the sample. In other words, the resonance fields are still comparable to what occurs in the weak gradient field case, i.e., the perturbed modes are not observably shifted. Instead, the intensities of the perturbed modes, which correspond to wavenumbers of unperturbed samples, become affected. These results indicate that the unperturbed region of the sample largely determines the effects of the perturbation within the interaction volume. This is a direct consequence of the strong magnetic coupling within the sample. These studies are a crucial first step toward understanding FMRFM in the high gradient field limit where the dispersion relations are expected to become completely determined locally. In this regime, FMRFM imaging becomes analogous with that of EPR MRFM (i.e., the limit of "direct" spatial resolution).

Spatial resolution of magnetic probes

Two types of spatial resolution are defined in Chapter 2: (a) "direct" resolution, in which the force and the resonance condition are determined locally, and (b) spatial sensitivity, in which the force is determined locally but the resonance condition is determined "globally" (i.e., by the sample geometry).

The experiments in Chapter 4 indicate that the spatial sensitivity of FMRFM is approximately determined by the dimensions of the probe magnet. The sensitivity is determined by the mapping of magnetostatic mode amplitudes within the sample. For the rectangular $50\mu m \times 20\mu m \times 15\mu m$ NdFeB particle, the spatial resolution was verified to be $\sim 50\mu m$ laterally and $18\mu m$ axially. The magnetic probe of the NiFe-tipped cantilever, which has a diameter of $4 - 6\mu m$ and a height of $10\mu m$, achieved an unprecedented lateral resolution of $< 15\mu m$. The NiFe-tipped cantilevers are also able to detect the relative phase of the modes with a spatial resolution of $2\mu m$ (Figs. 4.14 and 4.15).

Direct spatial resolution was discussed in the previous section. The studies indicate that it will depend upon the strength of the gradient field of the magnetic probe.

Effect of the FMRFM technique on signal detection

The FMRFM measurement can alter the ferromagnetic resonance signal for non-optimal choices of certain parameters. The FMR signal amplitude and shape have significant dependence upon the RF field strength, the modulation amplitude of H_{mod}, and the angle of the RF field relative to the long axis of the sample.

The RF field produced by the microstrip is observed to drive the FMR into a nonlinear regime at large RF input powers (Fig. 4.22). The effect results in a distorted FMR line shape and a broadened line width. These effects are found to be qualitatively similar to spectra obtained by Fetisov *et al.*[62] under similar experimental conditions. For low RF powers, the FMR remains in a linear regime, and the signal shape and line width are not distorted.

For amplitudes of H_{mod} larger than the line width of the sample, the signal amplitude is reduced. Furthermore, features of the sample with resonance fields separated by less than the amplitude of H_{mod} will be unresolved due to the averaging of the signal over the field equal to H_{mod} (Fig. 4.25).

The angle of the RF field relative to the long axis of the sample is observed to have a significant effect on the signal intensity. A dramatically reduced signal intensity is observed for the RF field oriented along the long axis of the sample. The precession angle of the moments is influenced by the RF demagnetization factors of the sample (which are determined by the orientation of the sample with respect to the RF field). An approximation of the magnitude of this effect is found to be in reasonable agreement with the data (Fig. 4.26).

6.2 Characterization of magnetic microstructures

The ability of FMRFM to characterize the crucial properties of magnetic microstructures are demonstrated by the measurements upon YIG microstructures and metallic thin films. The YIG microstructures were discussed in the sections above, and will concentrate here on metallic films.

Single and multilayer metallic thin films, similar to GMR devices, have been characterized on a lateral scale ($40 \times 40 \mu m$) orders of magnitude smaller than which is required by conventional methods. The gradient field in these experiments was insufficient to provide lateral spatial resolution of the magnetostatic modes within the samples.

Single layer Co films, obtained from different deposition methods, were characterized. The relative differences in the measured anisotropy energies resulting from the deposition methods were determined. The experimental values were reasonable within qualitative analysis. The measured dependence of the resonance field on the angle of the external field relative to the film plane closely fit theoretical predictions.

Multilayer samples (Co/Cu/Co trilayers), which had thickness of $\sim$50Å and $\sim$100Å, were characterized. The volume and surface anisotropy energies, K_V and K_S, were determined for individual layers and had reasonable agreement with experimental values found in the literature. The apparent thickness of the 50Å layer was determined to be $\sim$30Å. The reduced thickness could be explained by interface effects.

These first studies on magnetic thin films demonstrate the ability of FMRFM to measure the anisotropy energies, thickness, angle dependence on H, and interface roughness of *individual* layers within a multilayer sample. The FMRFM sensitivity to small samples also demonstrates its potential to characterize the lateral effects produced by reduced dimensions of micron scale samples.

6.3 Future directions

6.3.1 Current apparatus challenges

Several challenges in optimizing the FMRFM technique remain to be investigated. Preliminary work is presented at the end of Chapters 3 and 4.

Sweeps to higher magnetic fields in the new FMRFM apparatus reveal a new unidentified resonance, shown in Figure 4.27. The most likely source of this signal is an FMR signal from the NiFe-tipped cantilever. This possibility could be verified by using cantilevers tipped with different magnetic materials, such as Co.

When the probe magnet is brought close to the surface ($\leq 1\mu m$), the thermal peak of the NiFe-tipped cantilever exhibits Q damping. This effect may be caused by domain wall fluctuations in the NiFe-tipped cantilever [66], [67]. Furthermore, the tip is attracted to the magnetic sample and can become magnetically pulled in to the surface. The attraction of the probe magnet to the sample surface can be nulled by designing magnetic probes on mechanical resonators that utilize the perpendicular geometry. The motion of the mechanical oscillations would be then parallel to the surface. This option is explored in Appendix E for magnetic films on Si beams.

Samples, especially metallic films, can experience destructive effects from eddy current heating when placed in the RF field. This problem can be reduced by heat sinking the microstrip. Thus, microstrips on sapphire, which possess superior heat sinking qualities to that of the Duroid, are currently under development.

6.3.2 Future experiments

Spatial resolution in YIG

Experimental and theoretical work is being continued on localized perturbations in YIG microstructures as a function of gradient field strength. Studies on the mode intensities as a function of tip-to-sample distance (i.e., gradient field strength) will be explored for smaller separations in order to determine the gradient field limit in which "direct" spatial resolution

can be attained. The simple model, which qualitatively accounts for the observations of the perturbed sample (higher gradient field limit), will be development into a more sophisticated model.

Spatial resolution in metallic films

Several new experimental difficulties arise in attaining spatial resolution in metallic films instead of in YIG microstructures.

First, metallic films such as Co or NiFe typically exhibit broad linewidths of order $50 - 100G$, whereas YIG has narrow linewidths of order $1 - 3G$ [63]. Therefore, the FMR signal of metallic films will be distributed over a larger spread in the external field. Thus, the spatial variation if the signal becomes quite weak and spatially resolving ferromagnetic mode amplitudes will become more difficult.

Second, the anharmonic modulation technique must be carefully applied since the modulations of the field amplitudes will be smaller than the linewidth. The modulation field H_{mod}, which is only a few gauss, will be unable to shift the sample completely in and out of the resonance condition.

Third, the total magnetic moment, and thus the signal intensity, of the metallic films is reduced compared to YIG samples of comparable lateral dimensions. Metallic thin films are typically orders of magnitude thinner than the YIG films in this study. Their magnetization (magnetic dipole density) ($4\pi M_S(Co) = 17.6kG$) is an order of magnitude greater than YIG films ($4\pi M_S(YIG) = 1.75kG$). Thus, the SNR may decrease by a factor of order ~ 100. The FMRFM signal can be enhanced by increasing the Q of the cantilever. If the experiment is performed in vacuum, however, problems due to sample heating are exacerbated because of the absence of convective cooling.

An experiment to characterize micron scale metallic films, namely single crystal Co dots, is currently in progress. The dimensions of these Co structures will be varied in order to determine the minimum detectable volume and to explore the effects of reduced lateral dimensions on the anisotropy energy in metallic films. The localized perturbation due to a strong gradient field will also be investigated in these metallic films.

Multilayer films

Multilayer films may exhibit coupling between magnetic layers that are separated by a non-magnetic layer with thickness of only a few monolayers. The exchange energy between the magnetic layers is a vital characteristic of GMR devices. An experiment to demonstrate the ability of FMRFM to characterize the exchange energies as a function of the individual layer qualities (thickness, anisotropy energies, and interface qualities) is currently planned.

Bibliography

[1] J. A. Sidles, *Appl. Phys. Lett.* **58**, 2854 (1991).

[2] D. Rugar, *et al., Science* **264**, 1560 (1994).

[3] Z. Zhang, *et al.,* Appl. Phys. Lett., **68** 2005 (1996).

[4] J. A. Sidles, *Appl. Phys. Lett.* **68**, 1124 (1992).

[5] K.J. Bruland, *et al.,* Rev. Sci. Instrum., **66** 2853 (1994).

[6] D. Rugar, *et al., Nature*, **360** 563 (1992).

[7] D. Rugar, *et al., Appl. Phys. Lett.* **63** 2496 (1993).

[8] P.C. Hammel, Z. Zhang, G.J. Moore and M.L. Roukes, *J. Low Temp. Phys.,* **101**, 59 (1995).

[9] J.A. Sidles, *et al., Rev. Mod. Phys.* ***67*** *249 (1995).*

[10] Hoen, *et al.*, Solid-State Sensor and Actuator Workshop, Hilton Head, S.C., 1994.

[11] K. Wago, *et al., J. Vac. Sci. Technol. B*, **14** 1197 (1996).

[12] C.P. Slichter, "*Principles of Magnetic Resonance,*" Spinger-Verlag, New York, 1989.

[13] Z. Zhang, M.L. Roukes, and P.C. Hammel, "Sensitivity and spatial resolution for electron-spin-resonance detection by magnetic resonance force microscopy," *J. Appl. Phys.*, **80** (12) 6931 (1996).

[14] C. Kittel, Introduction to Solid State Physics 3rd Ed., John Wiley and Sons Inc., New York, p. 525 (1953) (corrected printing 1968).

[15] K. J. Bruland, *et al., J. Appl. Phys.*, **83** 3972 (1998).

[16] P.C. Hammel, Z. Zhang, G.J. Moore, and M.L. Roukes, *J. Low Temp Phys. Proc. of the Symposium of Quantum Fluids and Solids,* June 11-16 (1995) Ithica, NY, INVITED.

[17] P.E. Wigen, *Thin Solid Films*, **114** 135 (1984).

[18] D. O. Smith, *J. Appl. Phys.*, **49** (1978) 1592.

[19] Z. Zhang, *thesis,* "Ferromagnetic resonance study in exchange coupled magnetic/non-magnetic multilayer structures," 1994.

[20] Robert O'Handley, "Modern Magnetic Materials: Principles and Applications," John Wiley & Sons Inc, 2000.

[21] Feng, *et al.*, *J. Appl. Phys.*, **78** 5549 (1995).

[22] R.L. White and I.H Solt, *Phys. Rev.,* **104** 56 (1956).

[23] L. Walker, *Phys. Rev.*, **105** 390 (1957).

[24] R.W. Damon and J.R. Eshbach. J. Phys. Chem. Solids, **19**, 308 (1961).

[25] M. Sparks, *Phys. Rev. B*, **1** 3831, 3856, 3869. (1970).

[26] A. Akhiezer, V. Bar'yakhtar, and S. Peletminskii, *Spin Waves*, North Holland, Amsterdam, 1968.

[27] B. Schnider, *Phys. Status Solidi B*, **51** 325 (1972).

[28] B. Tittmann, *Solid State Commun.*, **13** 463 (1973).

[29] B.E. Storey, A.O. Tooke, A.P. Cracknell, and J.A. Przyslawa, *J. Phys. C*, **10** 875 (1977); **13** 2079 (1980).

[30] C. Borghese, P. DeGasperis, and R. Tappa, *Solid State Commun.*, **22** 463 (1973); **25** 21 (1978).

[31] M.J. Hurben and C.E. Patton, *J. Magn Magn Matt,* **139** 263 (1995).

[32] B.A. Kalinikos, *IEEE Proc.* **127** (Pt. H) 4 (1980).

[33] A. Butera, J.N.Zhou, and J.A.Barnard. *J. Appl. Phys.*, Proc. 44th Conf Mag and Mag Mat, April 2000.

[34] A.M.Portis, *Appl. Phys. Lett.*, **2** 69 (1963).

[35] Garstens, M.A. and Kaplan, J.I., *Phys. Rev.* **99** 459 (1955).

[36] A Crown-410 stereo amplifier was used to drive the modulation coils. It has a bandwidth of $20kHz$.

[37] Rogers Corporation, One Technology Drive, PO Box 188, Rogers, CT 06263-0188.

[38] T. Edwards, *Foundations for Microstrip Circuit Design*, John Wiley and Sons Inc., New York, 1981.

[39] David M. Pozar, *Microwave Engineering*, Addison-Wesley, Massachusetts, 1990.

[40] I.J. Bahl and P. Bhartia, *Microstrip Antennas*, Artech House, Massachusetts, 1980.

[41] Sonnet Software, Inc., 1020 Seventh North Street, Suite 210, Liverpool, NY 13088, www.sonnetusa.com.

[42] Micro-Coax Corp., 206 Jones Blvd., Pottstown, PA 19464-3465, www.micro-coax.com.

[43] E.H. England, *IEEE Trans. Microwave Theory Tech. (short papers)*, 47 (1976).

[44] SC12 Contact Ultrasharp silicon cantilevers. ND-MDT, POB 50 103305 Moscow, Russia.

[45] Gould Electronics, 34929 Curtis Boulevard, Eastlake, OH 44095-400, www.gould.com.

[46] New Focus, 2630 Walsh Ave., Santa Clara, CA 95051-0905, www.newfocus.com.

[47] P. Hariharan, "Basics of Interferometry," Academic Press, Inc, Boston 1992.

[48] D. Rugar, H.J. Mamin, R. Erlandsson, and B.D. Terris, *Rev. Sci. Instrum.*, **59** 2337 (1988).

[49] K.G. Libbrecht and J.L. Hall, *Rev. Sci. Instrum.* **64** 2133 (1993).

[50] D. Rugar, *et al., Ultramicroscopy 42* (1992).

[51] A. Moser and H.J. Hug, *Meas Sci Tech* 4 (1992).

[52] D. Rugar, *et al., Rev. Sci. Instr.* 59 (1988).

[53] D. Rugar, *et al., Appl. Phys. Lett.* 55 (1989).

[54] J.A. Sidles, Phys. *Rev. Lett.*, **68**, 1124 (1992).

[55] J.A. Sidles, *et al., Rev. Sci. Instrum.*, **63**, 3881 (1992),

[56] The YIG subtrate was provided by Prof. Phil Wigen, Ohio State Univ., OH.

[57] Special thanks to Richard Campbell of IBM Almaden for ion milling the sample.

[58] P.E. Wigen, *et al., J. Appl. Phys.*, **85** 4521 (1999).

[59] M. M. Midzor, *et al., J. Appl. Phys.*, **87** 6493 (2000).

[60] P.W. Andersdon and H. Suh, "Instability in the motion of ferromagnets at high microwave power levels," *Phys. Rev.* **100** 1788-1789 (1955).

[61] M.T. Weiss, "Microwave and low-frequency osciallations due to resonance instabilities in ferrite," *Phys. Rev. Lett.*, **1(7)** 239-241 (1958).

[62] Y.K. Fetisov, C.E. Patton, and V.T. Synogach, *IEEE Trans. Magn.*, **35 (6)** 4511 (1999).

[63] W.H. von Aulock, "Handbook of Microwave Ferrite Materials," Academic Press, New York (1965).

[64] P.E. Wigen, Ohio State Univ.

[65] R.C. LeCraw, E.G. Spencer, and C.S. Porter, *Phys. Rev.*, **110** 1311 (1958).

[66] Y. Liu, B. ellman, and P. Grutter, "*Appl. Phys. Lett.* **71** 1418 (1997).

[67] P. Grutter, Y. Liu, and P. LeBlanc, *Appl. Phys. Lett.* **71** 279 (1997).

[68] Z. Zhang, M. Midzor, J.R. Childress, M.L. Roukes, and P.C. Hammel, *Appl. Phys. Lett.* **79** 2036 (1998).

[69] The sputtered films were provided by J. Childress, Univ. of Fl.

[70] The thermally evaporated films were made at Caltech.

[71] F.J.A. Broeder, *et al. J. Magn. Magn. Mat.* **93** 562 (1991).

[72] A. Soliman, *et at.*, *Phys. Stat. Sol. (B)* **186** 437 (1994).

[73] W. Donner, *et al.*, *Appl. Phys.* **75** 6421 (1994).

[74] D. Spoddig, *et al.*, *J. Appl. Phys.* **79** 4929 (1996).

[75] M. Sakurai, *et al.*, *J. Phys. Soc. Japan*, **62** 1853 (1993).

[76] Chappert, *et al.*, *Phys. Rev. B*, 34 3192 (1986).

[77] T.J. Minvielle, *et al.*, *J. Appl. Phys.* **79** (Part 2A) 5116 (1996).

[78] H. Puszkarski, Acta Phys. Polonica, **A38**, 271 (1970).

[79] J. Jackson, "Classical Electrodymanics," John Wiley & Sons, New York (1975) p. 194.

[80] A.N. Cleland and M.L. Roukes, *Appl. Phys. Lett.* **69** 2654 (1996).

[81] Hans-Jurgen Butt and M. Jaschke, "Calculation of thermal noise in atomic force microscopy," Nanotechnology 6 1-7, 1995.

[82] J. Prescott, "Applied Elasticity," Dover Publications (1946).

[83] T.D. Stowe, *et al.*, *Appl. Phys. Lett.*, **71** 14 (1997).

[84] S.P Timoshenko *et al.*, "Vibration Problems in Engineering," John Wiley & Sons (1974).

[85] Conversations with Darrell Harrington, Caltech.

A Notations

FMRFM	Ferromagentic resonance force microscopy
NMRFM	Nuclear magnetic resonance force microscopy
FMR	ferromagnetic resonance
NMR	nuclear magnetic resonance
EPR	electron paramagnetic resonance
DPPH	2,2-diphenyl-1-picrylhydrazyl
YIG	yttrium iron garnet
F	force
∇H	field gradient
$\vec{M}$	magnetization
k	force constant of mechanical osciallator
f_c, ω_c	resonance frequency of mechanical osciallator
Q	quality factor of mechanical osciallator
H	external magnetic field
H_{res}	the external field at resonance
ω	frequency of resonance precession
H_{RF}	RF magnetic field
H_{mod}	modulation field of external field
m	RF component of the magnetic moment
ΔH	(resonance) line width
$\vec{H}_{eff}$	total magnet field due to the external, anisotropy, and demagnetization fields
$\vec{H}_u$	uniaxial anisotropy field
$\vec{H}_d$	demagnetization field
γ	gyromagentic ratio. g=2 for electrons
H_i	the internal magnetic field ($= H + H_d$)

k_i	the wave number of magnetostatic mode
M_S	saturation magnetization
K_{u2}	uniaxial anisotropy energy
K_{eff}	the effective anisotropy energy
K_V	volume anisotropy energy
K_S	surface anisotropy energy
$\bar{N}$	demagnetization vector
$H_{i,int}$	the i^{th} component of the internal magnetic field
λ	wavelength of the laser light
$f_{RF\,\mathrm{mod}}$	frequency of the amplitude modulation of the RF field
$f_{H\,\mathrm{mod}}$	frequency of the modulation field H_{mod}
δH	small local field from the magnetic probe

B Thermal noise and sensitivity in mechanical resonators

B.1 Introduction

To determine the response of an oscillating beam or cantilever, there are two equations of motion to consider. There are modes of oscillation where each particle of the beam executes simple harmonic motion (SHM) in the same period and phase. Period is independent of x, but amplitude is a function of x. So the frequency response of a particular point of a beam (for example, the free end of a cantilever) follows SHM, but its amplitude is determined by the shape of the beam which may not be a simple harmonic oscillator (SHO). The general equation is [84]

$$y(x,t) = u(x)\sin(\omega t + \phi) = u(x)\, e^{i(\omega t+\phi)} \tag{B.1}$$

where $y(x,t)$ is the amplitude, $u(x)$ is the motion of the beam, and ω is the resonance frequency of the oscillator.

To determine the vibration response of a beam due to thermal noise, two equations of motion are involved.

1. $e^{i(\omega t+\phi)}$ is the simple harmonic motion (SHM) of a particular point of the beam, such as the free end of a cantilever or the center of a uniform beam. This determines the frequency response (or transfer function $G(\omega)$) of that particular point (see section B.2).

2. $u(x)$ is determined by the transverse oscillations of a mechanical oscillator, such as a doubly clamped beam. From this equation, k, ω and δ for a particular section of the beam is found (section B.3).

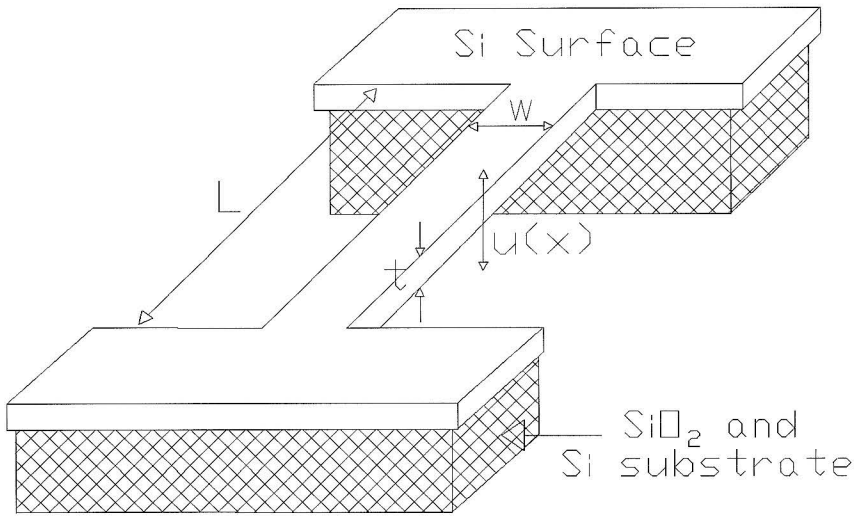

Figure B.1: A doubly clamped beam of thickness t, width w, and length L. The motion of the cantilever, $u(x)$, is indicated.

B.2 Sensitivity equations

The calculation of the force sensitivity of mechanical oscillators presented here follows the derivation by Butt [81] and Stowe [83].

The equation of motion for a SHO is

$$m\frac{d^2u}{dt^2} + c\frac{du}{dt} + k\,u = F(t) \quad \text{or} \quad \frac{d^2u}{dt^2} + 2\gamma\frac{du}{dt} + \omega_0^2\,u = \frac{F(t)}{m}, \tag{B.2}$$

where m is the mass, γ is the friction coefficient, Q is the quality factor, and k is the force constant. Note that for large Q, $2\gamma = \Delta\omega \approxeq \frac{\omega_0}{Q}$ and $\omega_0 = \sqrt{\frac{k}{m}}$.

Assume that the solutions to the motion of the mechanical oscillator and that the force function have the forms

$$\begin{aligned} u(\omega,t) &= u(\omega)\,e^{i\omega t}, \\ F(\omega',t) &= F(\omega')\,e^{i\omega' t} \end{aligned} \tag{B.3}$$

where ω is the resonance frequency of the oscillator and ω' is the driving frequency of the

force. Putting these into the equation of motion B.2, a general solution is obtained:

$$u(\omega) = F(\omega')\frac{1}{m}\frac{e^{i(\omega'-\omega)t}}{\left(\omega^2 - \omega_0^2 - i\frac{\omega\omega_0}{Q}\right)} = F(\omega')\,G(\omega',\omega). \tag{B.4}$$

For $\omega = \omega'$, this simplifies to

$$u(\omega) = F(\omega)\left[\frac{1}{m}\frac{\left(\omega^2 - \omega_0^2\right) + i\frac{\omega\omega_0}{Q}}{\left(\left(\omega^2 - \omega_0^2\right)^2 + \left(\frac{\omega\omega_0}{Q}\right)^2\right)}\right] = F(\omega)\,G(\omega) \tag{B.5}$$

where $G(\omega)$ is a transfer function defined by the brackets above.

The force can be Fourier transformed by the relation $F(t) = \frac{1}{2\pi}\int S_F(\omega')\,e^{i\omega' t}dt$. For white noise (thermal noise), $S_F(\omega')$ is a constant, or a flat power spectrum. In the case $\omega = \omega'$, the mean square deflection of the mechanical oscillator caused by thermal vibrations is

$$x_{rms}^2 = \int_0^\infty S_F(\omega)\;|G(\omega)|^2\;d\omega = S_F\int_0^\infty |G(\omega)|^2\;d\omega \tag{B.6}$$

where S_F is the flat power spectrum of the thermal force noise, and $G(\omega)$ is the transfer function of the mechanical oscillator (i.e., its response to frequencies). For $Q >> 1$, the integral can be evaluated to get:

$$S_F^{1/2} = \sqrt{\frac{4}{Q\omega_0}}\,k\,x_{rms} \tag{B.7}$$

For a system in thermal equilibrium, the equipartition theory states that each independent quadratic term in its total energy has a mean value of $\frac{1}{2}k_BT$. We define the relation:

$$\left.\begin{matrix} U_{beam} \\ U_{Cantilever} \end{matrix}\right\} \frac{1}{2}k_{eff}\;\delta^2 \tag{B.8}$$

where U_x is the bending (or potential) energy, k_{eff} is the effective force constant, and δ is the maximum displacement which occurs at one point. We could also define δ in terms of displacement averaged over the mode shape. However, we measure a maximum displacement, so we define it at one point. This displacement is the cumulative effect over all frequencies (i.e., in the time domain).

Relating $\frac{1}{2}k_BT$ to the displacement of the mechanical oscillator due to all frequencies,

$$\delta^2 = x_{rms}^2 = S_F \int_0^\infty |G(\omega)|^2 \, d\omega = \frac{k_BT}{k_{eff}}. \tag{B.9}$$

Or, one can view it as relating the thermal noise in the time domain to the thermal noise in the frequency domain:

$$S_F = \frac{k_BT}{k_{eff} \int_0^\infty |G(\omega)|^2 \, d\omega} = \text{constant} \quad \text{(flat noise spectrum)} \tag{B.10}$$

Combining the displacement (Eq. B.9) with the thermal force noise (Eq. B.7), the *force spectral density* of the thermal fluctuations is obtained:

$$S_F^{1/2} = \sqrt{\frac{4k_BT\,k}{Q\,\omega_0}} \qquad \text{in units of } \left[\frac{N}{\sqrt{Hz}}\right]. \tag{B.11}$$

Since $|F(\omega)| = S_F^{1/2}$, and using the functional form of the motion of the mechanical oscillator (Eq. B.5), the *amplitude spectral density* $S_x^{1/2}$ is obtained:

$$S_x = |u(\omega)|^2 = S_F \, |G(\omega)|^2 = 4k_BT \frac{\omega_0}{Qk} \frac{1}{\left(\omega^2 - \omega_0^2\right)^2 + \left(\frac{\omega\,\omega_0}{Q}\right)^2}. \tag{B.12}$$

Some special frequencies of interest are:

$$\begin{array}{lll} \text{On resonance:} & S_X^{1/2} = S_F^{1/2} \frac{Q}{k_{eff}} = \sqrt{\frac{4k_BTQ}{\omega_0\,k_{eff}}} & \text{in } \left[\frac{m}{\sqrt{Hz}}\right] \\ \omega << \omega_0 & S_X^{1/2} = S_F^{1/2} \frac{1}{\omega_0^4} = \sqrt{\frac{4k_BT}{Q\,\omega_0\,k_{eff}}} & \text{in } \left[\frac{m}{\sqrt{Hz}}\right] \\ \omega >> \omega_0 & S_X^{1/2} = S_F^{1/2} \frac{1}{\omega^4} = \frac{1}{\omega^2}\sqrt{\frac{4k_BT\,\omega_0^3}{Q\,k_{eff}}} & \text{in } \left[\frac{m}{\sqrt{Hz}}\right] \end{array} \tag{B.13}$$

B.3 Free vibrations of beams and cantilevers

The physical parameters of mechanical oscillator, such as the force constant and frequency, are determined for cantilevers and doubly clamped beams. These calculations follow the derivations of Prescott [82] and Timoshenko [84], with help from Darrell Harrington [85].

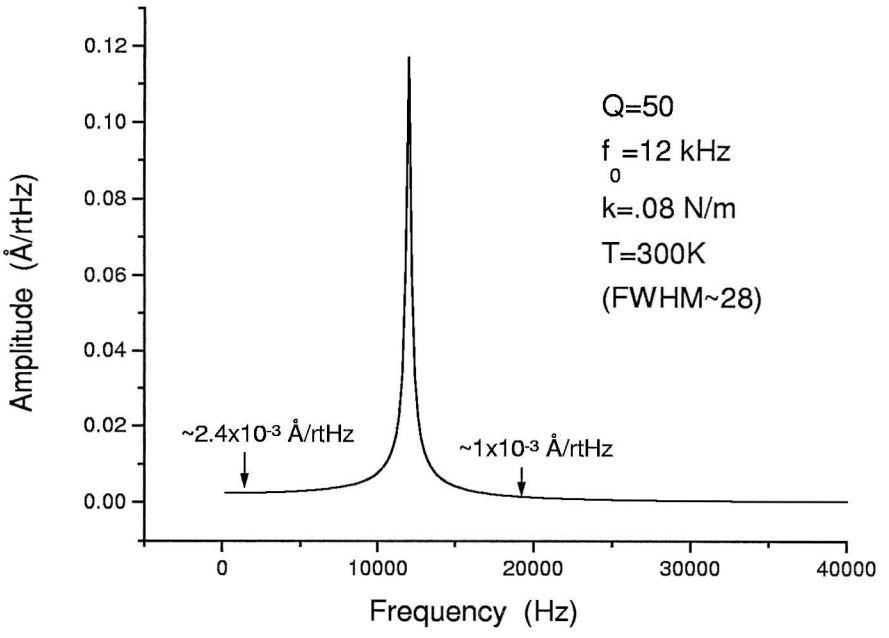

Figure B.2: Thermal noise response of a Si cantilever with $f_0 = 12\,kHz, k = .08\,N/m$ at T=300K. For $Q = 50$ (in air) at $1\,kHz$, $S_F^{1/2} = 2.4x10^{-3}\text{Å}/\sqrt{Hz}$. For $Q = 2000$ (vacuum) at $1\,kHz$, $S_F^{1/2} = 3.7x10^{-4}\text{Å}/\sqrt{Hz}$.

Assuming the beam is much longer than its width or thickness, the equation of motion for the transverse oscillation of a beam is

$$\frac{\partial^2}{\partial x^2}\left(E\ I(x)\frac{\partial^2 u}{\partial t^2}\right) = -\rho A\frac{\partial^2 u}{\partial t^2}, \tag{B.14}$$

where ρ =density, E =Young's Modulus, A =area of the beam cross section, and $I(x)$ =moment of inertia. For a uniform rectangular beam of width w, length L, and thickness t,

$$I = \int_{-1/2}^{1/2} z^2\, w(z)\, dz = \frac{1}{12}A\,t^2 = \frac{1}{12}w\,t^3, \tag{B.15}$$

the transverse equation of motion (Eq. B.14) is simplified to

$$\frac{\partial^4 u}{\partial x^4} = -\frac{\rho\,A}{E\,I}\frac{\partial^2 u}{\partial t^2}. \tag{B.16}$$

B.3.1 Normal modes

There are modes of oscillation where each particle of the beam executes SHM in the same period and phase. The period is independent of x, but the amplitude is a function of x. A normal mode is expressed by:

$$y(x,t) = u(x)\sin(\omega t + \phi) = u(x)\, e^{i(\omega t+\phi)}. \tag{B.17}$$

Putting $y(x,t)$ into the simplified equation of motion (Eq. B.16) yields

$$\frac{d^4u}{dx^4} = m^4 u, \tag{B.18}$$

where

$$m^4 = \frac{\rho A}{EI}\omega^2. \tag{B.19}$$

We assume that $u(x) = Ae^{\alpha x}$, where α is a constant to be determined. Plugging $u(x)$ into Eq. B.18 yields $\alpha^2 = \pm m^2$, so that $\alpha = \pm m, \pm im$. Thus, the general solution is

$$\begin{aligned} u(x) &= A_1 e^{mx} + A_2 e^{-mx} + A_3 e^{imx} + A_4 e^{-imx} \\ &= A\cos mx + B\sin mx + H\cosh mx + K\sinh mx \end{aligned} \tag{B.20}$$

where $H = A_1 + A_2$, $K = A_1 - A_2$, $A = A_3 + A_4$, and $B = i(A_3 - A_4)$. The value of y corresponding to $u(x)$ is given by the above expression. The coefficients will be determined by boundary conditions.

B.3.2 Boundary conditions

(The frequency and effective force constants, ω and k_{eff}, are determined for a point load [82][84].

In general, for a thin oscillating beam with a point load:

$$k_{eff} = \xi' E w \frac{t^3}{L^3}, \qquad f_0 = C' \frac{t}{L^2}\sqrt{\frac{E}{\rho}}, \tag{B.21}$$

and the coefficients are

$$\begin{array}{lll} \text{For a clamped beam} : & \xi' = 16.55 & \text{For a cantilever} : \quad \xi' = 0.2575 \\ & C' = 1.028 & \qquad\qquad\quad C' = 0.1615 \end{array} \tag{B.22}$$

The derivations for the two cases are shown below.

1. **Cantilever (clamped at one end, free at the other end)**

The boundary conditions for a cantilever clamped at one end and free at the other end are:

$$\begin{array}{lll} \text{at } x = 0 : & y = u = 0 & \text{at } x = L : \quad \frac{\partial^2 y}{\partial x^2} = \frac{d^2 u}{dx^2} = 0 \\ & \frac{\partial y}{\partial x} = \frac{du}{dx} = 0 & \qquad\qquad\quad \frac{\partial^3 y}{\partial x^3} = \frac{d^3 u}{dx^3} = 0 \end{array} \tag{B.23}$$

Using the boundary conditions (Eq. B.23) in the general solution (Eq. B.20), a set of equations which determine m and the coefficient relationships are determined. The roots of $\cos ml \cosh ml = -1$ each represent a mode. The lowest modes are:

$$\begin{array}{cccc} m_1 L & m_2 L & m_3 L & m_4 L \\ 1.875 & 4.694 & 7.855 & 10.996 \end{array} \tag{B.24}$$

The shape of the beam for all modes is (taking R=constant):

$$y = R e^{i\omega t} \left[\frac{\cosh mx - \cos mx}{\cosh mL + \cos mL} - \frac{\sinh mx - \sin mx}{\sinh mL + \sin mL} \right] \tag{B.25}$$

For the fundamental mode:

$$y = R\left[.3292\left(\cosh mx - \cos mx\right) - .2417\left(\sinh mx - \sin mx\right)\right] \tag{B.26}$$

Defining δ =maximum amplitude, which is at $x = L$, the fundamental mode equation is renormalized:

$$y = \delta\left[.500\left(\cosh mx - \cos mx\right) - .367\left(\sinh mx - \sin mx\right)\right] \tag{B.27}$$

From Eq. B.18 and $mL = 1.875$,

$$f_0 = C' \frac{t}{L^2} \sqrt{\frac{E}{\rho}}, \quad C' = .1615 \tag{B.28}$$

To determine the effective force constant, k_{eff}, the energy of bending the beam is set equal to $\frac{1}{2}k_{eff}\delta^2$. k_{eff} is essentially an effective force constant, dependent on where along the beam x is determined. For a cantilever, k_{eff} is determined at the free end, where deflection is maximum.

$$\begin{aligned} U_{Bending\,Energy} &= \frac{1}{2}\int_0^L EI\left(\frac{d^2y(x)}{dx^2}\right)dx \\ &= \frac{1}{2}EI\delta^2 m^4 \int_0^L \left[.5\left(\cosh mx+\cos mx\right)-.367\left(\sinh mx+\sin mx\right)\right]^2 dx \\ &= \frac{1}{24}Ewt^3\delta^2\left(\frac{1.875}{L}\right)^4\frac{L}{4} \\ &= (.129)\,EW\frac{t^3}{L^3}\delta^2 \end{aligned} \tag{B.29}$$

Setting $U_{Bending\,Energy} = (.129)\,EW\frac{t^3}{L^3}\delta^2$ equal to $\frac{1}{2}k_{eff}\delta^2$, the fundamental mode of a cantilever has an effective force constant of

$$k_{eff} = (.2575)\,Ew\frac{t^3}{L^3}. \tag{B.30}$$

2 Beam (clamped at both ends)

The boundary conditions of a doubly clamped beam are:

$$\text{at } x=0 \text{ and } x=L: \quad \begin{aligned} y &= u = 0 \\ \tfrac{\partial y}{\partial x} &= \tfrac{du}{dx} = 0 \end{aligned} \tag{B.31}$$

Using the boundary conditions (Eq. B.31) in the general solution (Eq. B.20), a set of equations which determine m and the coefficient relationships are obtained. The roots of $\cos ml\cosh ml = 1$ each represent a mode. The lowest modes are [84]:

m_0L	m_1L	m_2L	m_3L	m_4L
0	4.730	7.853	10.996	14.137

(B.32)

The shape of the beam for all modes is (taking R=constant):

$$y = R e^{i\omega t}\left[\frac{\sinh mL - \sin mL}{\cosh mL + \cos mL}\left(\cos mx - \cosh mx\right) + \left(\sinh mx - \sin mx\right)\right] \tag{B.33}$$

For the fundamental mode:

$$y = R\left[-1.01781\left(\cosh mx - \cos mx\right) + \left(\sinh mx - \sin mx\right)\right] \tag{B.34}$$

Defining δ =maximum amplitude, which occurs at $x = \frac{L}{2}$, the above equation is renormalized to:

$$\begin{aligned} y &= \delta\left[.630\left(\cosh mx - \cos mx\right) - .619\left(\sinh mx - \sin mx\right)\right] \\ y' &= m^2\delta\left[.630\left(\cosh mx + \cos mx\right) - .619\left(\sinh mx + \sin mx\right)\right] \end{aligned} \tag{B.35}$$

From Eq. B.18 and $mL = 4.730$,

$$f_0 = C'\frac{t}{L^2}\sqrt{\frac{E}{\rho}}, \qquad C' = 1.028 \tag{B.36}$$

The energy of bending the beam is:

$$\begin{aligned} U_{Bending\ Energy} &= \frac{1}{2}\int_0^L EI\left(\frac{d^2y(x)}{dx^2}\right)dx \qquad (B.37) \\ &= \frac{1}{2}EI\delta^2m^4\int_0^L\left[.630\left(\cosh mx + \cos mx\right) - .619\left(\sinh mx + \sin mx\right)\right]^2 dx \\ &= \frac{1}{24}Ewt^3\delta^2\left(\frac{4.730}{L}\right)^4\left(.397L\right) \\ &= \left(8.274\right)EW\frac{t^3}{L^3}\delta^2 \end{aligned}$$

Setting $U_{Bending\ Energy} = \left(8.274\right)EW\frac{t^3}{L^3}\delta^2$ equal to $\frac{1}{2}k_{eff}\delta^2$, the fundamental mode of a clamped beam has an effective force constant of

$$k_{eff} = \left(16.55\right)Ew\frac{t^3}{L^3} \tag{B.38}$$

B.4 Determination of k_{eff} by beam deflection under a load

The differential equation of a beam bending due to a transverse force (both uniform and point loads) is [82](p.52)

$$\begin{aligned} EI\frac{\partial^4 u}{\partial u^4} &= f(x) \qquad \text{for a uniform load } \left[\frac{Force}{Length}\right],\ f(x) = f \\ EI\frac{\partial^3 u}{\partial u^3} &= F \qquad \text{for a point force } F \end{aligned} \tag{B.39}$$

For a thin beam, the shear stress due the beam bending is ignore (to first order). The equations of motion (Eq. B.39) are solved by integrating four times and using the boundary conditions to determine the constants. Considering point loads only at the center of the beam (or at the end of the cantilever), the calculations yield

Boundary Conditions	uniform load	point load
Beam (clamped)	$u(x) = \frac{f}{24EI}\left(x^4 - 2Lx^3 + L^2x^2\right)$	$u(x) = \frac{F}{48EI}\left(-4x^3 + 3Lx^2\right)$
Cantilever	$u(x) = \frac{f}{24EI}\left(x^4 - 4Lx^3 + 6L^2x^2\right)$	$u(x) = \frac{F}{6EI}\left(-x^3 + 3Lx^2\right)$

(B.40)

The maximum deflection, δ, can be determined at $x = \frac{L}{2}$ for a clamped beam and at $x = L$ for a cantilever.

$$\begin{aligned} \delta &= \beta\frac{L^4}{EI}f \quad \text{for a uniform load} \\ \delta &= \beta'\frac{L^3}{EI}F \quad \text{for a point load} \end{aligned} \tag{B.41}$$

For small δ and ignoring changes in the beam length due to flexing, the linear restoring force may be approximated. For a uniform beam (with $I = \frac{1}{12}wt^3$),

$$\begin{aligned} f_{restoring} &= \varsigma\frac{Ew}{L}\left(\frac{t}{L}\right)^3\delta \quad \text{uniform load} \\ F_{restoring} &= \varsigma' Ew\left(\frac{t}{L}\right)^3\delta \quad \text{point load} \end{aligned} \tag{B.42}$$

Boundary	uniform load		point load	
Conditions	β	ς	β	ς
beam (clamped)	1/384	32	1/192	16
cantilever	1/8	.67	1/3	.25

(B.43)

For the case of a doubly clamped beam and a point force, the restoring force constant is $k_{eff} = 16Ew\left(\frac{t}{L}\right)^3$. This compares favorably with Eq. B.38.

B.5 Alternate method of obtaining ω and k

An alternate method may be used to determine ω and k [82][84][85]. Simple harmonic oscillators will follow the relationship

$$\omega = \sqrt{\frac{k_{eff}}{m_{eff}}}, \tag{B.44}$$

where k_{eff} and m_{eff} need to be determined for a particular oscillator shape, mode, and location along the beam.

The effective force constant may be determined for a particular point along the beam. Defining δ as the maximum amplitude for a particular mode at point x along the beam as before, k_{eff} is determined by the bending, or potential, energy:

$$U = \frac{1}{2}\int_0^L EI(x)\left(\frac{\partial^2 u(x)}{\partial x^2}\right)^2 dx = \frac{1}{2}k_{eff}\,\delta^2 \tag{B.45}$$

A moving beam has an effective mass because of its motion. This can be determined by using the kinetic energy of the beam:

$$KE = \frac{1}{2}\int_0^L \mu(x)\omega^2\left|u(x)\right|^2 dx = \frac{1}{2}m_{eff}\nu^2 \tag{B.46}$$

where $\mu(x)$ is mass per length (ρA for a uniform cross section beam), and ν is the velocity of a point mass at point x on the beam. (Using the amplitude and frequency, one can determine the acceleration and velocity.) Note that:

a) ν will be different for different points along the beam and for different modes.

b) $m_{eff} < m_{total}$ because the whole beam is not moving as a rigid body.

B.6 Tables: sensitivity vs. cantilever size

These are tables of expected vibration amplitude of a clamped beam for various f_c, Q, and k values determined by the beam dimensions and air pressure.

For a clamped beam (in the thin beam approximation derived above):

$$k_{eff} = \xi' E w \frac{t^3}{L^3}, \qquad f_0 = C' \frac{t}{L^2}\sqrt{\frac{E}{\rho}} \tag{B.47}$$

For a clamped beam : $\xi' = 16.55$, $C' = 1.028$ For a cantilever : $\xi' = 0.2575$, $C' = 0.1615$

where $t = thickness$, $w = width$, and $L = length$ of the beam.

For single crystal Si: $Y_{<100>} = 130 \times 10^9 N/m$, $Y_{<110>} = 169 \times 10^9 N/m$, and $\rho = 2332\, kg/m^3$.

A good approximation to find the amplitude spectral density ($S_x^{1/2}$) and the force spectral density ($S_F^{1/2}$) assumes a first order mode so that each point of the oscillator is a SHO. Thus, the $S_x^{1/2}$ and $S_F^{1/2}$ are only affected through k and f_0. Then the spectral densities are

$$\begin{aligned} S_x^{1/2} &= \sqrt{\tfrac{2k_B TQ}{\pi f_0 k}} \quad \text{in} \quad \left[\tfrac{m}{\sqrt{Hz}}\right] \\ S_F^{1/2} &= \sqrt{\tfrac{2k_B Tk}{\pi f_0 Q}} \quad \text{in} \quad \left[\tfrac{N}{\sqrt{Hz}}\right] \end{aligned} \tag{B.48}$$

For doubly clamped beams at $T = 300K$:

		$k =$	$.1\ N/m$		$k =$	$1\ N/m$
$f\ (MHz)$	Q	$A\ \left(\text{Å}/\sqrt{Hz}\right)$	$S_F^{1/2}\ \left(N/\sqrt{Hz}\right)$		$A\ \left(\text{Å}/\sqrt{Hz}\right)$	$S_F^{1/2}\ \left(N/\sqrt{Hz}\right)$
.5	10	.007	$.70 \times 10^{-15}$		.002	23×10^{-15}
	10^3	.07	$.07 \times 10^{-15}$		.02	2.3×10^{-15}
	10^5	.7	$.007 \times 10^{-15}$		.2	$.2 \times 10^{-15}$
5	10	.002	$.23 \times 10^{-15}$		.0007	7.3×10^{-15}
	10^3	.02	$.02 \times 10^{-15}$		.007	0.73×10^{-15}
	10^5	.2	$.002 \times 10^{-15}$		.07	0.07×10^{-15}

For doubly clamped beams at $T = 10K$:

		$k =$	$.1\ N/m$		$k =$	$1\ N/m$
$f\ (MHz)$	Q	$A\ \left(\text{Å}/\sqrt{Hz}\right)$	$S_F^{1/2}\ \left(N/\sqrt{Hz}\right)$		$A\ \left(\text{Å}/\sqrt{Hz}\right)$	$S_F^{1/2}\ \left(N/\sqrt{Hz}\right)$
.5	10	.0013	$.13 \times 10^{-15}$		.0004	4.2×10^{-15}
	10^3	.013	$.013 \times 10^{-15}$		.004	0.42×10^{-15}
	10^5	.13	$.0013 \times 10^{-15}$		.04	0.042×10^{-15}
5	10	.0004	$.04 \times 10^{-15}$		.00013	1.3×10^{-15}
	10^3	.004	$.004 \times 10^{-15}$		.0013	0.13×10^{-15}
	10^5	.04	$.0004 \times 10^{-15}$		.013	0.01×10^{-15}

C Processing details

C.1 NiFe-tipped cantilevers

IN GENERAL

A layer of photoresist is coated onto Si commercial AFM cantilevers. Surface tension prevents the photoresist from coating the region of the tip. Without breaking vacuum, the tip surface is cleaned with a short ECR etch and permalloy is sputtered onto the cantilever. The lift-off in acetone removes the excess permalloy, leaving only the tip region coated. The cantilevers are Silicon-MDT SC12 series Ultrasharp tips. The photoresist is Microposit 1813 (positive).

SPECIFICS

Spin A centered chuck is used to spin-coat photoresist onto the cantilever. The substrate of the mechanical resonator is placed at the center of the chuck, which results in the tip of a mechanical resonator being approximately $1.75mm$ off the axis of rotation of the chuck. This placement causes photoresist to spread in one direction along the cantilever arm towards the tip. Slow acceleration (5.0) and rotation speeds (5000 rpm) are used to force the photoresist onto the thin cantilever surface, without spinning all the resist off the cantilever. Slower speeds/accelerations result in the resist being left on the substrate and not spread onto the cantilever arm. Faster speeds/accelerations result in the resist being spun off the cantilever all together, or leaving most of the cantilever arm uncoated. It is then baked on a hot plate for 5 minutes at 100°C.

ECR Etch/Sputter The tip surface is cleaned with a 10 second ECR Argon etch (100V, 300W, Ar 15sccm). Without breaking vacuum, permalloy from a $Ni_{89}Fe_{19}$ target is

then RF sputtered onto the cantilever. The sputter conditions have been optimized for stress free films (Ar 20sccm, 5x10-3mTorr, 1.1Å/sec, power=200W). If the ECR cleaning step is skipped, the permalloy layer has been found to come off the cantilever tip upon slight contact. ECR cleaned tips tend to have stronger adhesion to the permalloy longer. This is vital to scanning applications.

Liftoff The excess permalloy is removed through an acetone lift-off. Ultrasound cleaning (5–60 seconds) is sometimes required to remove the permalloy from the cantilever arm.

A commercial Si cantilever in its original uncoated state and with its tip coated with a layer of magnetic material (NiFe) is shown in Figure 3.13.

C.2 YIG mask (thick photoresist)

The protective mask used to make the YIG rectangle series used the following photoresist and recipes.

Photoresist Shipley SJR 5740 microposit

Developer Microposit 2401 (ratio: $30mL$ developer, $120ml$ H_2O)

Spin 60 seconds, acceleration 10. For thickness, see table below.

spinning rate (rpm)	thickness (μm)
1000	15
2000	10
3000	8
4000	7

Bake 1 hour at 80-90°C in an oven (not a hot plate). Longer bake times result in steeper sides.

Best results: Spin at 3000rpm, bake 1 hour. Repeat (two layers). Expose UV for 2.0 minutes. Develop for 2.0 minutes. In the SEM, the photoresist had a thickness of $13 - 15\mu m$.

D

Calculations of H_d

These numerical calculations were performed by Dr. Wei Chen using Mathcad. The magnetic sample has lateral dimensions a and b, and thickness c. For YIG, the bulk value $4\pi M_s = 1750\,Gauss$ was used.

To calculate the internal field in the z direction, assume the magnetization is $\vec{M}$, and the sample is polarized along the z direction (normal to the film plane). The scalar magnetic potential [79] along the normal centerline $(0, 0, z)$ is

$$\Phi_M(z) = \int_{=a/2}^{a/2}\int_{-b/2}^{b/2}\left(\frac{M}{(x^2+y^2+z^2)^{1/2}} + \frac{(-M)}{(x^2+y^2+(c-z)^2)^{1/2}}\right)dx\,dy. \tag{D.1}$$

Thus, the internal field component in the z direction, $H_{z,int}$, is given by:

$$H_{d,z} = -\frac{\partial\,\Phi_M(z)}{\partial\,z} = \int_{=a/2}^{a/2}\int_{-b/2}^{b/2}\left(\frac{M\cdot z}{(x^2+y^2+z^2)^{3/2}} + \frac{M\cdot(c-z)}{(x^2+y^2+(c-z)^2)^{3/2}}\right)dx\,dy. \tag{D.2}$$

To obtain $H_{z,int}$ at the center of the film, we set $z = c/2$, and use Mathcad to integrate given the dimensions of the samples.

Similarly, we obtain $H_{x,int}$ and $H_{y,int}$ by assuming the sample is polarized in the x or y direction:

$$H_{d,x} = -\frac{\partial\,\Phi_M(z)}{\partial\,x} = \int_{=b/2}^{b/2}\int_{-c/2}^{c/2}\left(\frac{M\cdot x}{(y^2+z^2+x^2)^{3/2}} + \frac{M\cdot(a-x)}{(y^2+z^2+(a-x)^2)^{3/2}}\right)dy\,dz \tag{D.3}$$

$$H_{d,y} = -\frac{\partial\,\Phi_M(z)}{\partial\,y} = \int_{=c/2}^{c/2}\int_{-a/2}^{a/2}\left(\frac{M\cdot y}{(z^2+x^2+y^2)^{3/2}} + \frac{M\cdot(b-y)}{(z^2+x^2+(b-y)^2)^{3/2}}\right)dz\,dx$$

where we put in the values $x = a/2$ and $y = b/2$ respectively, according to the sample dimensions.

To calculate the resonance field H for microstructures:

$$\begin{aligned}\left(\frac{\omega}{\gamma}\right)^2 &= [H - 4\pi\,(N_z - N_x)\,M]\times[H - 4\pi\,(N_z - N_y)\,M] \\ &= [H - (H_{d,z} - H_{d,x})]\times[H - (H_{d,z} - H_{d,y})]\end{aligned} \tag{D.4}$$

$$\Rightarrow H = H_{d,z} - \frac{1}{2}\left(H_{d,x} + H_{d,y}\right) + \frac{1}{2}\left[\left(H_{d,x} - H_{d,y}\right)^2 + 4\left(\frac{\omega}{\gamma}\right)^2\right]^{1/2}. \tag{D.5}$$

E

Magnetic films on high frequency cantilevers

The resolution of MRFM can be increased by utilizing magnetic thin films as the probe magnet. Magnetic films, which produce large gradient fields near the edge, require the external field to be parallel to the film plane to saturate the magnet and to maximize the gradient field. Also, these thin films are typically deposited onto the flat surface of a mechanical oscillator. These two requirements can be satisfied with the perpendicular geometry.

The sensitivity of the MRFM can be improved by reducing the thermal noise of the mechanical oscillator. This can be achieved by increasing the frequency of the mechanical oscillator. High frequency beams increase the data rate, reduce the thermal noise, and allow for the possibility of direct coupling to the resonance.

The combination of these two improvements led to the development of thin magnetic films on high frequency Si beams, as shown in Figure E.1. These will be used in future MRFM experiments. The feasibility of producing thin magnetic films on high frequency Si beams for use in MRFM was determined in the early part of these studies. Further development of utilizing magnetic films on high frequency beams are being continued in our group.

These preliminary studies demonstrated the feasibility of using magnetic films on high frequency beams as the mechanical force detector in MRFM. First, we verified the ability to detect the higher frequency beams with the fiber optical detection method used in MRFM. The beams are much smaller than the commercial cantilevers, which reduce the reflectively and increased the difficulty of aligning the fiber and mechanical resonator. The higher frequency yields a smaller thermal peak than the commercial cantilevers. Thus, the noise

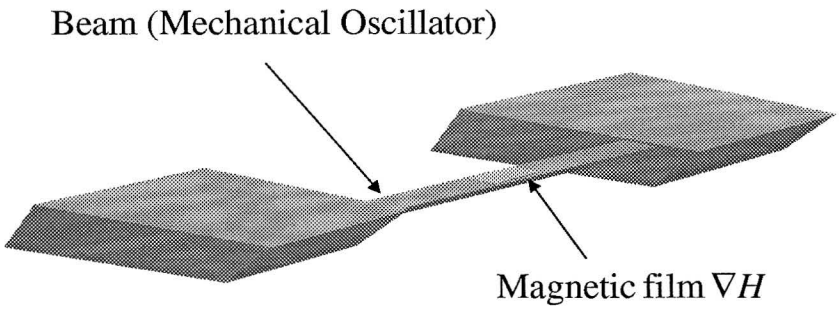

Figure E.1: An integrated mechanical detector for MRFM. The magnetic thin film is located at the center of the high frequency beam.

floor of the fiber optic system compared to the thermal noise of the mechanical oscillator is important. Second, we developed new processing techniques to create mechanical oscillators with magnetic films. Optical lithography and chemical wet-etching techniques were used.

E.0.1 Doubly clamped beams

The force constant and resonant frequency of a mechanical oscillator, derived in Appendix B, are

$$k = \xi' E w \frac{t^3}{L^3}, \qquad f_0 = C' \frac{t}{L^2}\sqrt{\frac{E}{\rho}}, \tag{E.1}$$

where $\xi' = 16.55$ and $C' = 1.028$ for a doubly-clamped beam. The thermal force noise, F_{rms}, which must be reduced is

$$F_{rms} = \sqrt{\frac{4k}{Q\omega_c} k_B T \, \Delta f}. \tag{E.2}$$

From these equations it is clear that optimizing both ω_c (large) and k (small) for small thermal noise cannot be done by simply increasing the length or reducing the thickness of the oscillator. Furthermore, there are limitations on the dimensions of the beam due to processing techniques. A range of values have been calculated and are shown in the table below. These are calculated for a Si doubly clamped beam with $t = .2\mu m$, $w = 3\mu m$, $Q \sim 10^3$, $\Delta f = 1Hz$, and $T = 293K$.

ω_c	f_c	L	L/t	k	F_{rms}
$1.0MHz$	$150kHz$	$75\mu m$	375	$.08N/m$	1.1×10^{-15}
$2.1MHz$	$333kHz$	$50\mu m$	250	$.26N/m$	1.4×10^{-15}
$5.8MHz$	$.9MHz$	$30\mu m$	150	$1.22N/m$	1.8×10^{-15}

As the table indicates, increasing the frequency results in shorter beams with higher force constants. The longer beams, with smaller force constants, have lower frequencies, and are also much harder to produce. Beams with $L = 30\mu m$ were produced using optical lithography methods with a success rate of $\sim 30\%$. Only one $L = 50\mu m$ beam was successfully produced and no $L = 75\mu m$ beams were produced.

The resonance characteristics of a Si beam with $L = 30\mu m$, coated with 60Å Cr and 220Å Au along its length, was measured with two methods: electromotive force (EMF) and fiber optic detection. The EMF measurement also serves as a verification for the thermal noise spectrum obtained from the fiber optic detection method.

First, the resonance frequency of the high frequency beam was measured using the electromotive force technique at a temperature of 4.2K in vacuum [80]. The beam was mounted in a chip carrier with the long axis of the beam perpendicular to the magnetic field. The magnetic field was supplied by a superconducting solenoid. Electrical connections to the Cr/Au layer on the beam were made by Au wire bonds to the chip carrier. A network analyzer was used to drive an alternating current along the length of the beam and also to measure the response of the beam. The alternating current, perpendicular to the magnetic field, generates a Lorenz force which drives the beam perpendicular to both its length and magnetic field direction. The motion of the beam, because of the Cr/Au layer, generates an electromotive force (EMF) along the length of the beam. The amplitude of the current created by the EMF is directly related to the oscillation amplitude of the beam. This EMF, corresponding to the cantilever response to the Lorenz driving force, is detected by the network analyzer. Thus, by driving the beam, the resonance frequency of the beam and its nominal Q is determined. The EMF response for the Si beam with $L = 30\mu m$ in a field of 4.6T is shown in Figure E.2. The measured resonance frequency was 2.3MHz and the Q was $\sim 10^4$.

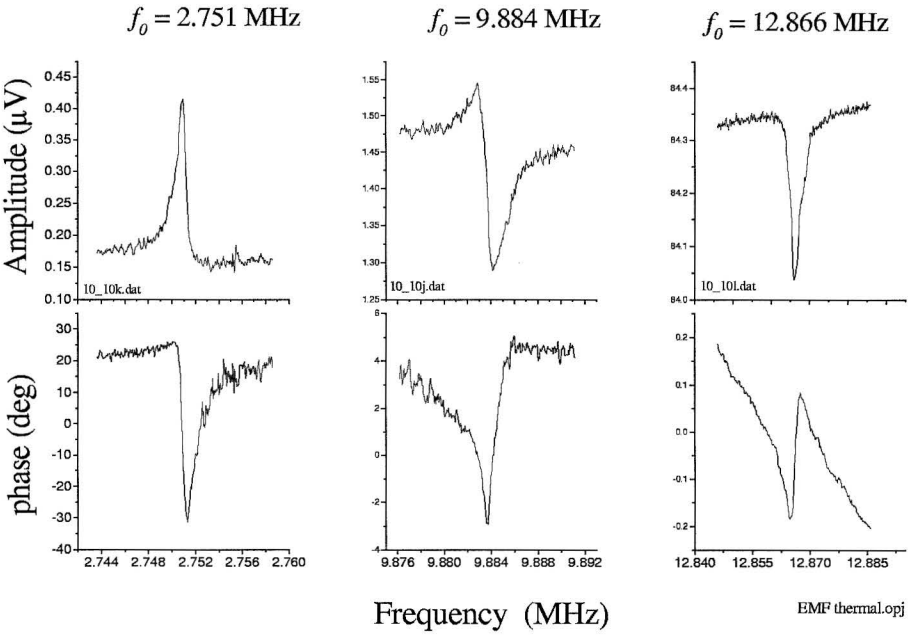

Figure E.2: The resonance response of a Si beam with $L = 30\mu m$ in a field of 4.6T. The first, third, and forth harmonics are shown.

Second, the high frequency beam was measured using fiber optic detection. This signal is not driven, as it was for the EMF method, and is the true thermal noise spectrum. The spectrum of the beam for a single shot measurement is shown in Figure E.3. The theoretical curve is determined by the physical properties of the beam, and has no fitting parameters (see Appendix B). The measured resonance frequency of 2.3MHz and the Q of $\sim 10^4$ corresponds with the previous results determined by EMF detection methods. The noise floor of the fiber optic system is $0.02\text{Å}/\sqrt{Hz}$.

The DC signal from the photodiode was used to position the fiber over the beam. The fiber core is $4\mu m$, and the fiber and beam must be aligned within $1\mu m$. The Cr/Au coating on the cantilever reflects the laser light with a greater intensity than the rough surface of the patterned Si. Thus, as the fiber is scanned over the substrate, the DC photodiode signal increases when the fiber is located above the beam. The center of the beam is determined

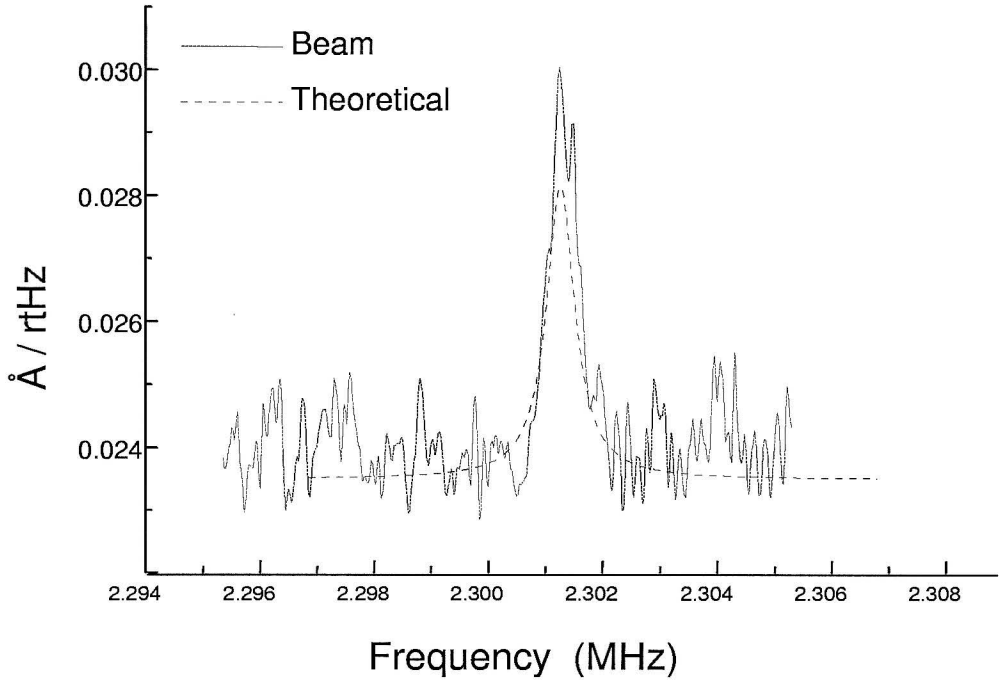

Figure E.3: Thermal peak of the $L = 30\mu m$ beam, which has a resonance frequency of 2.3MHz and a Q of 10^4. The theoretical fit is based upon physical properties of the beam and has no fitting parameters.

by mapping out the intensity of the reflected laser light versus position over the Si substrate.

These measurements verified the feasibility of detecting and utilizing high frequency beams as the mechanical detectors in MRFM.

E.0.2 Magnetic films

To increase the resolution, large magnetic gradient fields are required. A thin NiFe magnetic film can produce large gradients near its edge, on the order of $10^3 - 10^5$ (see section "Perpendicular Force Geometry"). However, typical photolithography methods to produce Si beams use Ni as a protective layer that is later removed. This would destroy the NiFe film intended to serve as the gradient magnet. A new processing method was developed to create an integrated mechanical force detector.